The Dissertation Committee for Armando Ruggiero Sena D'Anna Certifies that this is the approved version of the following dissertation:

Modeling and Imaging of Ground Penetrating Radar data

Committee:

Paul L. Stoffa, Co-Supervisor

Mrinal K. Sen, Co-Supervisor

Robert Tatham

Steve P. Grand

Jacob T. Fokkema

Clark R. Wilson

Modeling and Imaging of Ground Penetrating Radar data

by

Armando Ruggiero Sena D'Anna, Lic.

DISSERTATION

Presented to the Faculty of the Graduate School of
The University of Texas at Austin
in Partial Fulfillment
of the Requirements
for the Degree of

DOCTOR OF PHILOSOPHY

The University of Texas at Austin
December 2004

Dedication

To my parents Salvatore and Maria

Acknowledgements

I would like to extend my deepest gratitude to my supervisors Dr. Paul Stoffa and Dr. Mrinal Sen for their excellent guidance, encouragement and support through out my graduate studies. I would also like to acknowledge Dr. Steve Grand, Dr. Jacob Fokkema, Dr. Robert Thatam and Dr. Clark Wilson for their invaluable advice and encouragement as committee members.

I would also like to thank Dr. Jay Banner for being part of my examining committee and helping me with planning the GPR surveys at the cave site near Georgetown, Dr. Mironov Anatoliy for helping me to set up the GPR equipment, Dr. Roustam Seifoullaev for his help with data acquisition, and Dr. Donald Blankenship for facilitating the airborne radar data used in this dissertation.

I deeply thank Dr. William Fisher and William Galloway for their invaluable friendship, excellent classes in statigraphy and sedimentology, and their help and encouragement during my graduate studies.

Special thanks are due to Dr. Gail Christeson, Dr. Kirk McIntosh and Dr. Paul Mann for inviting me to participate in the Hess Deep cruise in the summer of 2003, allowing me to obtain first hand knowledge about marine seismic data acquisition. I also thank Dr. Yosio Nakamura, Ben Herber and Stephen Saustrup for the technical discussion during the cruise and their kind friendship.

I would also like to thank visiting scientist Dr. Indrajit G. Roy for his friendship and encouragement, and all my present and former colleagues at the Institute for Geophysics and the Department of Geological Sciences of The

University of Texas at Austin: Veronica Castillo, Anubrati Mukherjee, Alejandro Escalona, Dhananjay Kumar, Sylvia Nordfjord, Irina Filina, Xinxia Wu, Juan Bermudez, Nedra Bonal, Lisa Watson, Diego van Berkel, Robert Rogers, Chengshu Wang, Timothy Meckel, Leonel Gomez, Erick Lyons, David Gomey, Ricardo Combellas, Imtiaz Ahmed, Samarjit Chakraborty, Rishi Bansal, Chandan Kumar, Hongbo Lu and Erick Leuro. I also thank my friends Silvia Perez, Jean Carlos Perez, Paulina Malavis, Alfonso Benavides, Delia Perez and Jesus Salazar for their support and company during my studies here in Austin.

I would like to thank Kevin Johnson for his computer support, and especially Mark Wiederspahn for his invaluable discussions on program optimization and computer systems. I also thank Susan Beaubien, Judy Sansom, Kathy Ellins, Don Yarbro, Charlene Palmer, Lisa Gahagan, Patricia Ganey-Curry, Nancy Hard, Eleanor Picard, Philip Guerrero, Dennis Trombatore, Mary Koch, Alice Rentz, Miriam Pashby and all the administrative and technical staff of the Institute for Geophysics, the Department of Geological Sciences and the Geology Foundation.

I would like to acknowledge various sources of financial support during my graduate studies: “Consejo de Desarrollo Científico y Humanístico” of the Central University of Venezuela, the Ewing Worzel and Gale White fellowships of the Institute for Geophysics and the Thomas R. Banks memorial scholarship.

Finally, I would like to give very special thanks to my mother, my sisters Yolanda and Lucia, and my brothers Arcangelo and Filippo. Without their love and support this work would not have been possible.

Modeling and Imaging of Ground Penetrating Radar data

Publication No.____________

Armando Ruggiero Sena D'Anna, Ph.D.
The University of Texas at Austin, 2004

Supervisors: Paul L. Stoffa and Mrinal K. Sen

Ground Penetrating Radar (GPR) is an active and non-invasive exploration technique based on the propagation of electromagnetic waves in the subsurface. Modeling of GPR data is important because it helps us with data interpretation and forms the basis (solution to the forward problem) for most iterative inversion techniques. Conversely, migration (or imaging) is a type of inversion technique (backward propagation) that creates an image related to the subsurface reflectivity and can be used to estimate the model parameters of the media that affect the propagation of the waves. However, for practical applications, modeling and migration techniques must be fast, accurate and efficient.

I have developed a fast, efficient and accurate GPR modeling technique for stratified media (isotropic and laterally homogeneous layers) based on the invariant imbedding or reflectivity technique. To test the results obtained with this technique, and have a general tool for modeling of GPR data in heterogeneous, dispersive and isotropic media, I have implemented a 3D explicit Finite Difference Time Domain (FDTD) technique. The FDTD formalism is presented in conjunction with a discussion of the electromagnetic dispersion mechanisms that affect the GPR signal in most geologic media. I show that the results obtained with the reflectivity and FDTD techniques are nearly identical for laterally homogeneous media. Real GPR data is used to study the capabilities and practical aspects that affect the accuracy of the reflectivity technique.

I have developed a new technique for migration of GPR data in heterogeneous and lossy media. I have implemented the technique in 2D media and presented the formalism for its extension to 3D media. The new technique, based on the Split Step Fourier migration technique, allows us to efficiently include the dispersion and attenuation effects in the media. An approximation of homogeneous plane waves, which do not add new restrictions to the Split Step Fourier technique, gives greater stability to the imaging technique allowing us to migrate the data through thicknesses up to three times the characteristic skin depths of the media computed at the dominant frequency of the GPR signal.

Table of Contents

List of Tables

List of Figures

Chapter I: Introduction

The importance of Ground Penetrating Radar (GPR) has increased in the last decades extending its application to different areas of research, engineering and subsurface exploration. This increasing use of the GPR technique can be attributed to several factors: improvement in the instrumentation coupled with a reduction of the equipment cost, improved surveying efficiency and costs, and better portability of the equipment. However, processing of GPR data has not evolved accordingly and has relied on existing processing techniques developed for seismic data. In this chapter, I give a brief description of the GPR technique, explain the similarities with and differences from the seismic techniques and present the motivations for this dissertation.

1.1 GROUND PENETRATING RADAR TECHNIQUE

1.1.1 Origin and general description

Ground Penetrating Radar (GPR) is a subsurface imaging technique based on the detection of transmitted and reflected electromagnetic waves that propagate through the subsurface. The technique can be applied in any media where the skin depth (depth of penetration) for the dominant frequency of the radar signal is, at least, comparable to the depths of the targets we are interested in detecting and imaging.

The origin of the GPR technique goes back to the second quarter of the last century, when the RADAR technology was developed (Stern, 1930). Due to the lack of very short time instrumentation (intervals in the order of nanoseconds), the application of this technique was restricted to resolve the thickness of ocean ice sheets and glaciers. Since then, the improvement of technology for signal generation, acquisition and processing have broadened the application spectrum of this technique. The technique has been referenced with different names in the literature (e.g., Ground Probing Radar, Ground Penetrating Radar, Georadar) and has been widely used in the last two decades. Regardless of the shallow penetration of the technique in common soil (due to its conductivity, which produces a strong attenuation of the electromagnetic waves), the technique has been successful in areas such as civil engineering (e.g., Fruhwirth and Mueller, 1994), hydrology (e.g., Gloaguen, et. al., 2001), mining and placer exploration (e.g., Davis, et. al., 1984), fracture mapping (e.g., Grandjean and Gourry, 1996; Tsoflias, 2004), shallow stratigraphy (Dominic, et. al., 1995) and archeology (e.g., Sternberg and McGill, 1995).

In the GPR technique, an antenna (generally, an electric dipole whose length is about one half of the dominant wavelength of the radar signal) generates electromagnetic waves that propagate through the media. Then, the same antenna (mono-static mode) or another antenna (bi-static mode) receives the transmitted or reflected waves that propagate through, or reflect from, the media. In the multi-antenna configuration, more than one receiver (or transmitted) antenna can be used. However, these types of acquisition systems are not commonly used in the GPR technique because of cross talk problems among the antennas and the increased cost of the equipment.

The current at the transmitter antenna can be a short pulse (pulse radar) or a chirp signal (continuous wave radar). These two modes are the analog to explosions and Vibroseis used in seismic techniques. Pulse radars are the most commonly used because they do not require preprocessing and contain a broader frequency spectrum. Pulse radars have a dominant frequency of oscillation (peak of the spectrum), and the duration of the pulse determines the width of the spectrum. Commonly, the voltage (or current) applied to the transmitter antenna is designed in such a way that the half-width of the spectrum of the generated signal is approximately equal to half the dominant frequency (e.g., Davis and Annan, 1989). Figure 1.1 shows experimental data for a typical pulsed GPR signal (Bernabini, et. al., 1995).

At the receiver antenna, the incident electromagnetic waves generate a voltage (on the order of microvolts) that is recorded as a function of time for each position of the receiver and the transmitter. Then, the data is converted to digital format and stored. Commonly, for a given position of the receiver and transmitter antennas, the source is fired several times and the signal, acquired at the receiver, is stacked to increase the S/N ratio, and then, it is stored.

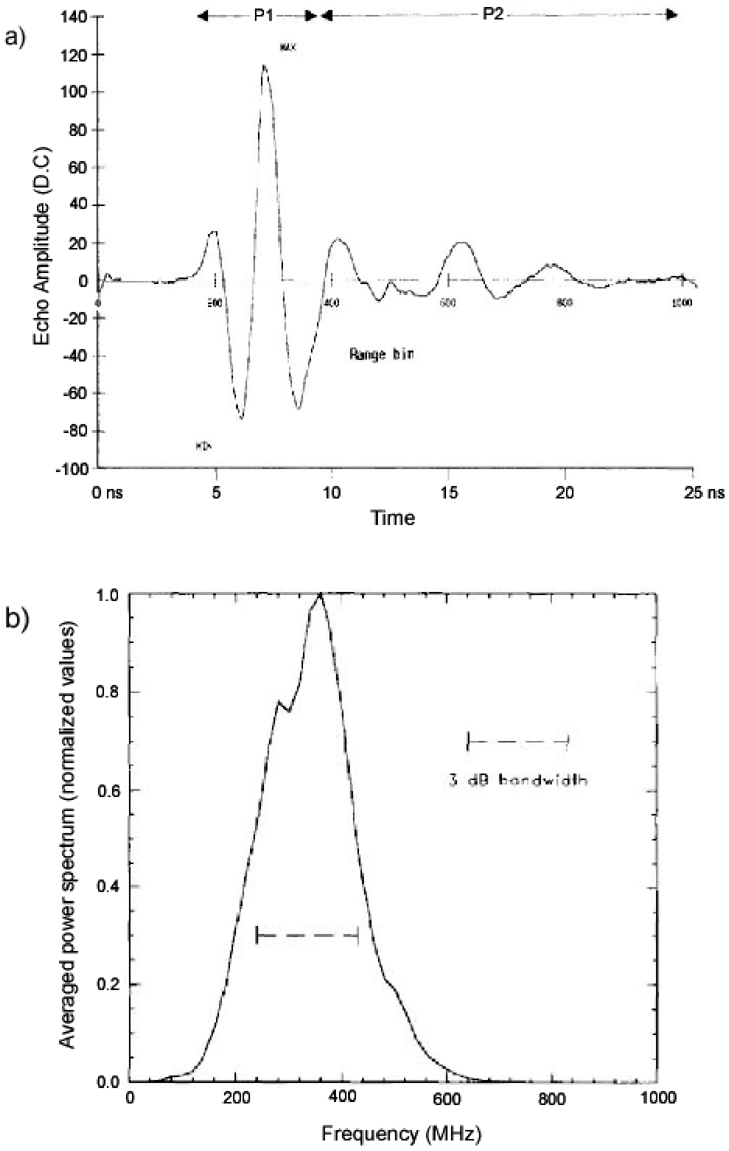

Figure 1.1. (a) Example of a GPR trace and (b) corresponding power spectrum. The power spectrum was estimated using the data within the window "P1" (Bernabini, et. al., 1995).

1.1.2 Acquisition modes and surveys

The GPR technique can be classified in two general categories: transmission or reflection techniques.

In the transmission techniques, the forward scattered wave field (transmitted waves) is recorded by placing the transmitter and receiver antenna on opposite sides of the system under study. These techniques are mostly based on the measurement of the traveltime and amplitude of the first arrival signals, corresponding to the so-called Traveltime Tomography (i.e., inversion of the transmitter-receiver traveltimes) and Amplitude Tomography (i.e., inversion of the amplitude variations due to absorption in the media), respectively. These techniques are based on the same principles as their seismic counterparts, and most applications have been found in areas such as Civil Engineering (e.g., Carlsten, et. al., 1995) or in cross hole tomography in Hydrology and mineral exploration (e.g., Zhou and Fullagar, 2001).

In the reflection techniques, the backward scattered wave field (reflected waves) is recorded by placing the transmitter and receiver antennas on the same side of the system or target under study. In this case, migration of the complete record allows us to obtain an image of the reflector (surfaces of contrasting impedances) present in the system. Inversion techniques based on the Born approximation have also been implemented for electric permittivity and conductivity anomalies with some degree of success (e.g., Hansen and Johansen, 2000).

Because electromagnetic waves are transverse, they have polarization properties. The state of polarization and intensity of the radiated waves depend on the orientation and form of the transmitter antenna. On the other hand, the receiver antenna also has a directivity that affects its own sensitivity; therefore, depending on the relative orientation of the transmitter and receiver antennas different responses are possible from the same medium. The classification of the different acquisition modes, according to the relative orientation of the transmitter and receiver antennas, and the survey line is shown in Figure 1.2. The orientation of the antennas is very important because the radar sections of the anomalies (reflectors) not only depend on their geometry, but also on their orientation relative to the direction of polarization of the incident wave. An interesting application of this characteristic of the GPR technique, has been presented by Van Gestel et. al. (2001). They have proposed a technique to recognize the orientation of scattering anomalies and also improve the resulting image by using Alford rotation in the migration algorithm.

In the acquisition modes shown in Figure 1.2 only one receiver antenna is used. However, it is possible to use two or three receiver antennas at the same receiver position oriented perpendicularly to each other, so that we can record the three components of the electric field at the receiver position. These are called multi-component GPR data (e.g., Lehmann, et. al., 2000, and Kruk, et. al., 2003). However, this type of survey is not very common and, when they are implemented, it is usual to record only the horizontal components of the electric field (i.e., parallel to the surface). This configuration of the receiver antennas is related to the polarization and radiation pattern generated by the transmitter antenna, which is generally placed parallel and very close to the surface in order to maximize the energy transmitted into the ground (e.g., Carcione, 1998; and Lampe, et. al., 2003).

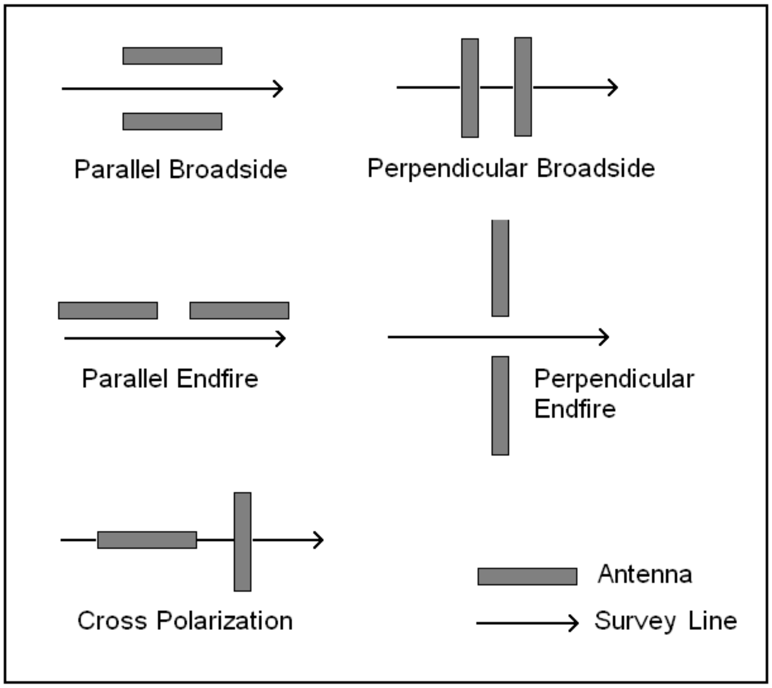

Figure 1.2 Acquisition modes in accordance to the relative deployment of the antennas and the survey line.

Systems with multiple transmitter and/or receiver antennas placed at different positions are also possible. However, the necessary instrumentation for the short pulses and sampling intervals used in the GPR technique (nanoseconds and fractions of nanoseconds, respectively) makes these multi-antenna configurations very expensive and they have not been in common use. If these practical difficulties are overcome, we will be able to acquire multi-component and multi-channel GPR data, which are necessary for a correct 3D imaging of GPR data in heterogeneous media (this point is discussed in more detail in chapter 4).

Commonly, GPR acquisition equipments include a transmitter and a receiver antenna, which allows the acquisition modes presented in Figure 1.1. With only two antennas, the GPR surveys are normally carried out along lines. Several lines can be gathered to form a pseudo-3D survey (common offset or multi offset data). They are not complete 3D surveys because out of plane reflected waves are not properly recorded and the character of the wavelet can change during the survey.

There are two different types of field procedures for acquisition along survey lines:

- **Common offset**: the receiver and transmitter antennas are moved along the line, and the distance (offset) between them is kept constant;

- **Wide Angle Reflection and Refraction (WARR)**: in this case, the transmitter and receiver antenna are moved along a line in such a way that the distance between them is changed (normally, increased). Three field procedures are usually employed: the transmitter (or receiver) antenna is fixed at a given position and the receiver (or transmitter) antenna is moved away (along the line), or the receiver and transmitter antennas are moved along the line in such a way that the middle point is always at a fixed position. This last procedure is also called **Common Mid-Point** (CMP) profiling.

The trace gathers obtained directly from these field procedures are called, common offset and WARR (common transmitter, common receiver, and common mid-point) gathers, respectively. If full coverage is acquired (with one of these field procedures), the traces can be resorted from one type of gather to the others. As we can see, the gather nomenclature is essentially the same as that used in seismic techniques (e.g., Yilmaz, 2001). Figure 1.3 shows a cartoon explaining these types of acquisition procedures.

Common offset gathers are usually acquired to obtain a fast profile (image) of the subsurface, whereas CMP gathers are acquired at selected locations to make an analysis of the wave velocity in the media. If full coverage is recorded (e.g., CMP gathers are collected at close and uniformly spaced mid-points along the line), then a full pre-stack processing sequence can be applied to the data (including pre-stack residual velocity analysis). Pipan, et. al. (2003) show an example where seismic processing software was used to carry out a complete pre-stack processing of GPR data (including migration velocity analysis).

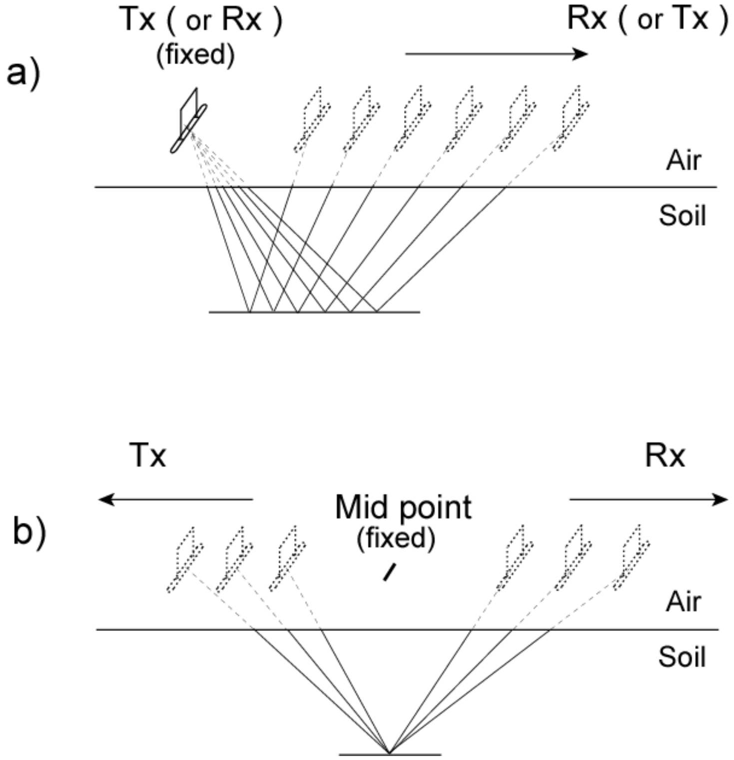

Figure 1.3. Different WARR acquisition procedures. (a) Transmitter (or receiver) acquisition, and (b) CMP acquisition.

1.2 ELECTROMAGNETIC PROPERTIES OF GEOLOGIC MEDIA

The properties of the media that affect the propagation of electromagnetic waves are the electric permittivity, electric conductivity and magnetic permeability. Depending on the frequency of the electromagnetic signal, each of these properties can have a greater or smaller effect on the propagation of the signal. These electromagnetic properties are, in general, independent of the mechanical (elastic) properties of the media. However, the electric permittivity and conductivity are strongly affected by fluid content in the media, and therefore, by the porosity, fractures and type of fluids in the media. Because these factors also affect the mechanical properties of the media, a correlation between electromagnetic and mechanical parameters can be observed in some particular cases, especially when the porosity and fluid saturation are moderate to high.

Most geologic media are non-magnetic (i.e., their relative magnetic permeability are practically equal to 1; e.g., Telford, et. al., 1976), and so, the electric permittivity and conductivity have, in most cases, greater importance for the GPR technique. Water content affects strongly the electric permittivity of rocks. This can be understood by the larger permittivity of water relative to the host material of most rocks. Water content also affects the electric conductivity of rocks since available ions can enter in solution, increasing the conductivity of the fluid, and therefore, of the whole rock. Table 1.1 shows some typical values of electric permittivity and conductivity for some typical rocks. Notice the influence of water content on the electric permittivity and conductivity. When clays are present in the media, the increase of conductivity with the addition of water in the system is significant. In practice, this is the main factor that affects the penetration of the GPR signal in the subsurface.

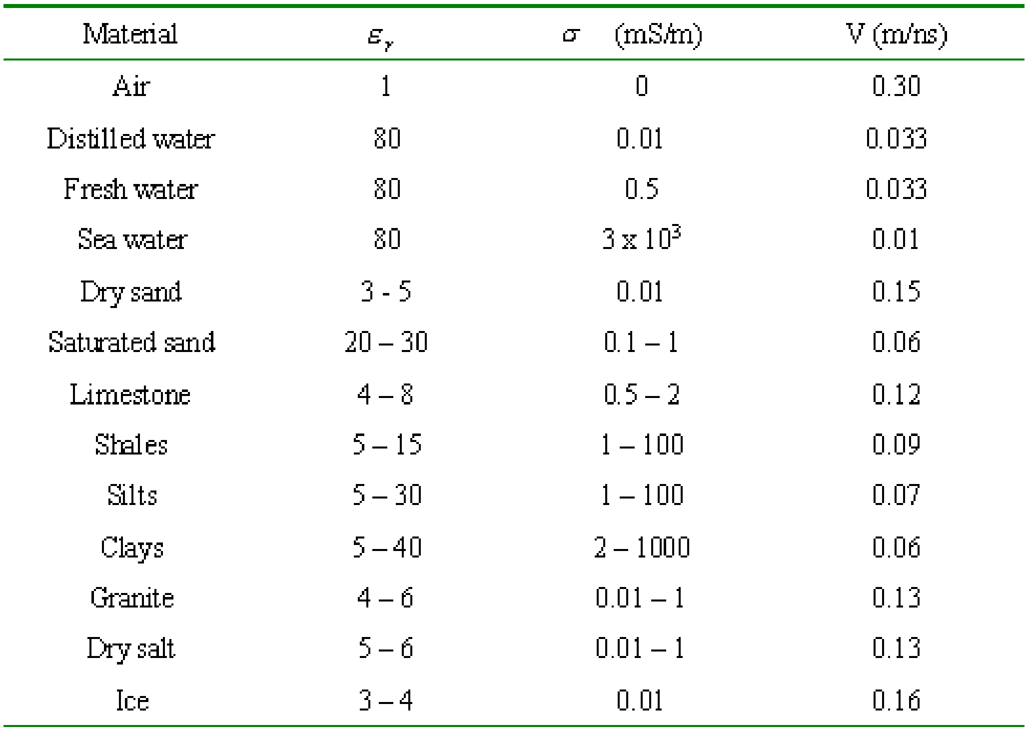

Material	ε_r	σ (mS/m)	V (m/ns)
Air	1	0	0.30
Distilled water	80	0.01	0.033
Fresh water	80	0.5	0.033
Sea water	80	3×10^3	0.01
Dry sand	3 - 5	0.01	0.15
Saturated sand	20 – 30	0.1 – 1	0.06
Limestone	4 – 8	0.5 – 2	0.12
Shales	5 – 15	1 – 100	0.09
Silts	5 – 30	1 – 100	0.07
Clays	5 – 40	2 – 1000	0.06
Granite	4 – 6	0.01 – 1	0.13
Dry salt	5 – 6	0.01 – 1	0.13
Ice	3 – 4	0.01	0.16

Table 1.1. Electromagnetic parameters of some geologic media (after Davis and Annan, 1989)

1.3 DISPERSION AND ATTENUATION OF ELECTROMAGNETIC WAVES IN GEOLOGIC MEDIA

Dispersion and attenuation of electromagnetic waves are inherently related. The Kramers-Kronig relations (e.g., Jackson, 1975) ensure that absorption and dispersion take place simultaneously to preserve causality, and so, there is a dependency between the complex and real part of the slowness in the frequency domain for any absorptive medium. Dielectric and magnetic absorptions, as well as conductivity losses, produce attenuation and dispersion of electromagnetic waves. These effects are important and must be simultaneously taken into account for correct modeling and imaging of GPR data.

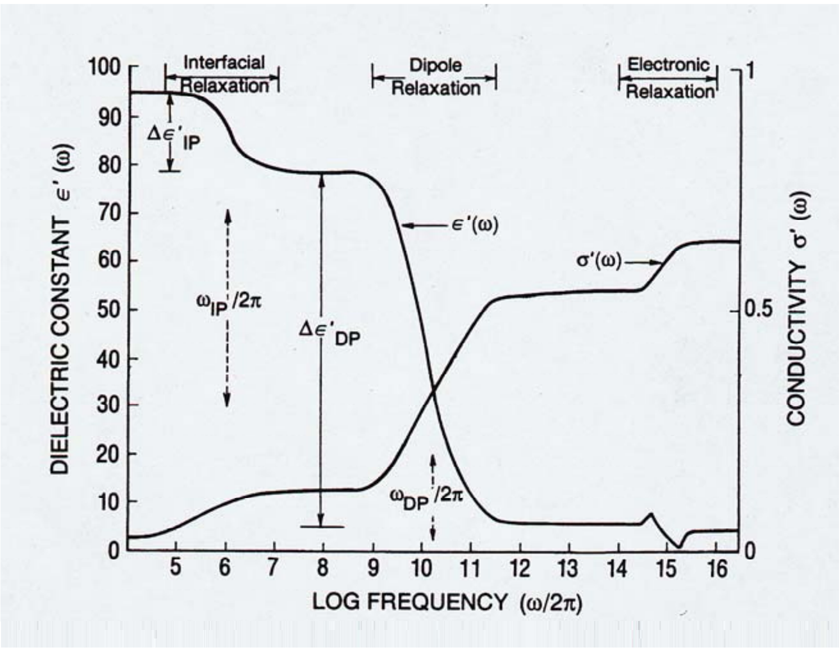

Figure 1.4. General behavior of a two component material. Interfacial and dipole relaxation are the main mechanisms for dielectric dispersion in most rocks. σ' is the effective conductivity in S/m of the composed material (Sherman, 1988).

Sherman (1988) presented a model for the frequency dependence of the dielectric permittivity observed in sandstone and limestone in the frequency band between 96 and 1300 MHz, and also a general review of the dielectric dispersion mechanisms in rocks. Figure 1.4 shows the main mechanisms for dielectric dispersion in rocks. The variable σ' in Figure 1.4 is the effective conductivity of the material and represents the imaginary part of the dielectric permittivity plus the contribution of the DC conductivity (related to Joule's effect). As we will see, interfacial and dipole relaxations are the main mechanisms of dielectric dispersion in the frequency band of the GPR technique.

Interfacial mechanisms are related to the so-called Double-layer effect. It is responsible for the increase of dielectric permittivity observed at intermediate and low frequencies in moist rocks (e.g., Scott, et. al., 1967), and at tens of megahertz in moist soils that contain pollutant substances (Blacic and Arulanandan, 1999) or clays (e.g., Olhoeft and Capron, 1994).

The dipole mechanism is related to molecular relaxation. The molecular relaxation of water is the most significant for the GPR technique. The peak of this relaxation mechanism for pure water is around 8 GHz (e.g., Eisenberg and Kauzmann, 1969) but, in moist soils, the peak is shifted downward to a frequency of 1.5 GHz approximately (Hoekstra and Delaney, 1974). This absorption is so strong that it represents an upper limit for the frequencies that are useful for the GPR technique in most geologic media.

Most geologic media are non-magnetic and do not present magnetic dispersion. Olhoeft and Capron (1994) have reported some degree of magnetic dispersion on a dry iron-silica powder mixture. The relative difference between the Debye's low and high frequency permeabilities was not higher than 20%, even for a 40% composition of iron, making this type of dispersion less important than dielectric dispersion, which can reach relative differences between the Debye's low and high frequency permittivities larger than 300 % (Olhoeft and Capron, 1994).

1.4 PREVIOUS WORK ON MODELING AND IMAGING OF GPR DATA

1.4.1 Modeling

During the last few years many papers on modeling of GPR data have been published. Most have been on finite difference time domain (FDTD) techniques (e.g., Roberts and Daniels, 1997; Xu and McMechan, 1997; and Teixeira, et. al., 1998). Luebbers (1992) presented a FDTD technique for modeling of electromagnetic waves in Nth-order dispersive media, and Carcione (1996) and Carcione and Schoenberg (2000) applied a similar formalism for modeling GPR data in anisotropic and dispersive media. The FDTD technique has also been used for modeling the radiation pattern of antennas with different geometries including the effect of the air-soil interface (e.g., Carcione 1998, and Lampe, et. al., 2003).

The FDTD modeling technique has the advantages of relatively simple implementation and allows us to obtain a better interpretation of the physical phenomenon. However, the required computational resources and computational time are, in many cases, prohibitive. This has lead to the investigation of more efficient modeling techniques. Zeng, et. al (1995) presented a comparison of ray and Fourier methods for modeling mono-static GPR data. Baumgartner, et. al. (2001) presented a geometric (ray) modeling technique to compute the electromagnetic scattering of cylinders, and Xiong and Tripp (1997) used a 3D integral equation modeling technique to compute the electromagnetic response of near surface scatterers (targets). Even though these techniques are computationally more efficient than FDTD techniques, they are based on approximations (e.g., the high frequency approximation for ray theory) and do not include all orders of interaction (multiples), even for the case of 1D media.

Modeling in 1D media is important because many geologic systems are horizontally stratified and these models are very good approximation for these stratified systems. The modeling techniques aforementioned are computationally too expensive to be used in formal inversions for these systems. In the electromagnetic literature, modeling of electromagnetic data in horizontally homogeneous media have been traditionally carried out by computation of reflection coefficients in the wave-number and frequency domain using a continues fraction scheme, as originally presented by Wait (1953). Pervago, et. al. (2003), have extended this technique for electric field modeling in arbitrary anisotropic layered media. However, this technique is not efficient for forward modeling (in inversion techniques) because a change in only one of the layers requires that the whole computation, from the bottom to the top layer, be carried out in order to obtain the new reflection coefficients.

An alternative to the continuous fraction technique is the so-called invariant imbedding or reflectivity technique originally developed by Thomson (1950) and Haskell (1953) for seismic data modeling. Kennett (1974) improved this technique by introducing recursion equations that allow us to combine the response of the layered subsystems and obtain the total response of the whole system. These recursion equations not only allow us to obtain, more efficiently, the new response of the whole system if only one (or a few) layers of the model are changed, but also makes the reflectivity technique unconditionally stable since in the computation of the reflection and transmission matrices of the subsystems, the presence of growing exponential terms can be avoided. Ursin (1983) made a theoretical review of this technique for elastic and electromagnetic waves; however, he did not develop, in detail, the specific case for electromagnetic waves. After Ursin’s work, there has not been more work published on this technique for modeling electromagnetic waves in layered media, particularly for modeling of GPR data. The development and implementation of this technique, for modeling GPR data in layered isotropic media, is one of the main objectives of this dissertation.

1.4.2 Imaging

Due to the similarities between GPR and the seismic techniques, most GPR data processing has been carried out using seismic data processing software (e.g., Davis and Annan, 1989; and Grasmueck and Horstmeyer, 1994) and little effort has been directed toward developing specific algorithms for processing of GPR data, and take into account the particular characteristics of this technique. The most interesting advances have been in imaging algorithms that take into account the polarization characteristics of the GPR techniques and also the air-soil interface effects. For example, Van der Kruk, et. al. (2003) presented a three-dimensional and multi-component imaging algorithm for GPR data in homogeneous subsurface media; Van Gestel and Stoffa (2001) used Alford rotation in multi-component GPR data to improve the imaging of elongate scattering objects immersed in an homogeneous subsurface medium, the rotation for optimal coherence superposition of the multi-component data gives information about the orientation of the scattering objects; Tsoflias et. al. (2004) have shown a multi-component GPR interpretation technique to detect vertical fractures (and their orientations) in horizontally stratified media; and Meincke (2001) has presented a linear inversion algorithm for GPR data. However, these algorithms have been developed supposing that the subsurface is homogeneous (they are based on the Green’s function for a system of two semi-infinite homogeneous media) and therefore, do not take into account the lateral variations of the electromagnetic properties in the subsurface.

There have also been some seismic or general inversion and mapping techniques that have been adapted for inversion or imaging of GPR data. For example, Wang and Oristaglio (2000) presented an inversion technique that used the generalized Radon transform. No simultaneous inversion for electric permittivity and conductivity of the medium is possible and it supposes that the background medium is homogeneous. Most of the imaging techniques for GPR data suppose that the subsurface is homogeneous, which in many cases does not represent correctly the subsurface and introduces considerable errors in the final image. Recently, Di and Wang (2004) implemented a finite-element reverse-time migration technique for GPR data that takes into account the lateral variations and conductivity of the media; the computational resources required by this technique are smaller than finite difference methods, but the results presented by Di and Wang are not encouraging because of loss of resolution and deterioration of the S/N ratio. These effects are probably generated by numerical dispersion and are increased when the conductivity of the media is included in their migration algorithm.

1.5 MOTIVATION AND OBJECTIVES

The first objective of this work is to develop and implement the reflectivity or invariant imbedding technique for modeling of GPR data in isotropic and laterally homogeneous media. This technique will allow us to do a quantitative interpretation of multi-offset GPR data in stratified media and could be used to generate the GPR response (forward problem) in future inversion techniques for GPR data. The importance of the reflectivity technique can be appreciated, for example, from the work presented by Sen and Stoffa (1991) and Stoffa and Sen (1991) on stochastic inversion of seismic data, or Sen and Roy (2002), which uses a gradient descent inversion algorithm. In these cases, the reflectivity technique is chosen to compute the seismic response of a given model, which changes at each iteration of the inversion technique (in Sen and Roy's paper, even the Frechet derivatives are computed based on the reflectivity technique). Therefore, the reflectivity technique is very efficient for these computationally intensive algorithms.

The second objective of this dissertation is to develop an imaging technique for GPR data that takes into account the heterogeneities, absorption and dispersion effects of the media. The technique that I have developed is based on the Split step Fourier migration technique (Stoffa et. al., 1990), which is a wave field extrapolation technique that takes into account (in a first order approximation) the lateral variation of the media. Because this technique is completely implemented in the frequency domain, it allows us to correctly compensate for dispersion and attenuation in an efficient way. The importance of this new migration technique is that it will increase the resolution, coherence and effective depth of penetration of the GPR technique, and so, increase the usefulness and areas of application for the method. In addition, when we correctly take into account the dispersion and attenuation effect produced by dielectric and magnetic absorption, and electric conductivity of the media, we are creating the basis for future inversion techniques based on the imaging algorithm (e.g., Valera et. al., 1998) that will allow us to estimate the electromagnetic parameters of the media, and therefore, improve the interpretation of the GPR data.

The proposed modeling and imaging techniques share something in common: they are based on a full Fourier transform (in space and time) and the extrapolation of the wave field in a homogeneous medium is carried out by a simple phase shift operator. However, each technique has a property that the other lacks. On one side, the reflectivity technique includes the dynamic response of the system, but the technique is strictly valid only for laterally homogeneous media. On the other side, the Split step Fourier technique can manage lateral variation of the media but it does not include the dynamic response of the system (i.e., it does not include changes of the wave field due to reflection and transmission coefficients at contrasting impedance interfaces). The development of these two techniques sets the basis for a hybrid technique to model GPR data that will be more efficient than other modeling techniques and will be able to take into account lateral variations of the media.

The third objective of this dissertation is to implement an explicit FDTD modeling technique for GPR data in 3D heterogeneous, dispersive and anisotropic media. This modeling technique can help us to interpret real GPR data in complex areas, and allows us to test the aforementioned reflectivity and imaging techniques.

Because the FDTD technique will be used to generate synthetic data for testing the new modeling and imaging techniques, I first present the FDTD technique in chapter 2. In chapter 3, I develop the theory of the reflectivity modeling technique and compare the results with synthetic data, generated with the FDTD technique, and show an application of this technique for the interpretation of real GPR data. In chapter 4, I develop the new GPR imaging technique and explain what I call the “plane wave approximation”, which gives more stability to the migration technique. Then, I give some examples, with synthetic and real data, that show the benefits of the new migration technique. Finally, in chapter 5, I present my conclusions and suggestions for future work.

Chapter 2: Finite Difference Time Domain technique

In this chapter, I present the details of implementation of an explicit staggered FDTD technique to model GPR data in heterogeneous, anisotropic and dispersive media. Numerical results are presented to show its capabilities and validity. This technique will allow us to improve our interpretation of real GPR data, compare the results obtained with other modeling techniques and test new migration techniques for GPR data in complex geologic media.

2.1 INTRODUCTION

Finite Difference Time Domain (FDTD) techniques belong to the group of numerical methods used to solve differential equations based on a discrete approximation of the derivative operators. Finite difference techniques to model GPR data are important because they allow us to solve the wave equation in heterogeneous, dispersive and anisotropic media without making any extra approximation other than the discrete approximation of the differential operators. In this way, we obtain a solution to the wave equation that includes all the phenomena observed in real GPR data, i.e., diffractions, reflections and refractions.

The advantage of the time domain techniques is that we directly obtain the response of the system at each time step, and therefore, we gain physical insight for the phenomenon under study. FDTD techniques can be implemented using two different schemes: implicit or explicit. In the implicit schemes, the new values of the functions, at each time step, are obtained by solving a system of simultaneous equations, whereas in the explicit schemes the new values of the functions are directly obtained by using explicit equations (i.e., formulas), making the amount of computation required, in each time step, smaller than in implicit schemes. However, to avoid numerical instability, explicit schemes require smaller grid sizes and time intervals than implicit schemes, and therefore, the total amount of computation required to solve a given problem is comparable in both the schemes (e.g., Isaacson and Keller, 1966). The main advantage of explicit techniques is their simple implementation, which in fact allows us to include, without extra difficulty, characteristics of the media such as dispersion and anisotropy. For this reason, I have chosen the explicit technique in the implementation presented in this chapter. However, implicit schemes may have some advantages over the explicit schemes, specifically for modeling very low frequencies (including zero frequency) and improving the stability of the FDTD technique.

Yee (1966) was the first to propose a staggered grid scheme for modeling electromagnetic waves using finite differences. The staggered grid allows us to directly express the spatial derivatives of the magnetic and electric fields using second order finite difference operators and, by computing the fields in alternate instants, second order finite difference operators can also be used to express the temporal derivatives of the fields. In this way, Maxwell’s equations can directly be used to model the propagation of electromagnetic waves using second order finite difference operators in space and time.

Roberts and Daniels (1997) used Yee's technique to model 3D GPR data in conductive media. They incorporated important parameters such as the shape of the antennas, feeding cables and height of the antennas above the ground. They also compared real measurements with model data, obtaining very good agreement. Correctly modeling the radiation pattern of a finite antenna is a 3D problem. However, as pointed out by Roberts and Daniels, solving such a problem using finite differences is computationally very expensive. Xu and McMechan (1997) proposed a 2.5 D technique for modeling of GPR data in 2D media that incorporates the characteristics of the radiation pattern of the antenna. Their approach consists of applying a Fourier transform in the invariant direction of the media, solving the resulting equation using Yee's technique in 2D media for a subset of wave numbers, and finally applying an inverse Fourier transform to obtain the 3D modeled data. In addition to the radiation pattern of the antenna, they also included dielectric absorption in their FDTD technique via memory variables (Debye's mechanisms). Carcione (1996) developed a modeling technique for GPR data that included anisotropy and intrinsic dispersion of the electric permittivity and conductivity. He implemented the algorithm for TM mode in 2D media and used a hypothetical infinite magnetic current as the source. Wang and Oristaglio (2000) implemented a perfect matching layer (PML) absorbing boundary condition for modeling 3D GPR data in dielectric dispersive media using the PML technique developed by Berenger (1994).

Lampe et. al. (2003), presented a detailed study of the radiation pattern of different antennas used in the GPR technique. They used an explicit FDTD technique and a PML absorbing boundary condition, but no anisotropy or dispersion was considered. They showed how the radiation pattern changes for different antennas and different conditions of the soil as well as the effect of shielded or unshielded antennas. They concluded that the asymptotic far-field equations commonly used to model the radiation pattern of GPR antennas (Engheta, 1982, and Smith 1984) may be a poor representation at intermediate-field zones.

The explicit FDTD technique has been the more commonly used technique to accurately model GPR data. In this chapter, I present the implementation and some test results for this technique. Then, in the next chapters, this technique will be used to verify the results obtained with the reflectivity technique (Chapter 3) and generate the synthetic data used for testing the new technique for migration of GPR data in heterogeneous, conductive and dispersive media (Chapter 4). I have implemented the FDTD technique for modeling GPR data in 3D media. However, because of the high computational cost of the 3D algorithm, I also implemented the technique for 2D media. In this case, the source is modeled as an infinite electric current and I also incorporate electric dispersion in the media. This allows me to efficiently generate the response of many different 1D and 2D models in order to test the reflectivity and new migration techniques.

2.2 MAXWELL'S EQUATIONS AND CONSTITUTIVE RELATIONS

2.2.1 Maxwell's equations

Maxwell's equations in a general media are (in SI units),

$$\nabla x \underline{E} = -\frac{\partial \underline{B}}{\partial t} \ , \tag{2.1}$$

$$\nabla x \underline{H} = \frac{\partial \underline{D}}{\partial t} + \underline{J} \ , \tag{2.2}$$

$$\nabla \cdot \underline{D} = \rho \ , \tag{2.3}$$

$$\nabla \cdot \underline{B} = 0 \ , \tag{2.4}$$

where $\underline{E}$ is the electric field, $\underline{H}$ is the magnetic field, $\underline{D}$ is the electric displacement, $\underline{B}$ is the magnetic flux density, $\underline{J}$ is the current density and ρ is the electric charge density.

It is important to mention that equation (2.3) is a consequence of equation (2.2) and the *conservation law* of electric charge, i.e.,

$$\nabla \cdot \underline{J} + \frac{\partial \rho}{\partial t} = 0 \ , \tag{2.5}$$

whereas equation (2.4) establishes the experimental (and fundamental) observation that magnetic monopoles do not exist. Notice that equation (2.4) can be obtained from equation (2.1) when the magnetic and electric fields vary with time, but it cannot if the fields are static (i.e., if the fields do not vary with time).

2.2.2 Constitutive relations and geologic media

Equations 2.1 to 2.4 are not complete; they require two more vectorial equations that relate the magnetic and electric fields. Such equations are called constitutive relations and describe how the response of the media affects the electromagnetic fields. In the literature, it is common to represent the fields $\underline{D}$ and $\underline{B}$ as a function of $\underline{E}$ and $\underline{H}$, i.e.,

$$\underline{D} = \underline{D}(\underline{E}, \underline{H}) \ , \tag{2.6}$$

$$\underline{B} = \underline{B}(\underline{E}, \underline{H}) \ . \tag{2.7}$$

Another important quantity in Maxwell's equations is the current density $\underline{J}$, which has two contributions, i.e.,

$$\underline{J} = \underline{J}_s + \underline{J}_{ind} \ , \tag{2.8}$$

where $\underline{J}_s$ is due to external sources and $\underline{J}_{ind}$ is the induced current density consisting in the movement of free (or mobile) charges in the media. Since the magnetic field does not do any effective work on electric charges, the induced current can, in general, be represented as a function of the electric field, i.e.,

$$\underline{J}_{ind} = \underline{J}_{ind}(\underline{E}) \ . \tag{2.9}$$

The specific form of the functions in equations (2.6), (2.7) and (2.9) characterize the electric and magnetic properties of the media. For example, the vacuum is completely linear, isotropic and non magneto-electric (i.e., the magnetic field does not generate electric displacement, and the electric field does not generate magnetic flux). Therefore, the constitutive equations are,

$$\underline{D} = \varepsilon_0 \underline{E} \ , \tag{2.10}$$

$$\underline{B} = \mu_0 \underline{H} \ , \tag{2.11}$$

$$\underline{J}_{ind} = 0 \ , \tag{2.12}$$

where $\varepsilon_0 = 8.854x10^{-12}$ F/m and $\mu_0 = 4\pi x10^{-7}$ H/m are the electric permittivity and magnetic permeability of the vacuum.

For small intensities of the electromagnetic fields (which is the case in the GPR technique), most materials behave linearly, i.e., the vectors $\underline{D}$, $\underline{B}$ and $\underline{J}_{ind}$ will be linearly dependent on $\underline{E}$ and $\underline{H}$. General constitutive relations for anisotropic, dispersive and linear media can be written as (e.g., Karlsson and Kristensson, 1992),

$$\underline{D} = \varepsilon_0 \left[\underline{\underline{\varepsilon}}_{\infty} \underline{E} + \int_{-\infty}^{t} \underline{\underline{\Phi}}_e (t - t') \underline{E}(t') dt' \right] + \underline{\underline{\gamma}}_m \underline{H} + \int_{-\infty}^{t} \underline{\underline{\Upsilon}}_m (t - t') \underline{H}(t') dt' , \quad (2.13)$$

$$\underline{B} = \mu_0 \left[\underline{\underline{\mu}}_{\infty} \underline{H} + \int_{-\infty}^{t} \underline{\underline{\Psi}}_m (t - t') \underline{H}(t') dt' \right] + \underline{\underline{\kappa}}_e \underline{E} + \int_{-\infty}^{t} \underline{\underline{\mathrm{K}}}_e (t - t') \underline{E}(t') dt' , \quad (2.14)$$

and,

$$\underline{J}_i = \underline{\underline{\sigma}}_{\infty} \underline{E} + \int_{-\infty}^{t} \underline{\underline{\Theta}}_e (t - t') \underline{E}(t') dt' . \quad (2.15)$$

However, most geologic media are not chiral or magneto-electric, i.e., the magneto-electric tensors $\underline{\underline{\gamma}}_m$ and $\underline{\underline{\kappa}}_e$ (time independent) and $\underline{\underline{\Upsilon}}_m$ and $\underline{\underline{\mathrm{K}}}_e$ (time dependent) are very small and can be neglected. Additionally, since the relative magnetic permeability in most geologic media is very small (a few units), the magnetic losses can usually be neglected (i.e., $\underline{\underline{\Psi}}_m \approx 0$). This is due to the fact that the area of the hysteresis curve, which defines the magnetic losses, is very small if the magnetic permeability is very small. Another important aspect of geologic media is that their conductivity does not change appreciably with frequency (e.g., Scott,et. al., 1967). This is due to the small inertia of the free charges (ions and electrons), allowing them to respond to oscillating electric fields even at the high frequencies of the GPR technique. The lag between the induced current density and the electric field, produced by the inertia of the free charges, begins to be important at frequencies above hundreds of GHz, reducing the effective conductivity of the media and modifying also its phase velocity (e.g., Jackson, 1975). This means that the time-dependent tensors $\underline{\underline{\Theta}}_e$ can be neglected for most geologic media at least for frequencies up to (and including) the frequency band of the GPR technique. In this way, equations 2.13 to 2.15 can be reduced to,

$$\underline{D} = \varepsilon_0 \underline{\underline{\varepsilon}}_\infty \underline{E} + \varepsilon_0 \int_{-\infty}^{t} \underline{\underline{\Phi}}_e (t - t') \underline{E}(t') dt' \ , \tag{2.17}$$

$$\underline{B} = \mu_0 \underline{\underline{\mu}}_r \underline{H} \ , \tag{2.18}$$

$$\underline{J}_{ind} = \underline{\underline{\sigma}} \underline{E} \ , \tag{2.19}$$

where I have renamed the instantaneous response permeability tensor $\underline{\underline{\mu}}_\infty$ as the relative tensor $\underline{\underline{\mu}}_r$ and the instantaneous response conductivity tensor $\underline{\underline{\sigma}}_\infty$ simply as the conductivity $\underline{\underline{\sigma}}$ (even though the symbol "∞"denotes "infinite frequency" response, physically it represents the instantaneous response of the media observed in the frequency band of interest).

2.2.3 Debye's mechanisms of dispersion

Dispersion is introduced in equations 2.13 to 2.15 through the time dependent tensors $\underline{\underline{\Phi}}_e$, $\underline{\underline{\Upsilon}}_m$, $\underline{\underline{\Psi}}_m$, $\underline{\underline{K}}_e$ and $\underline{\underline{\Theta}}_e$. Physically, we expect that the response of the media will depend more strongly on the present and recent values of the magnetic and electric fields and less on their past values. This means, mathematically, that these tensors should be decaying functions of time. In general, any decaying function of time can be expressed as a superposition of decaying time exponentials. This are called Debye's functions and each one represents a Debye's relaxation mechanism. Even though Debye developed his original work on dielectric dispersion (Debye, 1925), analogous results have been obtained for magnetic and elastic dispersion (Cole and Cole, 1945). Debye's functions, in addition to being physically plausible, are mathematically advantageous since by introducing new auxiliary vectors (called "memory" variables), associated with each Debye's mechanism, the convolution involved in equations 2.13 to 2.15 are circumvented, improving the numerical efficiency when modeling (in the time domain) dispersion effects in the media.

Theoretically, a continuous superposition (distribution) of Debye's mechanisms can generate any observed dispersion (e.g., Cole and Cole, 1945). However, for numerical purposes, we must select a finite number of Debye's mechanisms to represent the dispersion effects in the media. Such a finite representation is always possible in a limited frequency band, which can be selected according to the spectrum of the signal. Since we are interested in modeling dispersion effects in geologic media, let's focus on equation 2.17. Then, the tensor $\underline{\underline{\Phi}}_e$ can be represented as,

$$\underline{\underline{\Phi}}_e(t) = \sum_{l=1}^{L} \underline{\underline{\Phi}}_l(t) \quad , \tag{2.20}$$

with

$$\underline{\underline{\Phi}}_l(t) = \omega_l \underline{\underline{a}}_l e^{-\omega_l t} \quad , \tag{2.21}$$

where $\omega_l = 1/\tau_l$ is the relaxation frequency, and $\underline{\underline{a}}_l = \underline{\underline{\varepsilon}}_s^l - \underline{\underline{\varepsilon}}_\infty$ is a relative permittivity weighting tensor associated with each Debye's mechanism with relaxation time τ_l, and low frequency electric permittivity tensor $\underline{\underline{\varepsilon}}_s^l$. These expressions are generalizations of the representations presented by Xu and McMechan (1997). Now, for each Debye's mechanism, we define a memory variable $\underline{\xi}_l$ given by,

$$\underline{\xi}_l(t) = \int_{-\infty}^{t} \underline{\underline{\Phi}}_l(t-t')\underline{E}(t')dt' \ , \tag{2.22}$$

and therefore,

$$\underline{D} = \varepsilon_0 \left[\underline{\underline{\varepsilon}}_\infty \underline{E} + \sum_{l=1}^{L} \underline{\xi}_l \right] , \tag{2.23}$$

Differentiating equation 2.22 with respect to t, and using the definition of $\underline{\underline{\Phi}}_l$, we obtain,

$$\frac{\partial \underline{\xi}_l}{\partial t} = -\omega_l \underline{\xi}_l + \omega_l \underline{\underline{a}}_l \underline{E} \ , \qquad \text{for } l = 1,2,....,L \tag{2.24}$$

Now, differentiating equation 2.23 with respect to t and substituting equation 2.24,

$$\frac{\partial \underline{D}}{\partial t} = \varepsilon_0 \left[\underline{\underline{\varepsilon}}_\infty \frac{\partial \underline{E}}{\partial t} + \left(\sum_{l=1}^{L} \omega_l \underline{\underline{a}}_l \right) \underline{E} - \sum_{l=1}^{L} \omega_l \underline{\xi}_l \right] , \tag{2.25}$$

Substituting this equation and equations 2.8, 2.18 and 2.19 in the equations 2.1 and 2.2, we obtain,

$$\nabla x\underline{E} = -\underline{\underline{\mu}}\frac{\partial \underline{H}}{\partial t} \ , \tag{2.26}$$

$$\nabla x\underline{H} = \underline{\underline{\varepsilon}}\frac{\partial \underline{E}}{\partial t} + \left(\varepsilon_0 \sum_{l=1}^{L} \omega_l \underline{\underline{a}}_l + \underline{\underline{\sigma}} \right) \underline{E} - \varepsilon_0 \sum_{l=1}^{L} \omega_l \underline{\xi}_l + \underline{J}_s \ , \tag{2.27}$$

where $\underline{\underline{\mu}} = \mu_0 \underline{\underline{\mu}}_r$ and $\underline{\underline{\varepsilon}} = \varepsilon_0 \underline{\underline{\varepsilon}}_\infty$ are the instantaneous (high frequency) magnetic permeability and electric permittivity tensors. These two equations together with equation 2.24 form the basis for FDTD modeling of GPR data in anisotropic and dielectrically dispersive media.

2.3 DISCRETIZATION OF MAXWELL'S EQUATIONS

2.3.1 Staggered grid and the spatial and temporal finite difference operators

Yee (1966) first proposed the staggered grid to model electromagnetic waves. The technique takes advantage that Maxwell's equations already describe the electromagnetic waves as a system of first order differential equations. By staggering the spatial positions and instants for the electric and magnetic fields, mid-point second order difference operators can be used to write, in discrete form, the spatial and temporal first order derivatives of the fields. Figure 2.1 shows the spatial unit cell used in Yee's staggered grid technique. The electric field is defined at instants $t = n\Delta t$, whereas the magnetic field is defined at instants $t = \left(n + 1/2\right)\Delta t$.

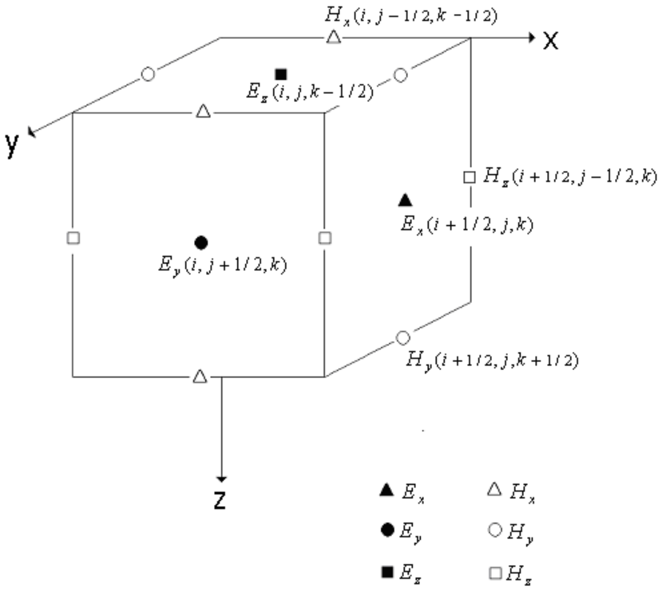

Figure 2.1. Spatial unit cell used in Yee's staggered grid technique (modified from Roberts and Daniels, 1997).

The parameters of the media are defined at some particular position of the unit cell. However, an interpolation of the parameters will be, in general, necessary to find their values at the positions where they are required (i.e., where the components of the fields or their derivatives are defined). In the case of dispersive media, the components of the memory variables $\underline{\xi}_l$ will be placed at the same position of the components of the electric field, but they will be defined at the instants $t = (n + 1/2)\Delta t$.

Using super indices to denote the discrete time instant, the first order derivatives of the fields and memory variables can be written as,

$$\left.\frac{\partial \underline{E}}{\partial t}\right|^{n+1/2} = \frac{\underline{E}^{n+1} - \underline{E}^{n}}{\Delta t} \ ,$$
$$\left.\frac{\partial \underline{H}}{\partial t}\right|^{n} = \frac{\underline{H}^{n+1/2} - \underline{H}^{n-1/2}}{\Delta t} \ , \text{ and} \tag{2.30}$$
$$\left.\frac{\partial \underline{\xi_l}}{\partial t}\right|^{n} = \frac{\underline{\xi_l}^{n+1/2} - \underline{\xi_l}^{n-1/2}}{\Delta t} .$$

Additionally, we can define the mean values,

$$\underline{E}^{n+1/2} = \frac{\underline{E}^{n+1} + \underline{E}^{n}}{2} \qquad \text{and} \qquad \underline{\xi}^{n} = \frac{\underline{\xi}^{n+1/2} + \underline{\xi}^{n-1/2}}{2} \ . \tag{2.31}$$

Now, substituting these expressions in the equations 2.24, 2.26 and 2.27, and writing the new values as a function of the previous ones, we get the following finite difference equations,

$$\underline{\xi_l}^{n+1/2} = (2 + \Delta t \omega_l)^{-1} \left[(2 - \Delta t \omega_l) \underline{\xi_l}^{n-1/2} + \varepsilon_0 \Delta t \omega_l \underline{\underline{a_l}} \underline{E}^{n} \right] , \tag{2.32}$$

$$\underline{H}^{n+1/2} = \underline{H}^{n-1/2} - \Delta t \underline{\underline{\mu}}^{-1} \cdot (\nabla x \underline{E})^{n} \ , \tag{2.33}$$

$$\underline{E}^{n+1} = [(1/\Delta t)\underline{\underline{\varepsilon}} + (1/2)\underline{\underline{\sigma'}}]^{-1}$$
$$\left\{ (\nabla x \underline{H})^{n+1/2} + [(1/\Delta t)\underline{\underline{\varepsilon}} - (1/2)\underline{\underline{\sigma'}}]\underline{E}^{n} + \sum_{l=1}^{L} \omega_l \underline{\xi_l}^{n+1/2} - \underline{J}_s^{n+1/2} \right\} , \tag{2.34}$$

where,

$$\underline{\underline{\sigma}}' = \underline{\underline{\sigma}} + \varepsilon_0 \sum_{l=1}^{L} \omega_l \underline{\underline{a}}_l \ . \tag{2.35}$$

Notice that $\underline{H}^{n+1/2}$ and $\underline{\xi}_l^{n+1/2}$ appear in the expression for $\underline{E}^{n+1}$, therefore, they must be computed (or updated) first. The curls of the fields, appearing in these equations, are computed using mid-point difference operators. For example, from figure 2.1 we can write,

$$\left.\frac{\partial E_z^n}{\partial x}\right|_{i+1/2} = \frac{E_z^n(i+1, j, k+1/2) - E_z^n(i, j, k+1/2)}{\Delta x}$$

and

$$\left.\frac{\partial H_y^{n+1/2}}{\partial z}\right|_{k} = \frac{H_y^{n+1/2}(i+1/2, j, k+1/2) - H_y^{n+1/2}(i+1/2, j, k-1/2)}{\Delta z} \ .$$

The other derivatives, needed to compute the curls, are obtained with analogous mid-point operators. Finally, the current density $\underline{J}_s$, which is the source of the electromagnetic fields, is injected into the model in accordance with the spatial distribution and temporal dependence of the density current in the transmitter antenna.

2.3.2 Convergence and stability conditions

An important aspect of finite difference schemes is to determine under which conditions they are stable and convergent. In this section, I discuss briefly the convergence and stability conditions for the finite difference technique presented.

Taflove and Brodwin (1975) showed that for non-lossy media, the stability condition for Yee's finite difference scheme can be expressed as,

$$\Delta t \leq \frac{1}{V_{\max}} \left[\frac{1}{(\Delta x)^2} + \frac{1}{(\Delta y)^2} + \frac{1}{(\Delta z)^2} \right]^{-1/2} , \tag{2.36}$$

where $V_{\max}$ is the maximum velocity of the waves in the model. The existence of this stability condition for this finite difference scheme guarantees its convergence (e.g., Ritchmyer & Morton, 1967), and therefore, a convergent approximate solution exists (Issacson and Keller, 1966). However, since we are considering lossy media, extra considerations must be taken into account.

For simplicity, let us suppose that the media, in our model, are isotropic. Then, from equation 2.34 we can see that, to avoid numerical oscillations of the electric field at each time step, the coefficient of the electric field must be positive, i.e.,

$$\frac{1}{\Delta t}\varepsilon > \frac{1}{2}\sigma' , \tag{2.37}$$

which can be rewritten as,

$$\frac{1}{\pi}\omega_{num}\varepsilon > \sigma' , \tag{2.38}$$

with $\omega_{num} = \dfrac{2\pi}{\Delta t}$.

Notice that equation 2.38 is similar to the physical condition $\omega\varepsilon > \sigma$, characteristic of the so-called propagation regime. This suggests that by satisfying equation 2.38 we guarantee that the finite difference scheme will still represent the numerical solution of a wave equation. If there are no losses in the media, this condition is immaterial since it implies that $\Delta t < \infty$. Equations 2.36 and 2.37 define upper bounds for Δt, but only one (the smaller) will effectively define the maximum value allowed for Δt. Since we are interested in modeling propagating waves, the losses in the media will generally be moderate to low, and therefore, we expect that the condition expressed by equation 2.36 will, in general, set the effective upper bound for Δt.

In GPR applications, the medium with maximum phase velocity will be the air, and so $V_{\max}$ in equation 2.36 will be the velocity of the electromagnetic waves in the air. Since the losses in the air are very small for the frequency band of the GPR technique (i.e., $\sigma'_{air} \approx 0$), $V_{\max}$ will be independent of the frequency. On the other hand, the spatial grid size (Δx, Δy and Δz) determines the accuracy of the technique, and therefore, these values must be smaller than the minimum wavelength of the GPR signal in the media. Taflove and Umashankar (1989) have indicated that, to obtain a reasonable accuracy, the grid size should be chosen smaller than 1/10 of the minimum wavelength of the signal in the media. Choosing an even smaller grid size will increase the accuracy and decrease the effect of numerical dispersion, but also will increase the total computing time. In non-lossy media, the minimum wavelength corresponds to the maximum frequency of the GPR spectrum. However, in lossy media, we must take into account the variation of the phase velocity with frequency. If we suppose that the frequency band of the GPR technique is finite, then the following expression can be used to estimate a lower limit "λ_{m}" for the minimum wavelength of the signal in the media,

$$\lambda_{\mathrm{m}} \equiv \left[V(\nu,\vec{r})\right]_{\min} / \nu_{\max} \leq \left[V(\nu,\vec{r})/\nu\right]_{\min} \ , \tag{2.39}$$

where $\left[V(\nu,\vec{r})\right]_{\min}$ is the minimum phase velocity of the media in the frequency band of the GPR signal, and $\nu_{\max}$ is the maximum frequency of the signal (i.e., the upper limit of the GPR frequency band). In isotropic and dielectrically dispersive media, the phase velocity can be estimated by,

$$V(\nu) = \frac{\sqrt{2}}{\sqrt{\mu\varepsilon(\nu)}}\left[1+\sqrt{1+(\sigma'/\omega\varepsilon(\nu))^2}\,\right]^{-1/2} , \tag{2.40}$$

where σ' is given by a scalar version of equation 2.35. If the medium is anisotropic, the analysis is, in general, more complicated. However, for simple anisotropic media (e.g., uniaxial media), equation 2.40 can still help us to estimate the minimum phase velocity by using the properties of the media for different directions of propagation and polarizations.

2.4 MODELING RESULTS

2.4.1 Radiation pattern of a finite electric dipole antenna

I present two examples of 3D modeling. The first is the radiation pattern of a finite electric dipole in a homogeneous and isotropic medium; and the second is the radiation pattern of a dipole antenna in a system of two semi-infinite isotropic media. The intention of the first example is to compare the results with existing analytical solutions. The second example is more interesting since it corresponds to the common case of an air-soil interface. In this case we can also verify if the radiation pattern obtained with the finite difference technique agrees with the analytical far-field solution for this case (Engheta, et. al., 1982) and, at the same time, study the characteristics of the air and ground direct waves that are commonly observed in GPR data. I do not consider anisotropic media in these 3D examples because they are computationally very expensive. However, to show some effects that anisotropy can produce on GPR data, in the next section I present an example of anisotropic media using a 2D modeling scheme.

Figure 2.2(a) shows the orientation of the electric dipole antenna and Figure 2.2 (b), (c) and (d) show its radiation pattern (snapshot) in a homogeneous and isotropic medium. Notice that the intensity and form of the wave front coincides with the theoretical prediction for the radiation pattern of an electric

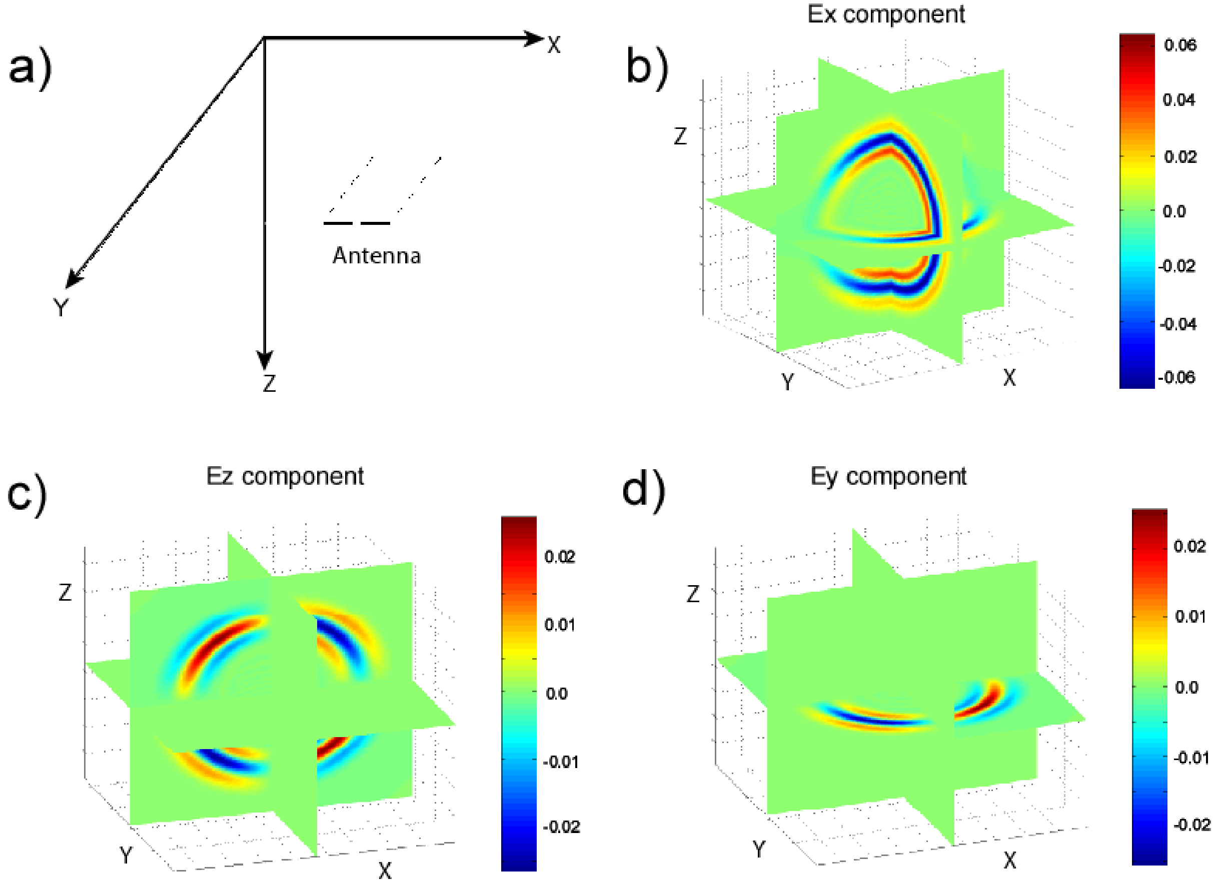

Figure 2.2. Snapshots of the three components of the electric field computed with the FDTD technique. (a) Electric dipole placed in the center of the volume and oriented parallel to the "X" axis. The medium is isotropic and homogeneous ($\varepsilon_r=2$, $\mu_r=1$, $\sigma=0$) and the volume has dimensions 5m x 5m x 5m. The snapshots correspond to the instant 10 ns. The current applied to the dipole is a squared hanning window of duration 5 ns. The results are in agreement with the analytical solution (small electric dipole).

dipole (e.g., Jackson, 1975). For example, the E_x component is symmetric around the axis of the antenna and becomes zero on the axis. On the other hand, the E_y and E_z components show the change of phase expected at the plane perpendicular to the axis of the antenna and pass through the middle of it. In conclusion, these results coincide with the theoretical characteristics expected for the radiation pattern of an electric dipole in an isotropic and homogeneous medium.

Figure 2.3 shows a snapshot of the "x" component of the electric field (i.e., E_x) for a two media model, simulating an air-soil interface. The upper media has $\varepsilon_r = 1.0$ and the lower media has . $\varepsilon_r = 8.0$ ($\mu_r = 1$ and $\sigma = 0$ for both the media). The antenna is placed at 5 cm above the surface (horizontal plane in the figure) and oriented along the "x" axis. Some interesting features can be noticed in this figure. First, the amplitude of E_x has a maximum in the vertical direction of propagation and reduces toward the horizontal direction of propagation (both along the "x" and "y" axis). This happens for the air direct wave as well for the ground direct wave. However, the focusing of the ground wave in the vertical direction is more pronounced (this is in agreement with Engetha's equations for the radiation pattern). Second, notice that the air wave is not totally equal to zero on the soil surface and is refracted at a critical angle inside the soil (indicated as A). Third, notice that the evanescent waves (indicated as C and C') are generated in the air by the direct ground wave. These waves (C and C') are the ones that we will detect on the surface as "ground waves". Finally, indicated as B is a point where E_x becomes minimum in the "zy" plane (also called "E" plane) and indicates a direction (from the center of the antenna) that is approximately perpendicular to the wave front of the refracted air waves traveling

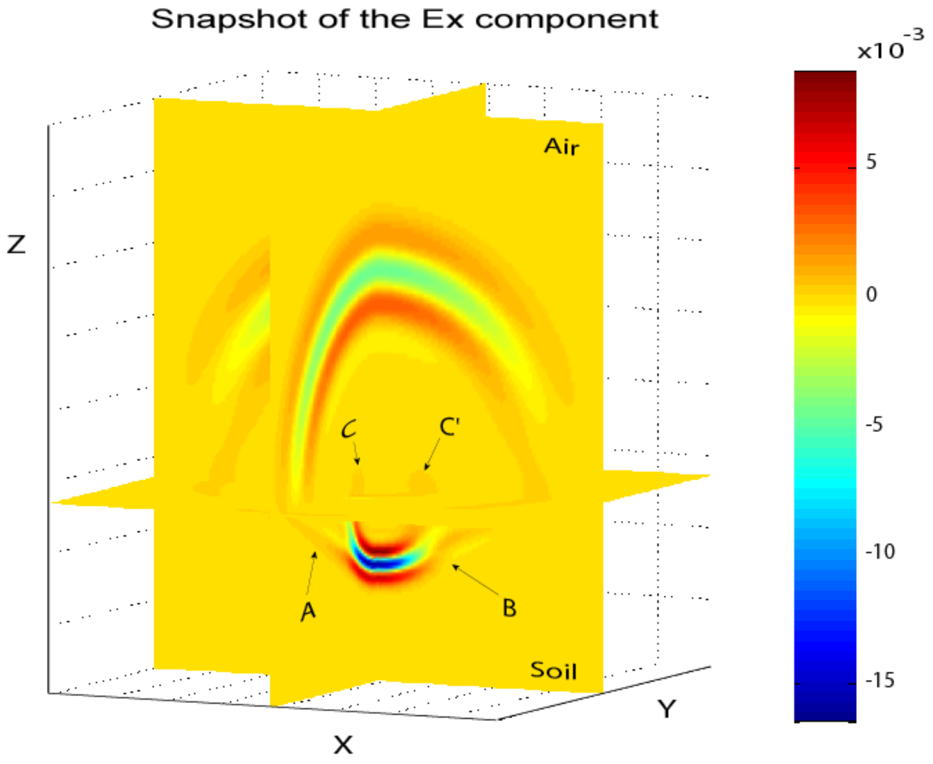

Figure 2.3. Snapshot of the "x" component of the electric field produce by a dipole antenna placed very close to the air-soil interface. The synthetic data was generated with the implemented 3D explicit FDTD technique. The air-soil interface is located at the same level than the shown horizontal plane and the snapshot corresponds to the instant t= 10 ns. The antenna is in the center of the volume, and is oriented in the "x" direction. See main text for the explanation of the pointed features.

in the ground, i.e., in the direction of the critical angle. However, this minimum is not very well defined in the internal part of the ground wave, where there is a reduction of amplitude, but it does not show any appreciable maximum between this direction (of minimum amplitude) and the horizontal direction. The observed reduction of amplitude at the critical angle (“zx” plane) is related to the destructive interference between the ground wave and the refracted wave in the subsurface, while the maximum observed at the critical angle in the “zy” plane (also called “H” plane) corresponds to a constructive interference between these two waves (note the polarity of the waves at the points where they join).

To see the interference in more detail and compare these results with previous work on modeling the radiation pattern with the FDTD technique, Figure 2.4 shows the snapshots of the “zx” and “zy” planes, separately. The first aspect to notice in these figures is the focusing of the radiation pattern into the soil. These results are in very good agreement with those presented by Lampe et. al. (2003) and confirm that the Engheta’s (1982) or Smith’s (1984) far field approximations do not describe accurately the near field radiation pattern of a antenna placed very close to the air-soil interface. The second aspect to notice is the different characteristics of the refracted waves, i.e., the way that the refracted wave in the subsurface and generated by the air wave is different (in the “zx” plane the refracted wave appears to be associated with the tailing part of the wave front in the air, whereas in the “zy” plane the refracted wave appears to be associated with the frontal part of the air wave front). Secondly, in the “zx” plane the refracted wave has opposite phase relative to the ground wave at the point where they merge, producing a destructive interference between them, whereas in the “zy” plane these waves have the same phase at the point where they merge, producing a constructive interference between them. In both the cases, the angle defined by the contiguous points where the merging occurs corresponds to the so called critical angle. These results are qualitatively in agreement with Engheta and Smith’s equations, but the exact variation of the amplitude is not completely in agreement as already pointed out in Lampe et. al. (2003). For reference, Figure 2.5 shows the results (FDTD and Engheta’s radiation pattern) presented by Lampe et. al. (2003) for a small dipole. Compare the snapshots in this figure with those presented in Figure 2.4.

In Figure 2.6, I present a radargram that shows what an experiment will look like if we record the E_x component along the “y” axis and at the same height as the source above the air-soil interface. In this case, I modified the size of the volume to make the “y” dimension larger (10 m), the “x” and “z” dimensions shorter (5 and 3.25 m, respectively), and placed the air-soil interface at 0.5 m from the bottom boundary of the model. Additionally, I didn’t used absorbing boundary conditions so that we can observe the reflection coming from the bottom and walls of the model. The other parameters of the model are the same as in the previous experiment. The data were normalized and clipped (clipping level equal to 0.015) to be able to observe (at far offsets) the signals related to the

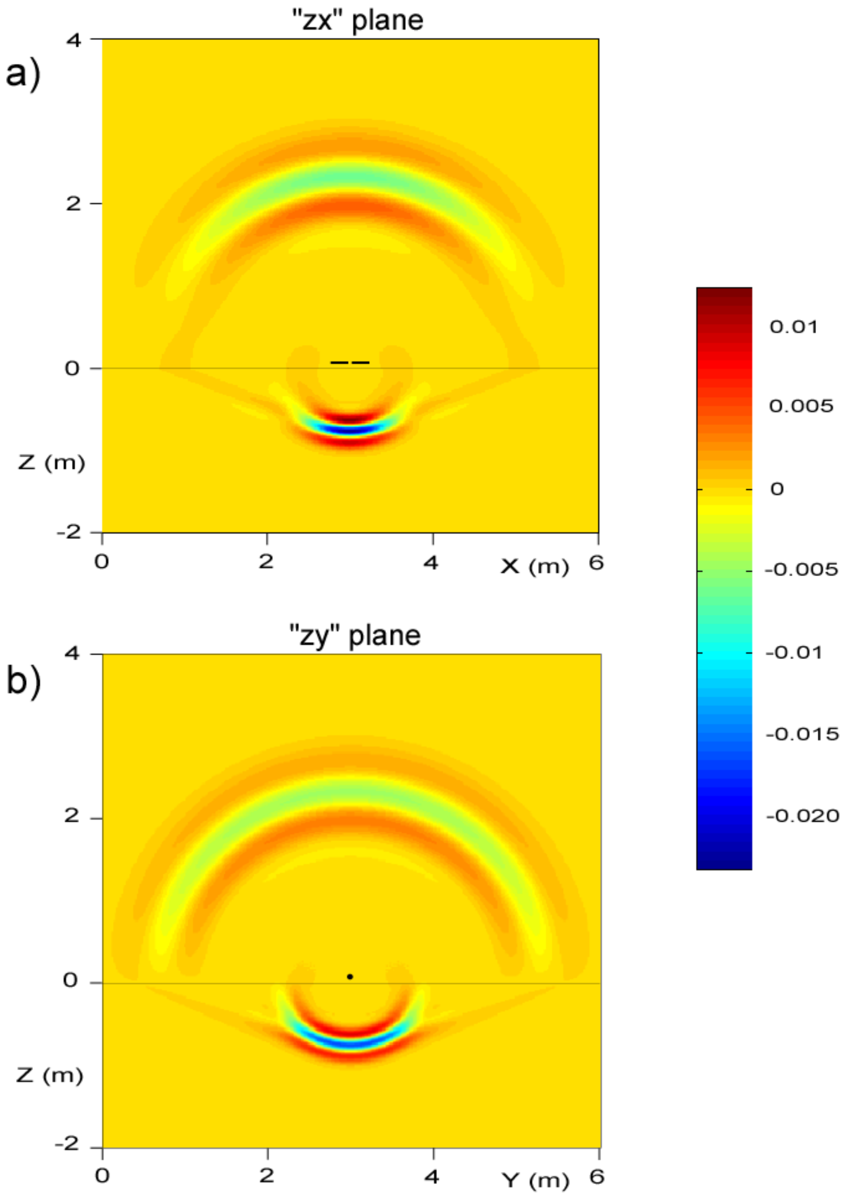

Figure 2.4. Detail of the snapshot shown in Figure 2.3. (a) Snapshot in the "E" plane ("zx" plane), and (b) snapshot in the "H" plane ("zy" plane). The location and orientation of the antenna is also shown in both the figures.

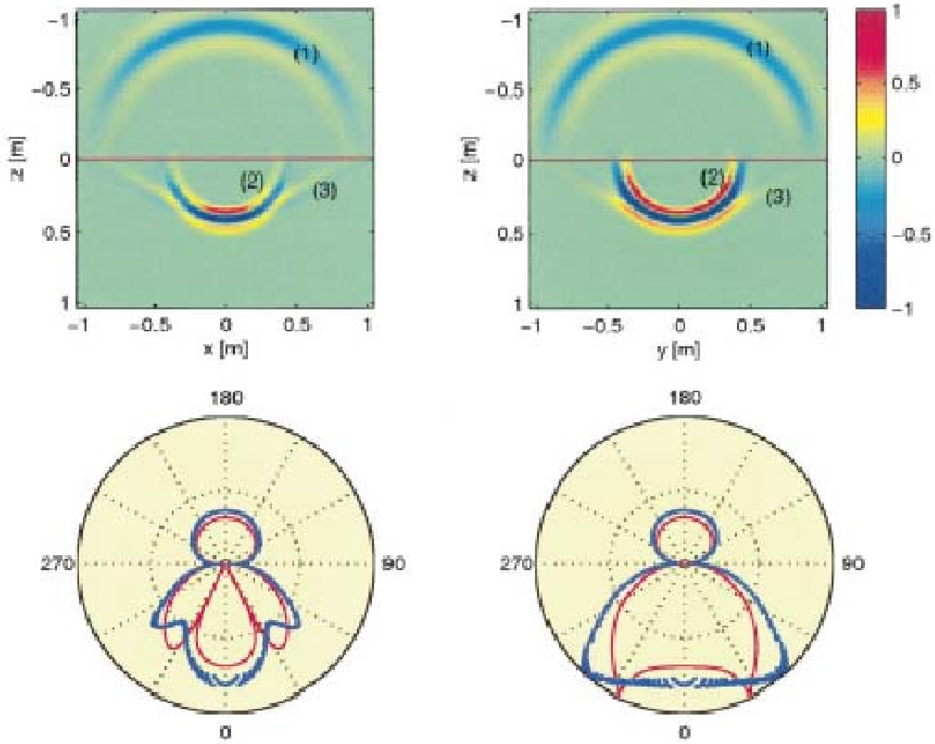

Figure 2.5. Results presented by Lampe et. al. (2003) (Figure 6, page 976) for the radiation pattern of an infinitesimal electric dipole placed above the air-soil interface. " (Top) E plane (left) and H plane (right) snapshots of the electric field E_x component radiated from an infinitesimal dipole located one grid cell above an interface between air and lossless soil ($\varepsilon = 5\varepsilon_0$, $\mu = \mu_0$, $\sigma = 0$ mS/m). The dipole is oriented parallel to the x-axis. Spherical waves in the upper (1) and lower (2) half-space and head waves (3) in the lower half-space are visible. (Bottom) Amplitude radiation patterns (blue) for the tangential components of the electric field, E_θ (left) and E_ϕ (right) in the E and H planes, respectively. Recording distance is 1 m. Red lines show corresponding asymptotic radiation patters for far-field [equations (46a)-(46d) in Smith, 1984]. Data are normalized with respect to the maximum amplitude ".

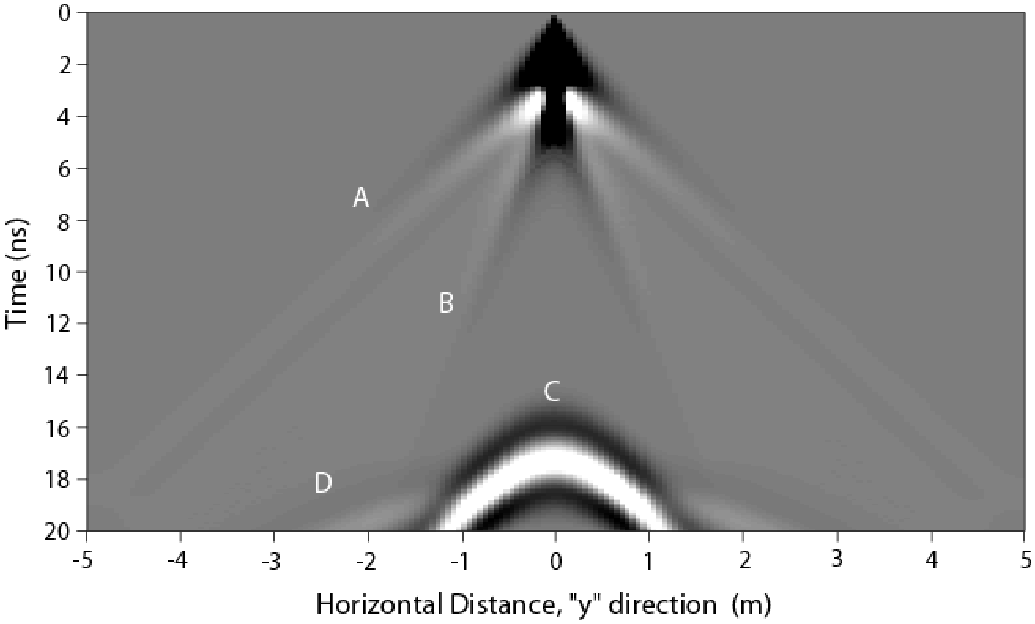

Figure 2.6. Shot record of the E_x component received at the same level of the antenna (above the air-soil interface). The configuration is analogous to the one used in Figure 2.4, but in this case the dimensions of the numerical volume are different (x=5m, y=10m and z=3.25m). The soil occupies the lower 0.75 m of the model. See main text for details.

direct air wave and the so called direct ground wave signals. The latter are produced, in reality, by the evanescent waves (C and C' in Figure 2.3) that are generated in the air by the direct ground wave. Notice that very close to the antenna the direct air wave (indicated as A) is so strong that it is completely clipped. The signal reflected from the bottom boundary of the model (indicated as C) has also been clipped, but its maximum peak value is about 0.04 times the amplitude of the direct air wave close to the antenna. The reflection indicated as D is a direct air wave reflected at the "zy" walls of the model and has very small amplitude because of the radiation pattern of the antenna (see Figure 2.3). Notice that the reflection from the bottom of the model (indicated as C) has the velocity of the radar signal in the soil, i.e., it approaches asymptotically the direct ground wave signal (indicated as B), whereas the reflection from the "yz" walls has the velocity of the radar signal in the air. If the recording time were longer, all other reflections coming from the different boundaries of the model could be seen.

2.4.2 Example of GPR data in anisotropic media

The most common anisotropy found in geologic media is transverse isotropy (TI), i.e., uniaxial media with its axis of symmetry oriented in the vertical direction ("z" axis). If the axis of symmetry is tilted, then the medium is called tilted transverse isotropic (TTI). In this section, I present an example of GPR data in TI homogeneous media, for which I have implemented a simplification of the technique for 2D media and transverse electric (TE) mode. In this modification, the source is a hypothetical infinite line current on the horizontal direction ("y" axis). Since the media is TI, the anisotropic tensors are diagonal, i.e.,

$$\underline{\underline{\varepsilon}} = \varepsilon_0 \begin{pmatrix} \varepsilon_\perp & 0 & 0 \\ 0 & \varepsilon_\perp & 0 \\ 0 & 0 & \varepsilon_\parallel \end{pmatrix} \qquad \underline{\underline{\mu}} = \mu_0 \begin{pmatrix} \mu_\perp & 0 & 0 \\ 0 & \mu_\perp & 0 \\ 0 & 0 & \mu_\parallel \end{pmatrix} \qquad \underline{\underline{\sigma}} = \begin{pmatrix} \sigma_\perp & 0 & 0 \\ 0 & \sigma_\perp & 0 \\ 0 & 0 & \sigma_\parallel \end{pmatrix}, \quad (2.41)$$

and therefore, the components of the electric field are decoupled from each other. This means that the “y” component of the electric field (generated by the infinite line current) will not produce any electric field in the “x” or “z” directions, i.e., the transverse electric (TE) and magnetic (TM) modes are still decoupled, and therefore, the transverse electric (TE) mode, which has only the components E_y, H_x and H_z different from zero, can exist independently, and for this particular source and media, only the magnetic anisotropy will affect the propagation of the electromagnetic waves (i.e., $\varepsilon_{\|}$ and $\sigma_{\|}$ do not affect the propagation because E_x and E_z are zero).

Figure 2.7 shows the models used in this example. Each model consists of two non-conductive layers with the same electric permittivities but different magnetic permeabilities. Three different cases are considered to observe the different propagation behavior and character of the reflection at the interface. The current (source) used in this example was a squared hanning window with duration equal to 5 ns. Notice that only the $\varepsilon_{\perp}$ component is given since $\varepsilon_{\|}$ does not affect the propagation of the waves in the TE mode.

To see the temporal evolution of the propagating wave, Figure 2.8 shows three snapshots of the electrical field corresponding to 10 ns, 20 ns and 30 ns for model I. We can clearly see the elliptical form of the wave front in the upper medium (anisotropic) with its major axis along the vertical direction [in this direction of propagation, the magnetic field only has horizontal component (H_x)

and therefore the velocity of the wave in that direction is defined by μ_{xx} $(=\mu_\perp$ in VTI media)], whereas in the lower medium (isotropic) the wave front of the transmitted wave is symmetric (i.e., circular). It is also very interesting to notice that for normal incidence there is no reflection at the interface between the two media and, when the angle of incidence increases, so does the magnitude of

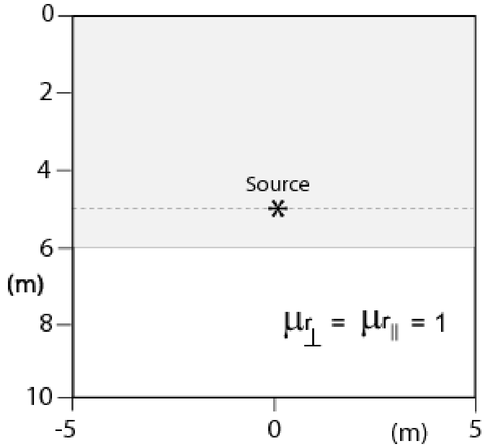

	Model I	Model II	Model III
$\mu_{r_\perp}$	1	4	2
$\mu_{r_\parallel}$	4	1	2

For all the models and media

$\varepsilon_{r_\perp} = 4$ $\sigma_\perp = 0$

Figure 2.7. Models and geometry used to show the results of the FDTD modeling algorithm in anisotropic media. The permittivity and conductivity are uniform through the models. The magnetic permeability of the lower medium is the same for all the model. Only the magnetic permeability in the upper media is different in each model. The dashed line is the location of the receiver antennas in the experiment.

the reflection. Again, this is explained by the fact that, for the vertical direction of propagation the magnetic field of the wave has only a horizontal component, therefore the contrast of impedance affecting the wave will depend in the variation of μ_{xx}. Since μ_{xx} is equal in both the media (as well as the electric permittivity and conductivity) the wave does not encounter any change of impedance for normal incidence. As soon as the angle of incidence begins to increase, the H_z component increases and the change of μ_{zz} $(=\mu_{\|}$ in VTI media), and therefore of impedance, affects the incident wave generating the corresponding reflection. This result implies that anisotropy can affect considerably the AVO behavior of the reflection at the interface, and therefore, if there is any indication of anisotropy in the media, it should be taken into account for interpretation and inversion.

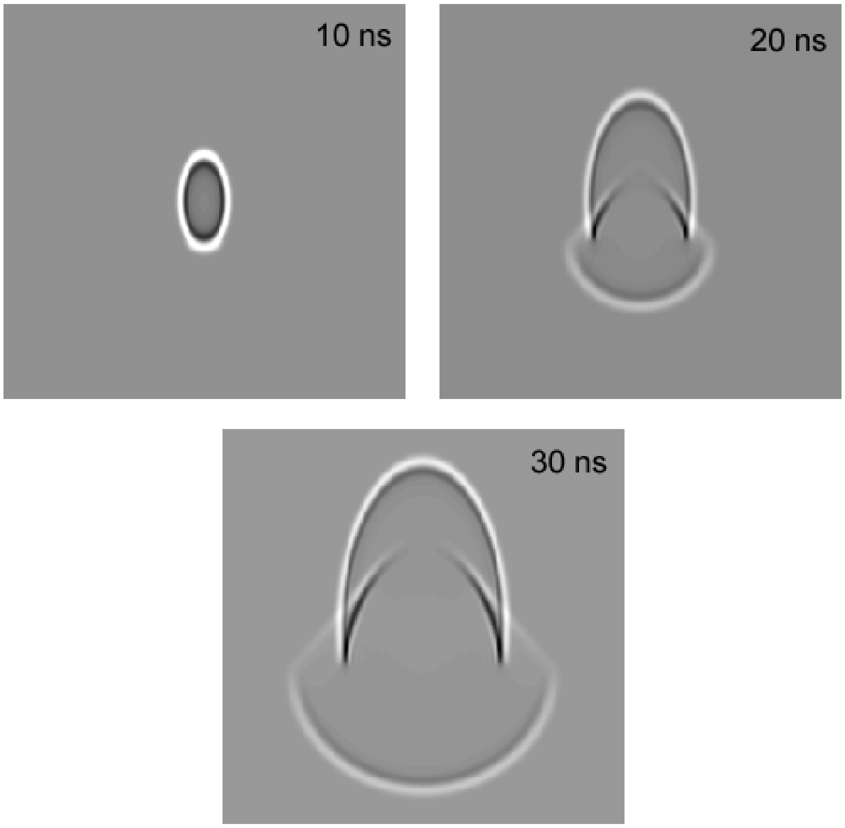

Figure 2.8. Three consecutive snapshots of a wave, originating at the source position, propagates through the layers of model I (see Figure 2.7). Notice the elliptical form of the wave front in the upper media due to anisotropy in that layer.

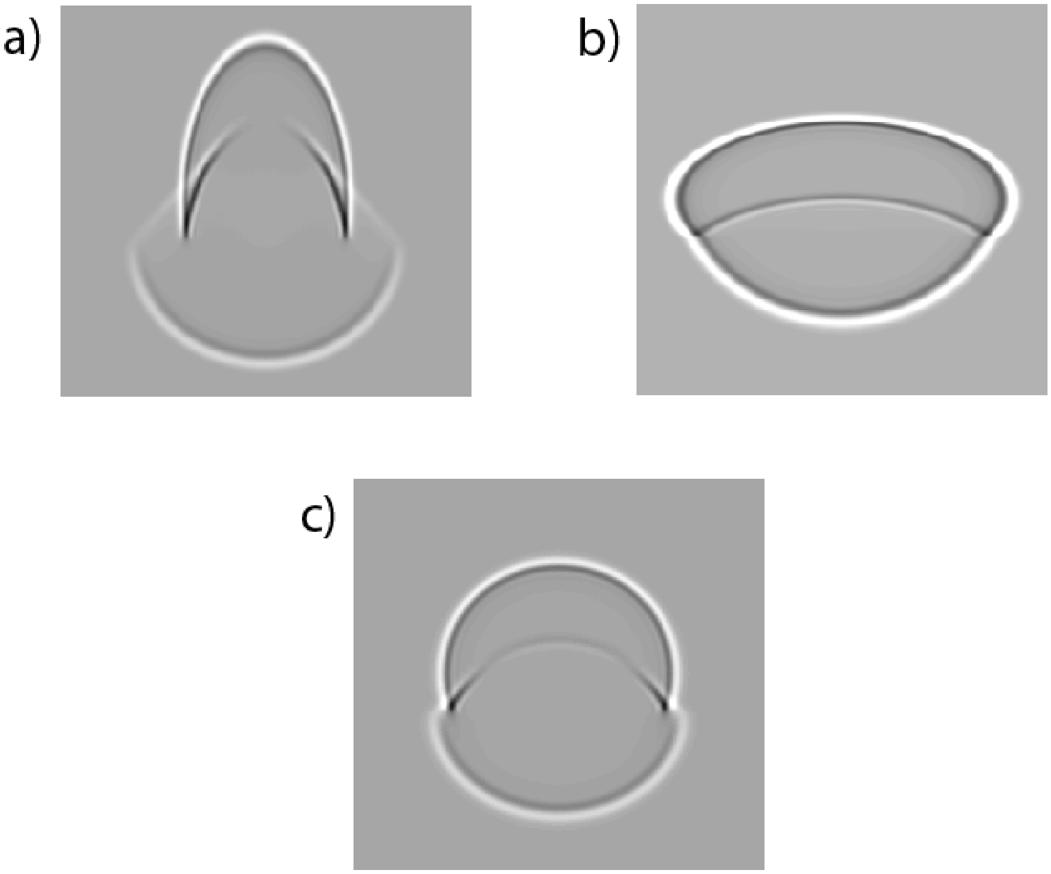

Figure 2.9. Snapshots at t=30 ns for the three different models presented in Figure 2.7. (a) model I, (b) model II and (c) model III.

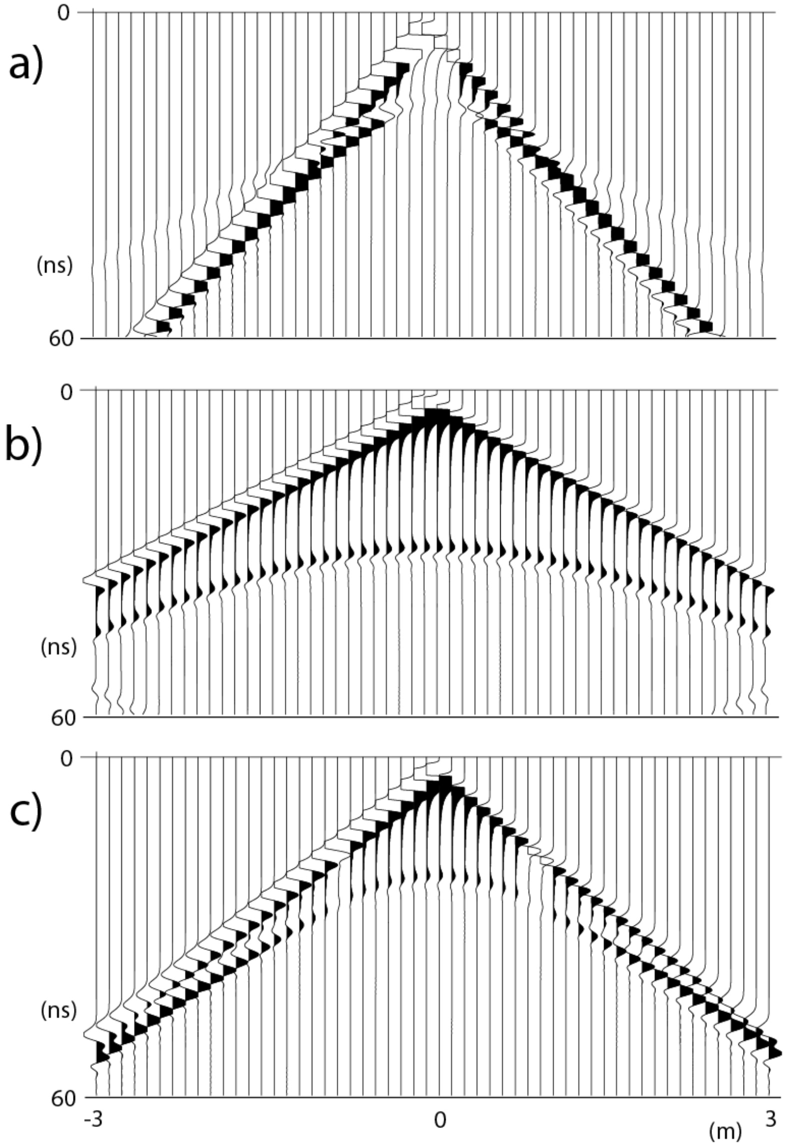

Figure 2.10. Traces recorded at the same level of the source in each model. In addition to the difference in velocity and non hyperbolic character of the reflection in the anisotropic models (a) and (b), notice the different AVO of each of these reflections. (a), (b) and (c) correspond to the models I, II and III presented in Figure 2.7, respectively.

Magnetic anisotropy is not often encountered in shallow exploration, but a similar effect will be observed if anisotropy of the electric permittivity or conductivity of the media are present (as for example, in fractured aquifers, fine stratification or anisotropic radar cross sections (RSC) due, for example, to the geometry of the scatterers). However, if the contrast with the encasing rock of all the elements of the conductivity tensor (in the reflector or scatterer target) is too high, the AVO anisotropic effect will be overcome by the almost unitary reflection coefficient obtained for all incidence directions.

Figure 2.9 shows the snapshots at 30 ns for the three models explained in Figure 2.6. Notice the difference between the forms of the wave fronts in the three cases. Model I and II have inverted values of the anisotropic magnetic permeability values, and therefore the wave front has inverted forms (the major axis of the ellipses are rotated from the "x" to the "z" axis), whereas Model III is isotropic and therefore the wave front is circular in both the media. Notice also how for model II the reflection coefficient at normal incidence in not zero (in contrast to model I). This is due to the fact that for model II the value of μ_{xx} changes from the upper to the lower media.

Finally, Figure 2.10 shows the shot records obtained with the receiver antennas located at the same "z" level of the source. Notice the difference in the phase of the reflections and their amplitude variations with offset (AVO), as well as the geometry of the reflections, which are non hyperbolic for the anisotropic media (one of the main criteria to recognize anisotropy in the media).

2.4.3 Example of GPR data in heterogeneous and conductive media

In most geologic media, heterogeneity and conductivity is usually more common and important than anisotropy. The conductivity of the media attenuates the GPR signal and can produce important dispersion effects, especially at low frequencies (see Chapter 4, section 4.3.1). In this section, I present an example of GPR signal propagation in heterogeneous and conductive 2D media. Again, the TE mode (described in the preceding section) is used to model the GPR data.

Figure 2.11 shows the model used in this simulation. The conductivity zone has a thickness equivalent to one skin depth computed at the dominant frequency of the GPR signal. Figure 2.12 shows six snapshots at 5, 25, 45, 55, 70 and 80 ns. Three important features can be noted in these snapshots. The first one is the amplitude reduction of the wave front when it travels through the conductive medium. The second one is not so evident, it is a small but perceptible refraction effect that can be noticed in the snapshot corresponding to 45 ns where a slight deflection of the wave front is observed at the bottom of the conductivity zone, which means that the conductivity produces a small but perceptible change of the velocity in the media. Third, notice the very small amplitude of the reflections that travel through the conductivity zone, in particular, the reflection coming from the dipping reflector whose amplitude will be almost negligible compared to the other reflections. This means that the attenuation produced by a conductivity zone whose thickness is equal to one skin depth (computed at the dominant frequency of the GPR signal) is already very strong. A set of models analogous to this one is used in Chapter 4 to test the migration algorithm for different thicknesses of the conductivity region.

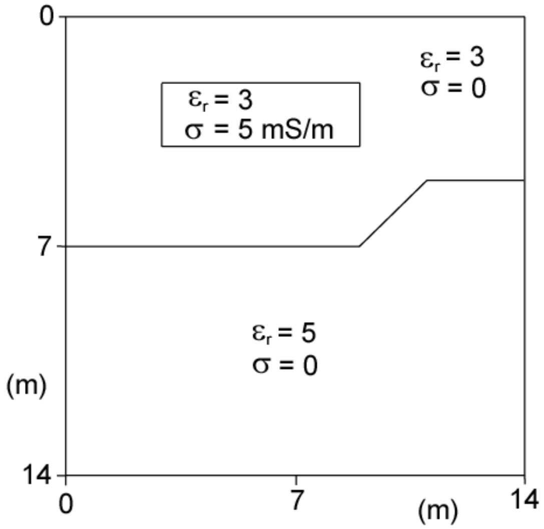

Figure 2.11. Model with a conductive region. It is used to show how electromagnetic waves are affected by conductivity losses in the media (especially with lateral variations). The thickness of the conductive region (2 m) is approximately equal to the equivalent skin depth of the region computed at the dominant frequency of the GPR signal used in this synthetic example (200 MHz).

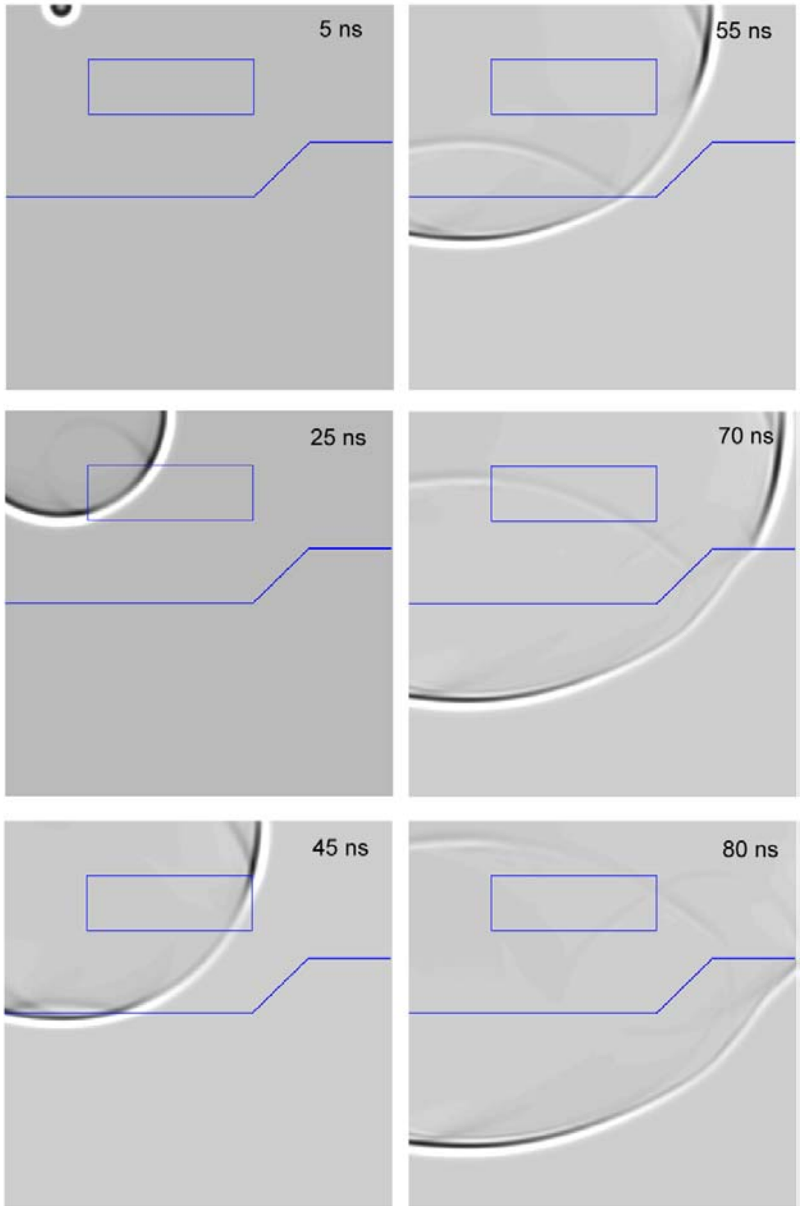

Figure 2.12. Consecutive snapshots of a GPR signal generated at the upper left side of the model. The contours represent the boundaries among the three different media in the model (see Figure 2.11) and are overlaid on the snapshots for reference.

2.4.4 Example of GPR data in heterogeneous and dielectrically dispersive media

Dielectric dispersion (and its related absorption) has been observed at different ranges of frequencies in soils and rocks (e.g., Sherman, 1988). In particular, Olhoeft and Capron (1994) and Hoekstra and Delaney (1974) have reported on dielectric dispersion for the frequency range of the GPR technique (MHz to GHz), and indicated that the dispersion mechanisms are probably related to interfacial (double layer) and molecular relaxations.

To demonstrate the effects of dispersion in GPR data, 2D modeling in dielectrically dispersive media is presented in this section. I used the so-called exploding reflection model (e.g., Yilmaz, 2001) in conjunction with the FDTD algorithm to generate a GPR zero offset section. The implementation of the exploding reflector model is important because it allows us to generate efficiently this type of section, making the FDTD modeling technique practical for testing migration algorithms of zero offset sections or for qualitative interpretation of real data.

To select the parameters of the dispersive medium in our model, I used the results of Olhoeft and Capron (1994). They analyzed different soil mixtures of clay and silica with different percentages of water content. The Cole-Cole parameters that they obtained for one of the samples are shown in Table 2.1. Notice that when the water content increases the resistivity decreases abruptly making the conductivity losses to rapidly overcome the dielectric absorption. For this sample no anisotropy was reported.

Water content (weight %)	ε_l	ε_∞	τ_ε (μsec)	α_ε	σ^{-1} (ohm-m)
0.0	3.46	2.65	0.0134	0.38	$> 10^4$
15.77	29.43	8.30	0.0183	0.66	56.0
30.18	43.04	20.73	0.0089	0.70	23.5
* 2.5	8.34	2.99	0.0152	0.44	$5.65\text{x}10^3$

* Interpolated data.

Table 2.1. Cole-Cole parameters for an engineering size-fraction clay soil (Olhoeft and Capron, 1994).

To estimate the Cole-Cole parameters at different water contents, I interpolated these data using quadratic functions, except for the resistivity, which I interpolated using an exponential function. In Table 2.1, the line with interpolated set of parameters is indicated with an asterisk.

Olhoeft and Capron obtained these parameters by fitting the spectral data to the Cole-Cole equation,

$$\varepsilon(\omega) = \varepsilon_0 \varepsilon_\infty + \frac{\varepsilon_0 (\varepsilon_l - \varepsilon_\infty)}{1 + (i\omega / \omega_\varepsilon)^{\alpha_\varepsilon}} - i\frac{\sigma}{\omega} ,$$

where ε_l and ε_∞ are the relative electric permittivities for low and very high frequencies, respectively; ε_0 is the electric permittivity of the vacuum, σ is the electric conductivity of the medium, α_ε is the relaxation exponent, and ω_τ is the relaxation frequency, which is related to the characteristic relaxation time τ_ε by $\omega_\varepsilon = 1/\tau_\varepsilon$.

To use these parameters, the Cole-Cole equation is approximated by a discrete superposition of Debye's mechanisms (e.g., Xu and McMechan, 1997),

$$\varepsilon(\omega) = \varepsilon_0 \varepsilon_\infty + \varepsilon_0 \sum_{l=1}^{L} \frac{a_l}{1 + \left(i\omega / \omega_l\right)} - i \frac{\sigma}{\omega} \ ,$$

where ω_l are the relaxation frequencies of the Debye's mechanisms related to the characteristic relaxation time τ_l by $\omega_l = 1/\tau_l$, and $a_l = \varepsilon_s^l - \varepsilon_\infty$ are the relative permittivity weighting factors associated with each mechanism (see equation 2.21).

In practice, most of the energy of the radar signal is contained within a determined frequency band and three Debye's mechanisms constitute a very good approximation of the dispersion curve in such a frequency band (see Figure 2.13). Adding more Debye's mechanisms will improve the representation of the dispersion curve but has the drawback of increasing the number of memory variables (and related parameters) in the modeling algorithm. Table 2.2 shows the Debye's relaxation frequencies and weighting factors corresponding to the fitting of the Cole-Cole curve shown in Figure 2.13.

a_1/ε_∞	a_2/ε_∞	a_3/ε_∞	ω_1 (Hz)	ω_2 (Hz)	ω_3 (Hz)
0.5899	0.6112	0.3164	1.3×10^7	2.47×10^8	7.15×10^9

Table 2.2. Debye's parameters corresponding to the fitting of the dispersion curve shown in Figure 2.13.

Figure 2.13(a) shows the magnitude of the real and imaginary parts of the complex wave number, i.e., the product of angular frequency and the slowness, computed with the Cole-Cole equation and corresponding to a soil with 2.5% water content (see Table 2.1). I also show the curves obtained with three Debye's mechanisms (Table 2.2), and the curves corresponding to a conductive media without dielectric dispersion and relative electrical permittivity equal to 5 and resistivity equal to 213 ohm-m. The imaginary part of the complex wave number corresponds to the so-called attenuation factor "α" (the inverse of "α" is the so-called skin depth "δ"). The real part of the complex wave number is related to the propagation of the waves and, for non-dispersive media, the slope of this curve (in log-log scale) should be equal to one. Notice how the superposition of three Debye mechanisms approximates the Cole-Cole curve in this frequency band, and also how for frequencies above 30 MHz, the attenuation factor of the media without dielectric dispersion does not change appreciably with frequency and the slope of the real part of the product approaches one asymptotically when

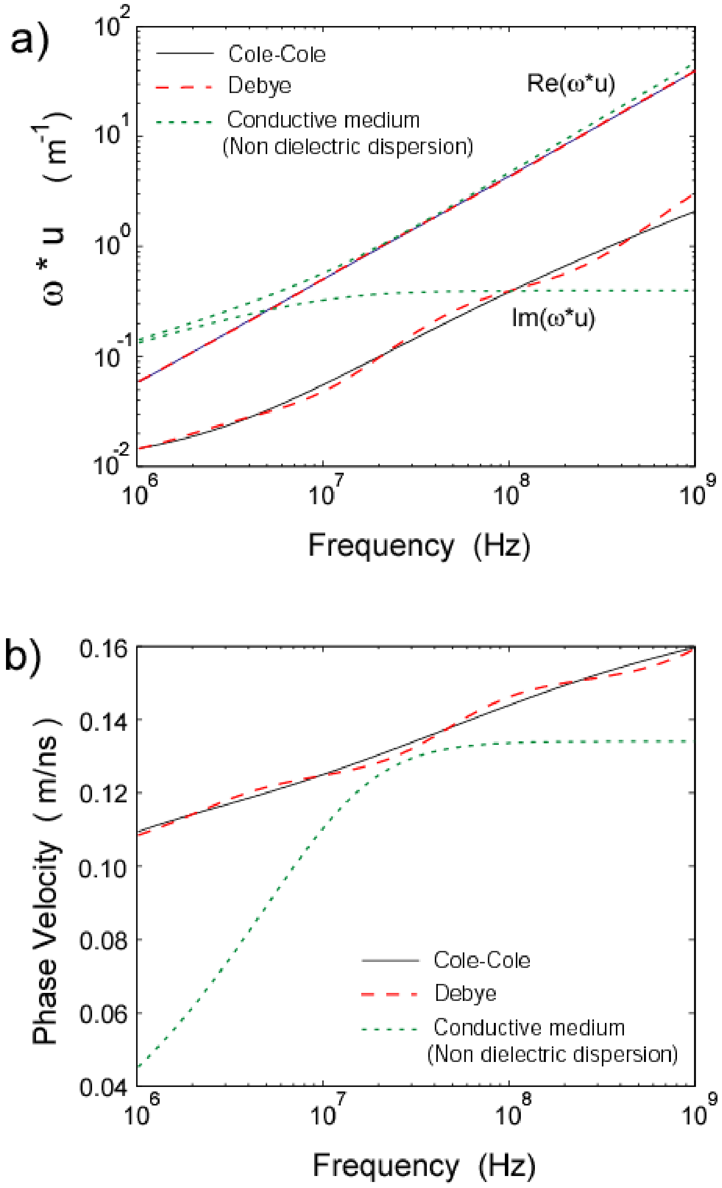

Figure 2.13. (a) Magnitude of the real and imaginary parts of the product of the angular frequency by the slowness as a function of frequency for a medium with dielectric dispersion and another medium without dielectric dispersion. (b) Phase velocity as a function of frequency for the same media shown in (a).

the frequency increases. On the other hand, for the dielectric dispersive medium the attenuation factor changes by one order of magnitude when the frequency increases from 20 MHz to 300 MHz; in addition, the slope of the real part of the product does not approach one asymptotically when the frequency increases. Figure 2.13(b) shows the corresponding phase velocities computed for the cases presented in Figure 2.13(a). Notice how the phase velocity changes in the entire frequency band for the medium with dielectric dispersion, whereas for the medium without dielectric dispersion, the phase velocity reduces appreciably for frequencies below about 60 MHz. In this way, the dispersion effect due to the conductivity of the media is important when the dominant frequency of the radar signal approaches the limit between the diffusion and propagation regimes.

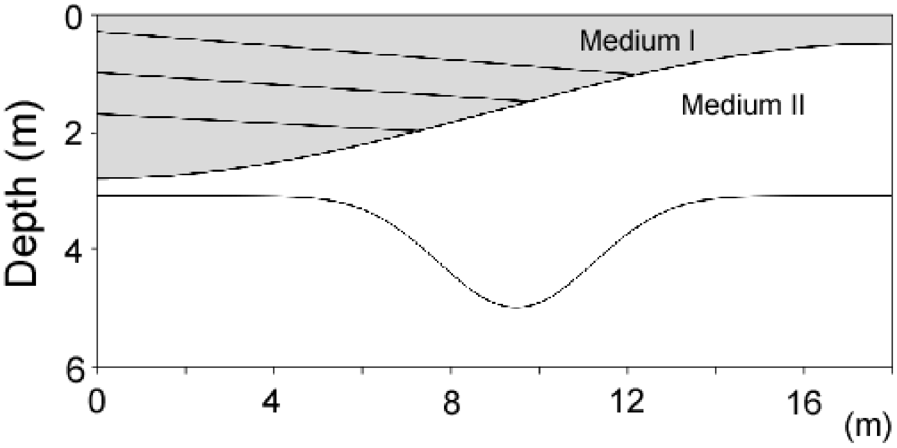

Figure 2.14. Model with dispersion, conductivity and lateral variation. It is used to generate the synthetic shown in Figure 2.15. Medium I is slightly conductor and has dielectric dispersion. The lines overlapped in the model are the loci of source injection in the exploding reflector model.

Figure 2.14 shows the model used to generate the synthetic data. The model is composed of two homogeneous media with an interface that is not horizontal. The medium (I) corresponds to the soil with 2.5% water content (discussed above) and Debye's parameters shown in table 2.2. On the other hand, medium II is non-dispersive and non-conductive, and has a relative electric permittivity equal to 4. The lines shown on Figure 2.14 are exploding reflectors introduced in the model. One of the reflectors coincides with the real interface between the two media. The wavelet is the derivative of a squared hanning window with a duration of 10 nanoseconds, and so, a dominant frequency of 100 MHz.

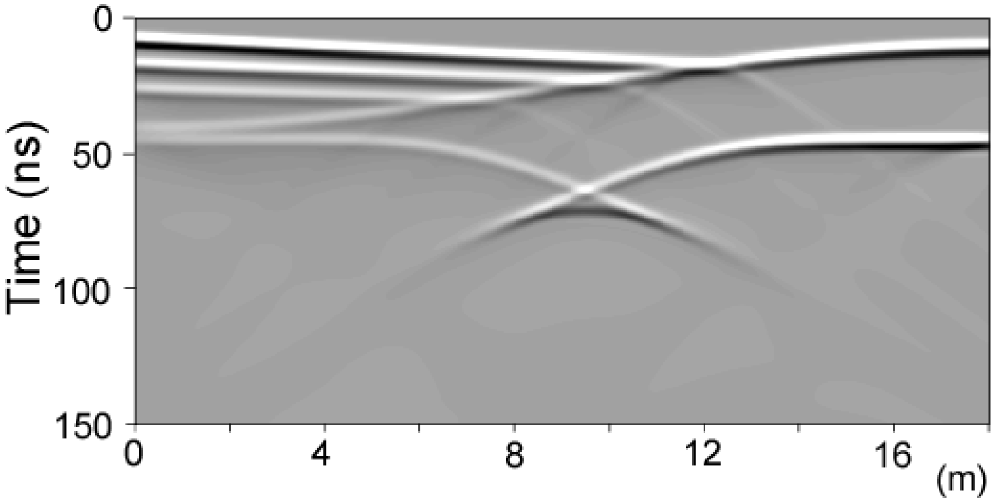

Figure 2.15. Synthetic zero offset section obtained for the model shown in Figure 2.14. Notice the effects that dielectric dispersion can produce on the GPR signal.

Finally, Figure 2.15 shows the zero offset section obtained for the model in Figure 2.14. Notice how the amplitude, travel time and wave form of the GPR data are affected by the dispersion mechanisms in the medium. For example, the width (of the wavelet) and amplitude of the reflection coming from the deeper reflector changes appreciably along the section, showing the effects produced by the dielectric dispersion and different thickness of the upper medium. In Chapter 4, I use this synthetic result to test the new migration technique and show how it allows us to take into account these effects due to dispersion and lateral heterogeneities.

2.5 SUMMARY

I have presented an explicit finite difference time domain (FDTD) technique for modeling GPR data in dispersive, heterogeneous and anisotropic media. In most geologic media, dispersion effects are produced by dielectric absorption and conductivity in the media. The dispersion effects produced by dielectric absorption are introduced in the FDTD modeling technique using memory variables, which are associated with the so-called Debye's mechanisms. The electric conductivity in most geologic media does not change with frequency (up to and including the band of frequencies used for the GPR technique). Therefore, the dispersion related to this parameter is only associated with Joule's effect. This dispersion is important because it defines, in practice, the lower frequency limit for the GPR technique (the so-called limit between the propagation and diffusion regimes).

In dispersive and conductive media, the stability condition is defined by the electric permittivity, the conductivity and dielectric absorption in the media (equations 2.36 and 2.38). The upper limit for the time step interval, defined by equation 2.38, is necessary to avoid numerical oscillation of the electric field at each time step. If the losses in the media are very small, the limit defined by equation 2.38 is irrelevant and equation 2.36 effectively defines the limit for Δt. However, as the dominant frequency of the GPR signal approaches the limit between the diffusion and propagation regimes ($\omega\varepsilon \approx \sigma'$), equation 2.38 becomes more important, and care must be taken to guarantee that this condition is also satisfied. On the other hand, to compute the minimum value of the phase velocity in the media, we must be take into account the equivalent conductivity "σ'"of the media, which is produced by Joule's losses and dielectric absorption in the media.

I presented two simple 3D modeling examples of GPR data. They were used to test the validity of the technique. However, the explicit FDTD technique for 3D modeling is numerically very expensive, especially when increasing values of the electric permittivity are used. Implementing the FDTD technique for 2D media and transverse electric (TE) mode, allow us to obtain an approximate GPR response for the commonly used broadside perpendicular acquisition mode. I have also implemented the exploding reflector model to be able to obtain, more efficiently, synthetic zero offset sections, which can be used to test new migration algorithms or for the qualitative interpretation of real GPR data.

The anisotropic examples shown in this chapter indicate that not only the geometrical locus of the reflections can be used as a criterion to detect anisotropy, but also the amplitude versus offset (AVO) behavior for different polarizations can be used with this purpose. A similar AVO behavior can also be expected from scatterers that have anisotropic radar cross section (RCS), and so, this information can be used to determine their geometry and orientation (supposing that these are the causes of the anisotropic RCS behavior). In particular, such AVO criteria could be used in conjunction with the Alford rotation technique to improve the accuracy on the estimation of the orientation of elongated targets.

Finally, the explicit FDTD technique will be used to compare the results of the reflectivity technique that I have developed for modeling GPR data in 1D media. The reflectivity technique is presented in the next chapter.

Chapter 3: The Reflectivity Modeling technique

Horizontally layered media are often encountered in shallow exploration geophysics. Modeling of GPR data in these environments can be implemented by techniques that can be faster than a Finite Difference scheme because the lateral homogeneity of the media allows us to reduce the dependence on the horizontal spatial variables through Fourier transforms on those coordinates. The transformed system of equations will depend only on the vertical coordinate (depth) and, under the assumption of homogeneous layers, the system of differential equations can be solved analytically. I adapted the invariant embedding or reflectivity technique, originally developed by Kennett to model elastic waves in layered media, to model GPR data in layered isotropic media. This technique is useful not only for fast modeling of GPR data (which allows us to obtain a faster and quantitative interpretation of the GPR data), but also for model-based inversion of estimating rock properties that require a fast forward modeling technique. It can also be the basis for a hybrid modeling technique that can incorporate lateral heterogeneities of the media.

3.1 INTRODUCTION

Numerical modeling of GPR data is very important for interpretation and inversion. In chapter 2, I have shown that finite difference techniques allow us to obtain the response of general 3D heterogeneous and anisotropic media. However, finite difference techniques are computationally very expensive and require considerable computing resources (dynamic memory and CPU speed).

In stratified media, Fourier transforms of Maxwell's equations from the time to the frequency domain and from the horizontal coordinates to the wave number domains reduce them to a system of first order, ordinary differential equations whose solution can be obtained more efficiently than using a finite difference technique. This reduction of the wave propagation problem in layered media has been employed in many other areas, for example in acoustic and elastic wave propagation, electromagnetism and quantum mechanics (e.g., Chew, 1995). In order to solve the resulting system of first order, ordinary differential equations many particular schemes have been proposed. However, they all can be classified into two general categories: continued fractions or propagator matrix schemes.

Crook (1948) and Abeles (1950 presented a matrix formalism for modeling of electromagnetic waves, and Thomson (1950) presented a similar approach for modeling elastic waves in stratified media. Then, Haskell (1953) showed an application of this technique to obtain the dispersion equations of elastic surface waves and Wait (1953) developed a continued fractions technique to compute the transmission and reflection response of electromagnetic waves in layered media. These pioneering techniques were used during the subsequent years to model the elastic and electromagnetic responses of layered media. However, numerical instabilities associated with the propagator matrices algorithm (e.g., Gilbert and Backus, 1966), as well as the impractical aspects of the continued fractions approach, stimulated extensive investigation in this area. Fuchs and Müller (1971), and Kennett (1974) presented a new recursive technique for modeling elastic waves in stratified media that is unconditionally stable and, physically, more intuitive. In this technique, the wave field is decomposed into up-going and down-going waves, the response of the sub-systems is represented by up and down reflection and transmission matrices and recursive relations allow us to obtain the total transmission and reflection matrices of the whole system from its partial responses.

Ursin (1983) presented a general review of this technique for elastic and electromagnetic waves. However, he did not develop, in detail, the case corresponding to electromagnetic waves and small errors are present in the expressions of the eigenvector matrices given in the appendix.

In this chapter, I develop in detail the Fuchs and Kennett formalism applied to electromagnetic waves in layered isotropic media. Then, the results obtained with this technique are compared with the classical results of Fresnel's equations and the finite difference time domain algorithm presented in chapter 2. Finally, an application of this technique for interpretation of real GPR data (CMP gathers) is presented.

3.2 THEORY

3.2.1 The propagator matrix equation

In developing the invariant imbedding or reflectivity technique for electromagnetic waves in laterally homogeneous and isotropic media, I will follow a procedure analogous to that presented by Kennett and Kerry (1979) for elastic waves. The model to be considered is shown in Figure. 3.1. It is composed of a stack of homogeneous and isotropic layers, each one characterized by an electric permittivity "ε", an electric conductivity "σ" and a magnetic permeability "μ".

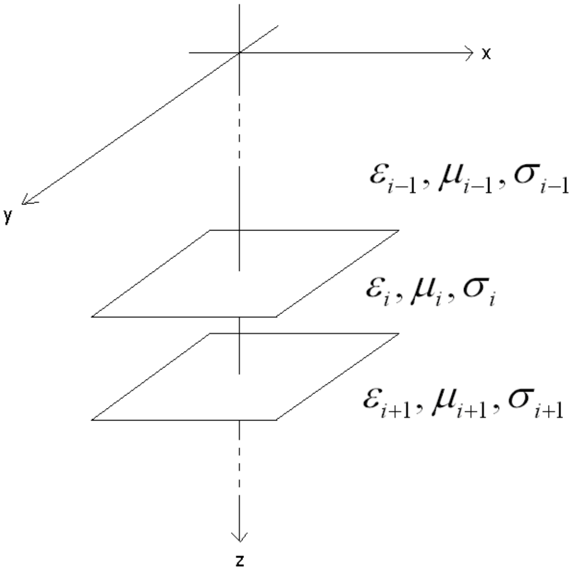

Figure 3.1. Layered system supposed in the reflectivity technique.

Then, Maxwell's equations in each layer can be written as,

$$\nabla x\underline{E} = -\mu \frac{\partial \underline{H}}{\partial t} \ , \tag{3.1}$$

$$\nabla x\underline{H} = \sigma \underline{E} + \varepsilon \frac{\partial \underline{E}}{\partial t} + \underline{J} \ ,$$

where $\underline{E}$ is the electric field, $\underline{H}$ is the magnetic field, and $\underline{J}$ is the current density (source). In these equations we have considered that the free charge density "ρ", in each layer, is zero.

Developing the curl operator and applying the following temporal and spatial (2D) Fourier transforms,

$$F(\omega, k_x, k_y, z) = \iiint f(t, x, y, z).e^{i(\omega.t - k_x x - k_y y)} dtdxdy \, ,$$

we get, from the first equation of (3.1),

$$\begin{cases} ik_y E_z - \dfrac{\partial E_y}{\partial z} = i\omega\mu H_x \, , \\[2ex] \dfrac{\partial E_x}{\partial z} - ik_x E_z = i\omega\mu H_x \, , \\[2ex] ik_x E_y - ik_y E_x = i\omega\mu H_z \quad \Rightarrow \quad H_z = -\dfrac{P_y}{\mu} E_x + \dfrac{P_x}{\mu} E_y \, , \end{cases}$$

where $P_x = \frac{k_x}{\omega}$ and $P_y = \frac{k_y}{\omega}$ are the horizontal slowness; and from the second equation of (2.1),

$$\begin{cases} ik_y H_z - \frac{\partial H_x}{\partial z} = -i\omega(i\frac{\sigma}{\omega} + \varepsilon)E_x + J_x\,, \\ \frac{\partial H_x}{\partial z} - ik_x H_z = -i\omega(i\frac{\sigma}{\omega} + \varepsilon)E_y + J_y\,, \\ ik_x H_y - ik_y H_x = -i\omega(i\frac{\sigma}{\omega} + \varepsilon)E_z + J_z \;\; \Rightarrow \;\; E_z = \frac{P_y}{\gamma}H_x - \frac{P_x}{\gamma}H_y - \frac{i}{\omega\gamma}J_z\,. \end{cases}$$

Now, eliminating "E_z" and "H_z" from these equations, defining $\gamma = \varepsilon + i\frac{\sigma}{\omega}$ (complex permittivity) and rearranging the equations we get,

$$\begin{cases} \frac{\partial E_x}{\partial z} = -i\omega\left[(\frac{P_x^{\,2}}{\gamma} - \mu)H_y - \frac{P_x P_y}{\gamma}H_x\right] + \frac{J_z}{\gamma}\,, \\ \frac{\partial E_y}{\partial z} = -i\omega\left[\frac{P_x P_y}{\gamma}H_y + (\mu - \frac{P_y^{\,2}}{\gamma})H_x\right] + \frac{J_z}{\gamma}\,, \\ -\frac{\partial H_y}{\partial z} = -i\omega\left[(\gamma - \frac{P_y^{\,2}}{\mu})E_x + \frac{P_x P_y}{\mu}E_y\right] + J_x\,, \\ \frac{\partial H_x}{\partial z} = -i\omega\left[\frac{P_x P_y}{\mu}E_x + (\gamma - \frac{P_x^{\,2}}{\mu})E_y\right] + J_y\,. \end{cases}$$

This system of equations can be written as,

$$\frac{\partial \underline{b}}{\partial z} = -i\omega \underline{\underline{A}}\,\underline{b} + \underline{S}\,, \tag{3.2}$$

where, $\underline{b} = \left[E_x, E_y, -H_y, H_x\right]^T$ is the wave field, $\underline{S} = \left[\frac{J_z}{\gamma}, \frac{J_z}{\gamma}, J_x, J_y\right]^T$ is the source term, and the system matrix $\underline{\underline{A}}$ is given by,

$$\underline{\underline{A}} = \begin{pmatrix} 0 & 0 & (\mu - \frac{P_x^2}{\gamma}) & -\frac{P_x P_y}{\gamma} \\ 0 & 0 & -\frac{P_x P_y}{\gamma} & (\mu - \frac{P_y^2}{\gamma}) \\ (\gamma - \frac{P_y^2}{\mu}) & \frac{P_x P_y}{\mu} & 0 & 0 \\ \frac{P_x P_y}{\mu} & (\gamma - \frac{P_x^2}{\mu}) & 0 & 0 \end{pmatrix}.$$

By solving the eigenvalue problem, the matrix “$\underline{\underline{A}}$” can be represented in the following form,

$$\underline{\underline{A}} = \underline{\underline{L}}\,\underline{\underline{\Lambda}}\,\underline{\underline{L}}^{-1} \tag{3.3}$$

where the diagonal eigenvalue matrix is given by,

$$\underline{\underline{\Lambda}} = \lambda_0 \cdot \begin{pmatrix} \underline{\underline{I}} & 0 \\ 0 & -\underline{\underline{I}} \end{pmatrix}, \text{ with } \underline{\underline{I}} = \begin{pmatrix} 1 & 0 \\ 0 & 1 \end{pmatrix},$$

and

$\lambda_0 = \sqrt{\mu\gamma - (P_x^{\,2} + P_y^{\,2})}$ is the so-called “vertical slowness”.

The eigenvector matrix $\underline{\underline{L}}$ is given by,

$$\underline{\underline{L}} = \frac{1}{\sqrt{2}} \begin{pmatrix} \underline{\underline{L}}_1 & \underline{\underline{L}}_1 \\ \underline{\underline{L}}_2 & -\underline{\underline{L}}_2 \end{pmatrix},$$

where

$$\underline{\underline{L}}_1 = \lambda_0 . \underline{\underline{I}} ,$$

and

$$\underline{\underline{L}}_2 = \frac{1}{\mu} \begin{pmatrix} \mu\gamma - P_y^2 & P_x P_y \\ P_x P_y & \mu\gamma - P_x^2 \end{pmatrix} .$$

I have not rescaled the eigenvectors to impose the symmetry relation $\underline{\underline{L}}_1^T = \underline{\underline{L}}_2^{-1}$ as suggested by Ursin (1983) because my interest is in the response of a stack of homogeneous layers (such symmetry condition is useful when vertically heterogeneous layers are considered).

Defining the wave vector $\underline{w} = \underline{\underline{L}}^{-1} \underline{b}$, substituting in equation (3.2) and using equation (3.3) we get,

$$\frac{\partial \underline{w}}{\partial z} = \left[-i\omega \underline{\underline{\Lambda}} - \underline{\underline{L}}^{-1} \frac{\partial \underline{\underline{L}}}{\partial z} \right] \underline{w} + \underline{\underline{L}}^{-1} \underline{S} . \quad (3.4)$$

In the absence of sources ($\underline{S} = 0$), we obtain the following homogeneous equation,

$$\frac{\partial \underline{w}}{\partial z} = \left[-i\omega \underline{\underline{\Lambda}} - \underline{\underline{L}}^{-1} \frac{\partial \underline{\underline{L}}}{\partial z} \right] \underline{w} . \quad (3.5)$$

The general solution of this equation, when the operator in parenthesis is continuous, can be written as (e.g., Gilbert and Backus, 1966 and references there in),

$$\underline{w}(z) = \underline{\underline{Q}}(z, z_0)\underline{w}(z_0), \tag{3.6}$$

where the matrix $\underline{\underline{Q}}(z, z_0)$ is called the "wave vector propagator", which is also a solution of the differential equation. In fact, the column vectors of the matrix $\underline{\underline{Q}}(z, z_0)$ are independent wave vector solutions of equation (3.5). Depending on the vertical variation of the properties in the layer, the wave vector propagator can be obtained analytically or by numerical integration.

An important property of the wave vector propagator is intrinsically established in equation (3.6) and can be shown as follows. Let's suppose that we know the wave vector at an initial depth z_0, then, the wave vector at a depth z_1 will be given by,

$$\underline{w}(z_1) = \underline{\underline{Q}}(z_1, z_0)\underline{w}(z_0) \ .$$

Analogously, the wave vector at z_2 can be written as,

$$\underline{w}(z_2) = \underline{\underline{Q}}(z_2, z_1)\underline{w}(z_1) = \underline{\underline{Q}}(z_2, z_0)\underline{w}(z_0) \ ,$$

therefore,

$$\underline{\underline{Q}}(z_2, z_0) = \underline{\underline{Q}}(z_2, z_1)\underline{\underline{Q}}(z_1, z_0) \ ,$$

and, by induction, the last equation can be generalized to,

$$\underline{\underline{Q}}(z_N, z_0) = \prod_{i=0}^{N-1} \underline{\underline{Q}}(z_{i+1}, z_i) \ . \tag{3.7}$$

This equation establishes that the wave vector propagator from z_0 to z_N can be computed by successive multiplication of the intermediate propagators.

3.2.2 Wave vector propagator in a homogeneous layer

In a homogeneous layer, the spatial derivative of the eigenvector matrix becomes zero ($\frac{\partial \underline{\underline{L}}}{\partial z} = 0$), and equation (3.5) reduces to,

$$\frac{\partial \underline{w}}{\partial z} = -i\omega \underline{\underline{\Lambda}} \underline{w} \ , \tag{3.8}$$

and the eigenvalues matrix $\underline{\underline{\Lambda}}$ is constant inside the layer. The solution of this differential equation is,

$$\underline{\underline{Q}}(z, z_0) = e^{-i\omega(z-z_0)\underline{\underline{\Lambda}}} = \begin{pmatrix} e^{-i\omega(z-z_0)\lambda_0} \underline{\underline{I}} & 0 \\ 0 & e^{i\omega(z-z_0)\lambda_0} \underline{\underline{I}} \end{pmatrix} \ , \tag{3.9}$$

where I is the 2x2 identity matrix.

We can see from this equation, that the propagation of the wave vector is composed of two opposite phase shifts operators. Suppose that $z_0 < z$, then the upper diagonal operator corresponds to a phase shift applied to an up-going wave that travels "backward" from z_0 to z, whereas the lower diagonal operator corresponds to a phase shift applied to a down-going wave that travels "forward" from z_0 to z. Figure 3.2 illustrates the physical meaning of this operator. Even though this result has been deduced from this particular case, the meaning of the action of the wave vector propagator has a general validity. In fact, it can be shown (see Appendix A) that the wave vector $\underline{w}$ is a decomposition of the wave field $\underline{b}$ into up-going and down-going waves,

$$\underline{w} = \underline{\underline{L}}^{-1}\underline{b} = [\underline{u}_p, \underline{d}_w]^T \ , \tag{3.10}$$

and therefore, the operator $\underline{\underline{Q}}(z, z_0)$ propagates the up-going and down-going waves from the depth z_0 to z, which is the reason why it is call wave vector "propagator".

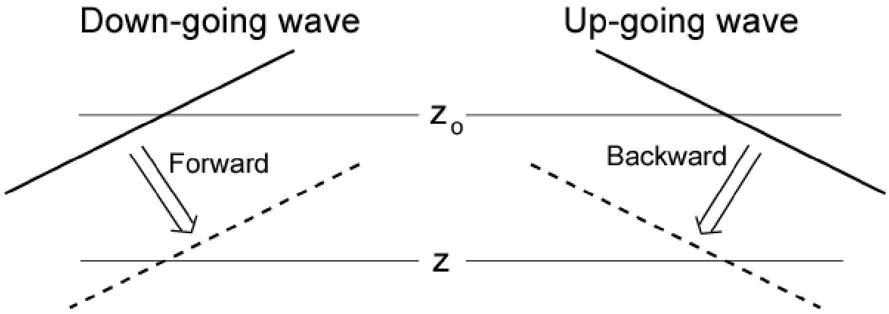

Figure 3.2. Physical meaning of the propagator operator $\underline{\underline{Q}}(z, z_0)$ in a homogeneous media (equation 3.9).

3.2.3 Wave vector propagator at an interface

At an interface (between two different homogeneous layers) the matrix $\underline{\underline{L}}$ is in general discontinuous, and therefore, its vertical spatial derivative does not exist at that particular depth. However, the tangential components of the electric and magnetic fields must be continuous at the interface implying that the wave field $\underline{b}$ must also be continuous. Then, if there is an interface at a depth z, the continuity of the wave field $\underline{b}$ implies that,

$$\underline{\underline{L}}(z^{+})\underline{w}(z^{+}) = \underline{\underline{L}}(z^{-})\underline{w}(z^{-}) \ , \tag{3.11}$$

where z^{+} and z^{-} are the vertical coordinate just below and above the interface, respectively. Comparing this equation with equation (3.6), we can conclude that the wave vector propagator across an interface is given by,

$$\underline{\underline{Q}}(z^{+}, z^{-}) = \underline{\underline{L}}^{-1}(z^{+})\underline{\underline{L}}(z^{-}) . \tag{3.12}$$

3.2.4 Reflection and transmission matrices

The fact that the wave vector $\underline{w}$ is composed of up-going and down-going waves, suggests that the wave vector propagator $\underline{\underline{Q}}(z, z_0)$ could be written as a combination of reflection and transmission matrices that represent the propagation of the up-going and down-going waves through the homogeneous layers and their reflections and transmissions at the interfaces.

Figure 3.3 shows two cases that help us to obtain the general expression of the wave propagator as a function of reflection and transmission matrices. In the regions $z < z_1$ and $z > z_2$ the media are homogeneous, whereas between the depths z_1 and z_2 there is a stack of laterally homogeneous layers (i.e., a vertically heterogeneous medium).

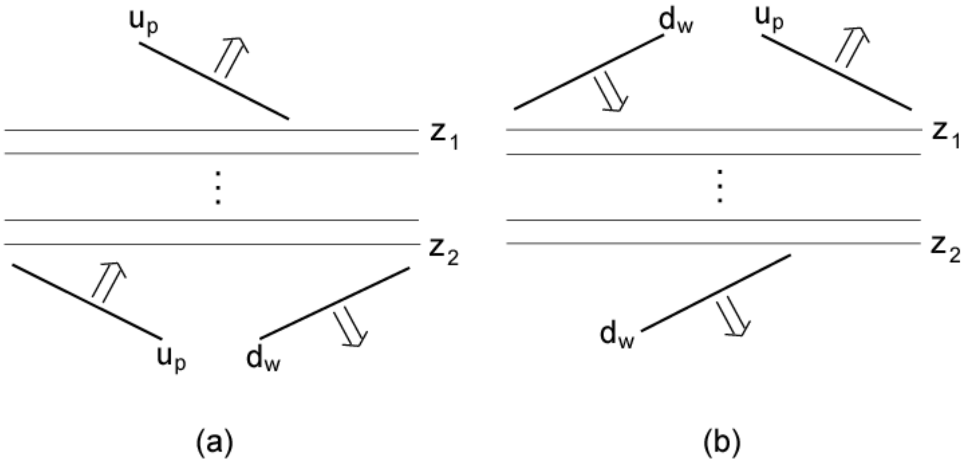

Figure 3.3. (a) Up-going wave impinging from below and (b) down-going wave impinging from above of a vertically heterogeneous region.

Figure 3.3 (a) shows the case when an up-going wave, originated below z_2, impinges the vertically heterogeneous region, generating a reflected down-going waves in the region $z > z_2$ and an up-going wave in the region $z < z_1$. In this case, we can write,

$$\begin{pmatrix} \underline{u}_p \\ \underline{d}_w \end{pmatrix}_{z_2^+} = \begin{pmatrix} \underline{\underline{Q}}_{11} & \underline{\underline{Q}}_{12} \\ \underline{\underline{Q}}_{21} & \underline{\underline{Q}}_{22} \end{pmatrix}_{(z_2^+, z_1^-)} \begin{pmatrix} \underline{u}_p \\ 0 \end{pmatrix}_{z_1^-} , \tag{3.13}$$

where the $\underline{\underline{Q}}_{ij}$'s are 2x2 sub-matrices of $\underline{\underline{Q}}(z_2^+, z_1^-)$, and I have expressed the wave vector $\underline{w}$ as function of up-going and down-going waves. From this equation we have,

$$(\underline{u}_p)_{z_2^+} = \underline{\underline{Q}}_{11(z_2^+, z_1^-)} (\underline{u}_p)_{z_1^-} , \tag{3.14}$$

$$(\underline{d}_w)_{z_2^+} = \underline{\underline{Q}}_{21(z_2^+, z_1^-)} (\underline{u}_p)_{z_1^-} , \tag{3.15}$$

equation (3.14) implies that,

$$(\underline{u}_p)_{z_1^-} = \underline{\underline{Q}}^{-1}_{11\,(z_2^+, z_1^-)} (\underline{u}_p)_{z_2^+} = \underline{\underline{T}}_{U\,(z_2^+, z_1^-)} (\underline{u}_p)_{z_2^+} , \tag{3.16}$$

where

$$\underline{\underline{T}}_{U\,(z_2^+, z_1^-)} = \underline{\underline{Q}}^{-1}_{11\,(z_2^+, z_1^-)} , \tag{3.17}$$

is identified as the transmission matrix for up-going waves. Substituting $(\underline{u}_p)_{z_1^-}$ into equation (3.15) we get,

$$(\underline{d}_w)_{z_2^+} = \underline{\underline{Q}}_{21(z_2^+, z_1^-)} \underline{\underline{Q}}^{-1}_{11\,(z_2^+, z_1^-)} (\underline{u}_p)_{z_2^+} = \underline{\underline{R}}_{U\,(z_2^+, z_1^-)} (\underline{u}_p)_{z_2^+} , \tag{3.18}$$

where,

$$\underline{\underline{R}}_{U\,(z_2^+, z_1^-)} = \underline{\underline{Q}}_{21(z_2^+, z_1^-)} \underline{\underline{Q}}^{-1}_{11\,(z_2^+, z_1^-)} , \tag{3.19}$$

is identified as the reflection matrix for up-going waves.

Figure 3.3 (b) shows the case when a down-going wave, originated above z_1, impinges the vertically heterogeneous region, generating a reflected up-going wave in the region $z < z_1$ and a down-going wave in the region $z > z_2$. In this case, we can write,

$$\begin{pmatrix} 0 \\ \underline{d}_w \end{pmatrix}_{z_2^+} = \begin{pmatrix} \underline{\underline{Q}}_{11} & \underline{\underline{Q}}_{12} \\ \underline{\underline{Q}}_{21} & \underline{\underline{Q}}_{22} \end{pmatrix}_{(z_2^+, z_1^-)} \begin{pmatrix} \underline{u}_p \\ \underline{d}_w \end{pmatrix}_{z_1^-} . \tag{3.20}$$

Proceeding analogously to the previous case, we obtain the following equations,

$$(\underline{u}_p)_{z_1^-} = -\underline{\underline{Q}}^{-1}_{11\,(z_2^+, z_1^-)} \underline{\underline{Q}}_{12(z_2^+, z_1^-)} (\underline{d}_w)_{z_1^-} = \underline{\underline{R}}_{D(z_2^+, z_1^-)} (\underline{d}_w)_{z_1^-} , \tag{3.21}$$

and

$$(\underline{d}_w)_{z_2^+} = [\underline{\underline{Q}}_{22(z_2^+, z_1^-)} - \underline{\underline{Q}}_{21(z_2^+, z_1^-)} \underline{\underline{Q}}^{-1}_{11\,(z_2^+, z_1^-)} \underline{\underline{Q}}_{12(z_2^+, z_1^-)}] (\underline{d}_w)_{z_1^-} = \underline{\underline{T}}_{D(z_2^+, z_1^-)} (\underline{d}_w)_{z_1^-} , \tag{3.22}$$

where

$$\underline{\underline{R}}_{D(z_2^+, z_1^-)} = -\underline{\underline{Q}}^{-1}_{11\,(z_2^+, z_1^-)} \underline{\underline{Q}}_{12(z_2^+, z_1^-)} , \tag{3.23}$$

and

$$\underline{\underline{T}}_{D(z_2^+, z_1^-)} = \underline{\underline{Q}}_{22(z_2^+, z_1^-)} - \underline{\underline{Q}}_{21(z_2^+, z_1^-)} \underline{\underline{Q}}^{-1}_{11\,(z_2^+, z_1^-)} \underline{\underline{Q}}_{12(z_2^+, z_1^-)} , \tag{3.24}$$

are identified as the reflection and transmission matrices for down-going waves, respectively.

Finally, the equations (3.17), (3.19), (3.23) and (3.24) can be inverted to obtain the matrices $\underline{\underline{Q}}_{ij}$ as a function of the reflection and transmission matrices for up-going and down-going waves. In this way, it is easy to show that,

$$\underline{\underline{Q}}_{(z_2^+,z_1^-)} = \begin{bmatrix} \underline{\underline{T}}_U^{-1} & -\underline{\underline{T}}_U^{-1}\underline{\underline{R}}_D \\ \underline{\underline{R}}_U\underline{\underline{T}}_U^{-1} & \underline{\underline{T}}_D - \underline{\underline{R}}_U\underline{\underline{T}}_U^{-1}\underline{\underline{R}}_D \end{bmatrix}_{(z_2^+,z_1^-)} . \tag{3.25}$$

3.3 RECURSION EQUATIONS

Based on the fundamental property of the wave vector propagator (equation 3.7) and its representation as a function of transmission and reflection matrices (equation 3.25), recursive relations can be obtained to compute the resulting transmission and reflection matrices for a system composed of layered sub-systems. Figure 3.4 shows a graphical interpretation of the recursive equations. We are interested to obtain algebraic relations between the reflection and transmission matrices from z_1 to z_3 based on the reflection and transmission matrices from z_1 to z_2, and z_2 to z_3. From equation (3.7) we can write,

$$\underline{\underline{Q}}(z_3,z_1) = \underline{\underline{Q}}(z_3,z_2)\underline{\underline{Q}}(z_2,z_1) \quad , \tag{3.26}$$

then, substituting the wave vector propagators by their representations as a function of transmission and reflection matrices (equation 3.25) and equating the sub-matrices elements we obtain,

$$\begin{aligned}
\underline{\underline{T}}_{U_{31}} &= \underline{\underline{T}}_{U_{21}} (\underline{\underline{I}} - \underline{\underline{R}}_{D_{32}} \underline{\underline{R}}_{U_{21}})^{-1} \underline{\underline{T}}_{U_{32}} \quad , \\
\underline{\underline{R}}_{U_{31}} &= \underline{\underline{R}}_{U_{32}} + \underline{\underline{T}}_{D_{32}} \underline{\underline{R}}_{U_{21}} (\underline{\underline{I}} - \underline{\underline{R}}_{D_{32}} \underline{\underline{R}}_{U_{21}})^{-1} \underline{\underline{T}}_{U_{32}} \quad , \\
\underline{\underline{R}}_{D_{31}} &= \underline{\underline{R}}_{D_{21}} + \underline{\underline{T}}_{U_{21}} (\underline{\underline{I}} - \underline{\underline{R}}_{D_{32}} \underline{\underline{R}}_{U_{21}})^{-1} \underline{\underline{R}}_{D_{32}} \underline{\underline{T}}_{D_{21}} \quad , \\
\underline{\underline{T}}_{D_{31}} &= \underline{\underline{T}}_{D_{32}} \underline{\underline{T}}_{D_{21}} + \underline{\underline{T}}_{D_{32}} \underline{\underline{R}}_{U_{21}} (\underline{\underline{I}} - \underline{\underline{R}}_{D_{32}} \underline{\underline{R}}_{U_{21}})^{-1} \underline{\underline{R}}_{D_{32}} \underline{\underline{T}}_{D_{21}} \, .
\end{aligned} \tag{3.27}$$

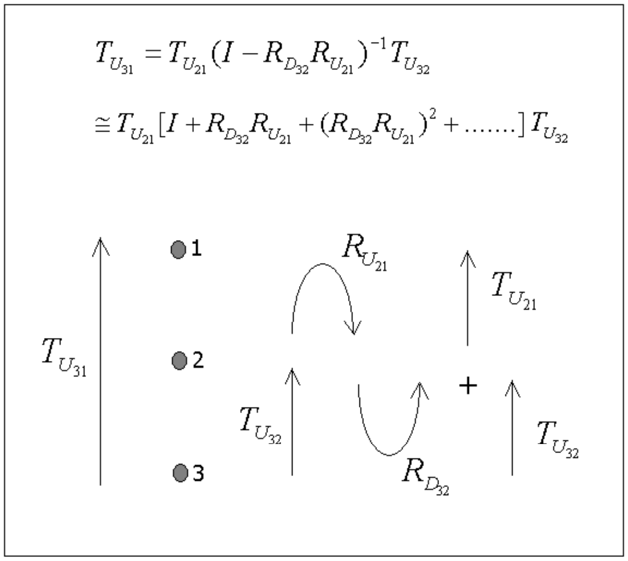

Figure 3.4. Schematic representation of one of the recursive relations. Only the first order reverberation is shown.

The operator $(\underline{\underline{I}} - \underline{\underline{R}}_{D_{32}} \underline{\underline{R}}_{U_{21}})^{-1}$, which appear in all these equations, introduces all the reverberations that occur between z_1 and z_3. To see this, the operator can be expanded in an infinite series as,

$$(\underline{\underline{I}} - \underline{\underline{R}}_{D_{32}} \underline{\underline{R}}_{U_{21}})^{-1} = \mathrm{I} + \underline{\underline{R}}_{D_{32}} \underline{\underline{R}}_{U_{21}} + \left(\underline{\underline{R}}_{D_{32}} \underline{\underline{R}}_{U_{21}}\right)^{2} + \left(\underline{\underline{R}}_{D_{32}} \underline{\underline{R}}_{U_{21}}\right)^{3} + \ldots\ldots \ .$$

The convergence of this series requires that the spectral radii $\rho\left(\underline{\underline{R}}_{D_{32}} \underline{\underline{R}}_{U_{21}}\right) < 1$ (e.g., Varga, 1962). This condition is always satisfied because the only case when the spectral radii of a reflection matrix become equal to one is when the contrast of impedances is infinite, which is not possible physically. However, the reflectivity at the interface of a given layer can be very close to one. If the difference (to one) were less than the numerical precision used, an artificial divergence would be generated. The presence of a layer (in our model) that produces such artificial divergence is of no practical interest because no waves would be transmitted at such an interface, and therefore, no reflections would be observed from underneath it. However, to avoid the accidental occurrence of such cases, the determinant of $\left(\underline{\underline{I}} - \underline{\underline{R}}_{D_{32}} \underline{\underline{R}}_{U_{21}}\right)$ is computed and checked to be different from zero.

3.4 SYNTHESIS OF RADARGRAMS

3.4.1 Plane-wave domain and offset-time domain

Common midpoint (CMP) and wide angle reflection and refraction (WARR) gathers give us information about the reflectivity of the system at different angles of incidence (e.g., Zeng, et. al., 2000) and are the equivalent of CMP and wide angle reflection gathers in seismic reflection techniques (David and Annan, 1989). In a WARR gather, the source is located at a fixed position and the receivers are placed (along a line) at varying distances (offsets) from the source. On the other hand, in a CMP gathers the source and receiver are separated (also along a line) symmetrically from a fixed point (called midpoint). These two types of gathers are, in general, different in laterally heterogeneous media. However, in laterally homogeneous media, these two types of gathers are identical and I will refer them as CMP gathers.

The reflectivity technique gives us the transmission and reflection matrices for each value of frequency and horizontal slowness, and therefore, these matrices represent the physical responses of the system to harmonic plane waves each one characterized by a given frequency and angle of incidence (horizontal slowness). The plane wave domain is not the same as the domain in which the data is normally acquired (CMP gather). However, a plane wave decomposition of the data can be made via a Radon or tau-p transform (e.g., Stoffa, et. al., 1981; Chapman, 1981). In this case, the data is transformed to the intercept time – slowness domain (also call "tau-p" (τ - p) domain) and a consecutive Fourier transform (from the intercept time to the frequency domain) will give us the harmonic plane wave representation of the data (i.e., in the same domain that we obtain the response of a laterally homogeneous system using the reflectivity technique).

When generating synthetic CMP data using the reflectivity technique, we must transform the data from the plane wave domain to the offset-time domain. This process implies two different transforms: one from the frequency to the time domain, and other from the slowness to the space domain. If the frequency to time transform is made first, the modeling technique is called "slowness reflectivity method" (because the intermediate domain is in the slowness space), whereas if the slowness to space transform is made first, the technique is called "spectral reflectivity method" (e.g., Chapman, 1978). The slowness reflectivity method is essentially the inverse process of plane wave decomposition aforementioned. This method is more intuitive and the intermediate results are tau-p seismograms (or radargrams) that can be directly interpreted and, if necessary, compared with the real data that has already been transformed to the tau-p domain. Additionally, the technique is operationally easier to implement since it involves an inverse Fourier transform followed by an inverse tau-p transform (if we want to obtain the final data in the offset-time domain).

3.4.2 The source term and the generation of radargrams

In a GPR survey, the antennas are placed in the air and very close to the surface. Therefore, there is not reflection condition from above the antennas (as usually happen with the free surface reflections in seismic techniques). Then, following the source response formalism of the reflectivity technique (Kennett, 1983), the relation between the source term (the source is placed at depth z_s) and the wave vector at the receiver depth z_r (with $z_s < z_r$), can be written as (see Appendix B),

$$\underline{b}(z_r) = \underline{\underline{L}}(z_r)\begin{pmatrix} \underline{\underline{T}}_{U_{rs}}^{-1}\underline{\underline{R}}_{D_s}\underline{\xi}_d \\ \underline{\underline{T}}_{D_{rs}}\underline{\xi}_d \end{pmatrix} , \tag{3.28}$$

where $\underline{\underline{R}}_{D_s}$ is the down-going waves reflection matrix for the whole system (seen from the source position), $\underline{\underline{T}}_{U_{rs}}$ and $\underline{\underline{T}}_{D_{rs}}$ are the up-going and down-going transmission matrices from the source to the receiver positions, respectively, and $\underline{\xi}_d$ is the down-going wave component of the source term, i.e.,

$$\underline{\underline{L}}^{-1}(z_s)\underline{S} = \begin{pmatrix} \underline{\xi}_u \\ \underline{\xi}_d \end{pmatrix} . \tag{3.29}$$

It is interesting to remember that all these quantities depend on the slowness components (p_x and p_y) and frequency. For a given spatial distribution of the current density, we will obtain a particular source term "$\underline{S}$". The application of the operator $\underline{\underline{L}}^{-1}$ will give us a representation (up-going and down-going waves) of this source term, which contains the radiation pattern of the source.

In equation (3.28) we recognize an up-going wave $\underline{\underline{T}}_{U_{rs}}^{-1}\underline{\underline{R}}_{D_s}\underline{\xi}_d$ and a down-going wave $\underline{\underline{T}}_{D_{rs}}\underline{\xi}_d$. The transmission matrices compensate for the difference in depth between the source and receiver positions. We can see that the up-going wave is the reflection of the source down-going wave by the stack of layer, whereas the down-going wave is the continuation of the down-going wave coming from the source (the direct wave). The eigenvector matrix $\underline{\underline{L}}(z_r)$ operate on the up-going and down-going waves to recombine them and give us the final wave field $\underline{b}$ whose components are the electric and magnetic fields at the receiver position. Physically we see that the reflectivity technique is giving us the response expected theoretically (i.e., the response at the receiver should be the superposition of the reflected and the direct waves).

3.5 RESULTS FROM THE REFLECTIVITY TECHNIQUE

3.5.1 Reflection at an interface: comparison of the reflectivity technique with Fresnel's equations

In this section, I present a comparison between the reflection and transmission coefficients at an interface obtained from the classic Fresnel's equations with those from the propagator matrix technique.

Even though it can be shown that both the results are identical analytically (see Appendix A), in Figures 3.5 and 3.6, I show a comparison of the numerical results obtained with Fresnel's equations and those obtained with the propagator matrix algorithm. The left side of Figure 3.5 shows the reflection coefficients for the "x" and "y" components of the electric field (of a down-going plane wave) when the lower medium is non-conductive, whereas on the right side, the lower medium is conductive (the parameters of the media are also shown in the figure).

Figure 3.6 shows the transmission coefficient for the same components and cases as Figure 3.5. These figures show that the results obtained with the reflectivity matrices technique and Fresnel's equations are in excellent agreement, as expected.

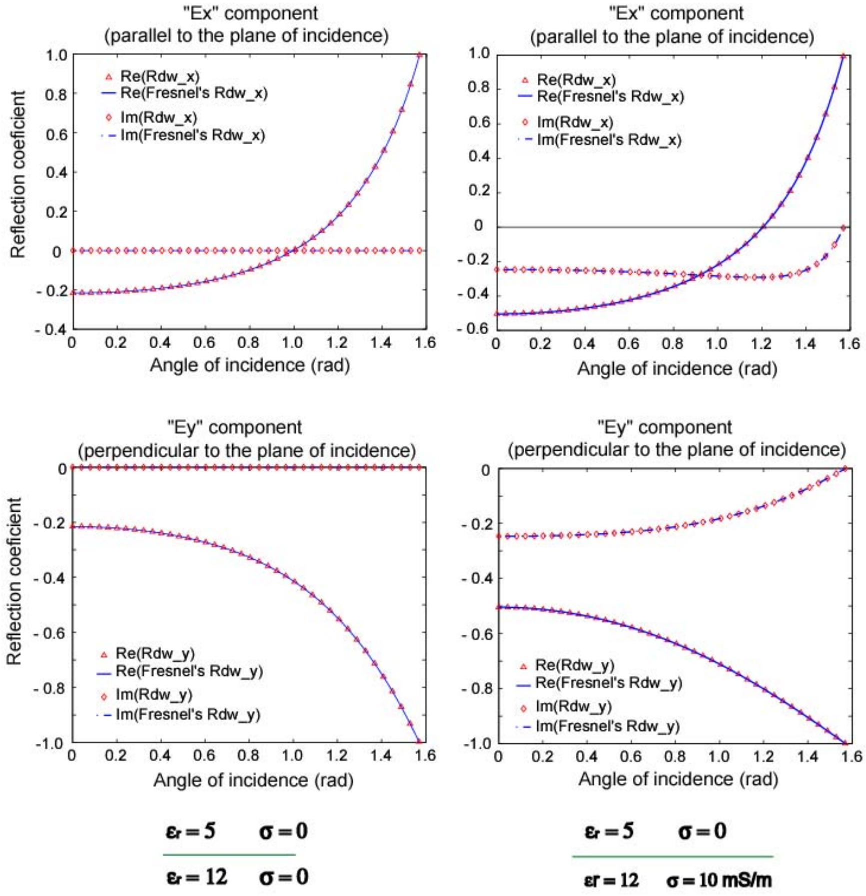

Figure 3.5. Comparison between the down-going reflection coefficients computed with Fresnel's equations and the reflectivity technique: on the left and on the right are the results corresponding to a non-conductive and conductive lower media, respectively. The coefficients have been computed at a frequency of 100 MHz, and $\mu_r = 1$.

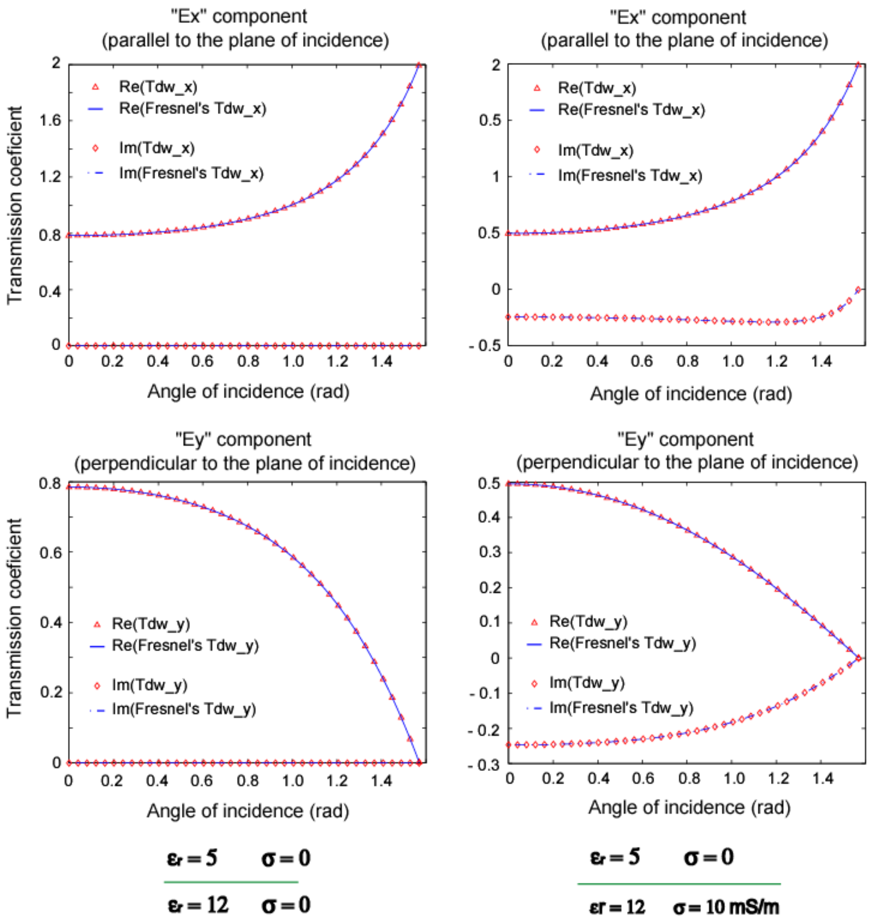

Figure 3.6. Comparison between the down-going transmission coefficients computed the Fresnel's equations and the reflectivity technique. On the left and on the right are the results corresponding to a non-conductive and conductive lower media, respectively. The coefficients have been computed at a frequency of 100 MHz, and $\mu_r = 1$.

Notice that, in the case of the lower conductive media, the reflection and transmission coefficients have, in general, a non-null imaginary part. This imaginary part, which is frequency dependent, introduces an additional phase shift during reflection and transmission of the waves. Therefore, we expect that the shape and phase of the wavelet will be affected by this additional factor, being an important aspect that differentiates the reflections produced by a contrast in electric conductivity from that produced by a contrast in electric permittivity.

3.5.2 Comparison of the results obtained with the Reflectivity and FDTD techniques

3.5.2.1 Multiple layers

In this section I present a comparison between the results generated with the FDTD algorithm and the propagator matrix technique for a system of laterally homogeneous layers. For simplicity, the 2D FDTD algorithm has been used (see chapter 2). Figure 3.7 shows the models (layered media) employed and the relative orientation of the electric and magnetic fields, as well as the relative orientation of slowness vector. The intention of using these two models is that, due to the duality of the electric and magnetic fields, by interchanging the magnetic and electric properties we can obtain some interesting cases (such as the Brewster's angle) using the 2D FDTD technique and make a better comparison of the results. The source is an infinite line with a current function equal to a squared hanning window, i.e., $j(t) = \left(0.5 - 0.5\cos(2\pi t / T)\right)^2$.

Figures 3.8 shows the tau-p radargrams (E_y component) obtained with the propagator matrix technique. They were generated using the equation (3.32) without including the direct wave term, i.e., convolving the current function only with the total downward reflection matrix of the system. Notice the Brewster's angles that appear in the radargram that correspond to model II. These radargrams show the qualitative and quantitative behavior expected theoretically. For example, the Brewster's angle observed in model II corresponds to the angle where the reflection coefficient of the "y" component of the magnetic field becomes zero. We also observe that for model I, the amplitude of the first reflection increases with offset, this is equivalent to the case shown on the right side of figure 3.5.

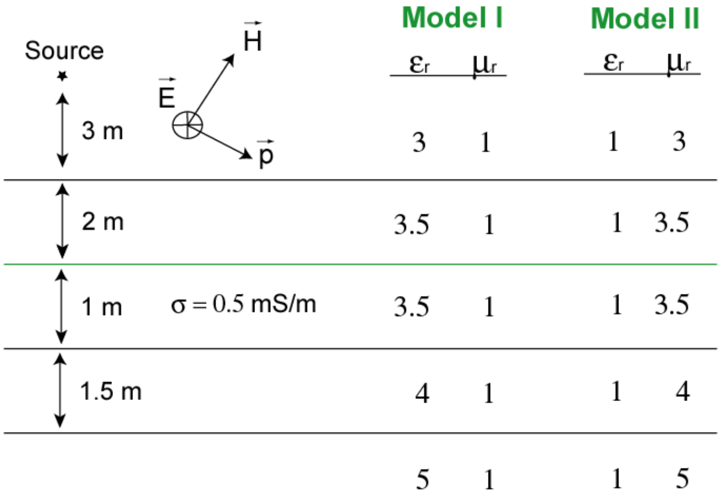

Figure 3.7. Models used to compare the results obtained with the reflectivity and FDTD techniques.

Finally, an important observation is the different wavelet character of the reflection produced at the interface between the non-conducting and the conducting layers. Notice that this wavelet is different from those reflected at the interfaces where only a contrast in electric permittivity is present. This indicates that the phase introduced by the complex part of the reflection coefficient effectively changes the form of the wavelet during reflection.

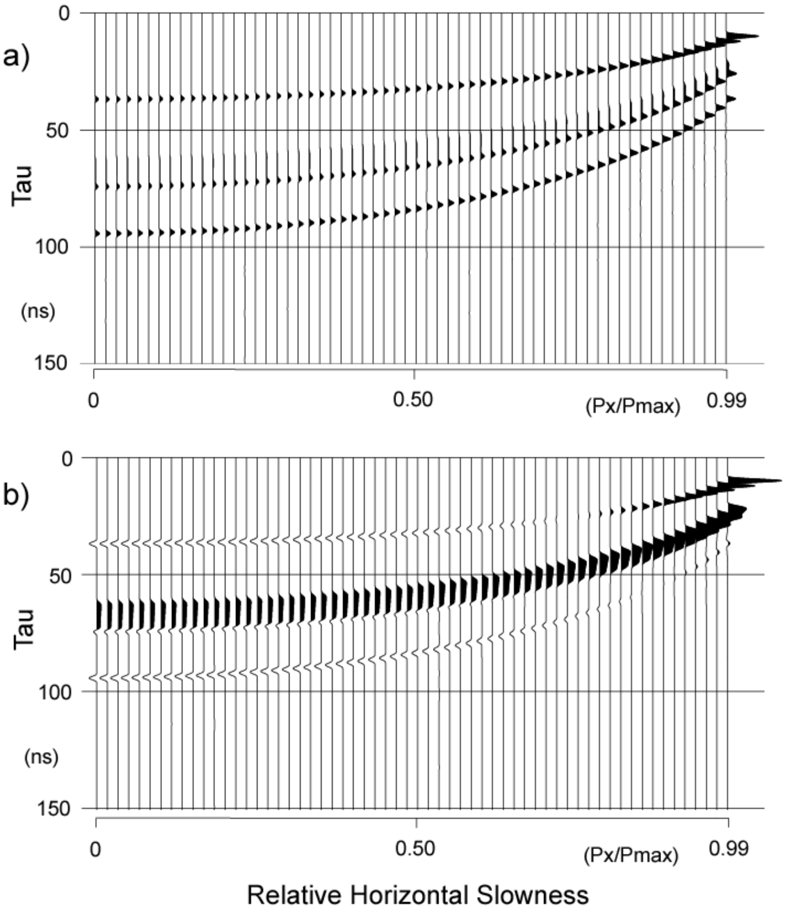

Figure 3.8. Tau-p radargrams (E_y component) generated with the reflectivity technique; (a) and (b) are the responses of model I and II, respectively.

In order to compare these results with those from the FDTD, I transform the tau-p radargrams to the offset-time domain. Figures 3.9 and 3.10 show the results obtained for models I and II, respectively.

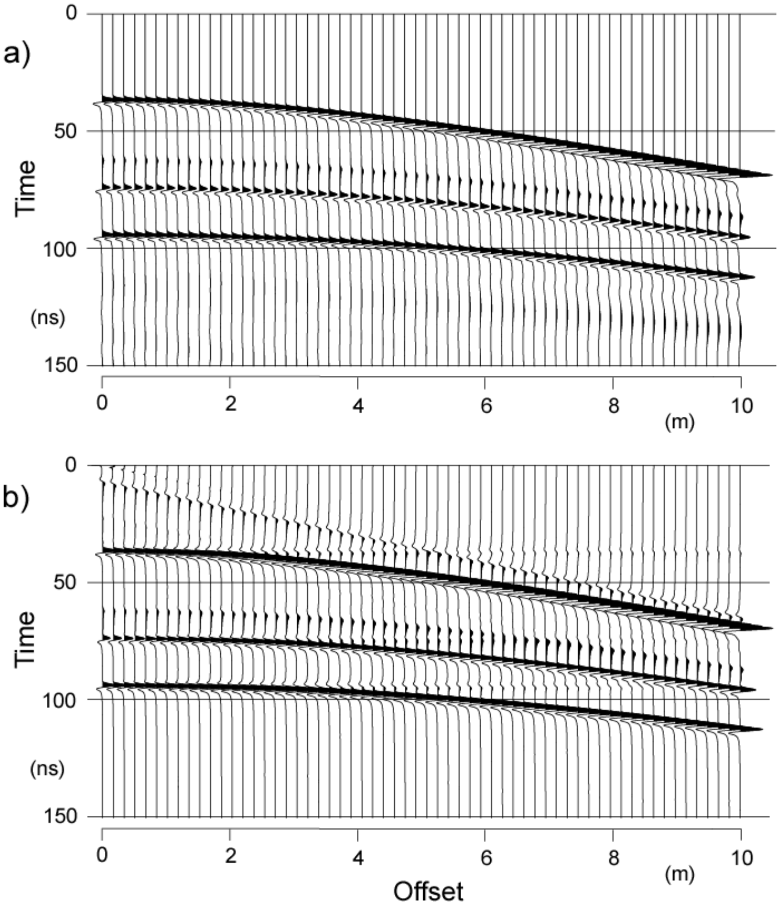

Figure 3.9. Comparison, in the x-t domain, between the radargrams obtained with (a) FDTD and (b) reflectivity technique for model I shown in Figure 3.7.

The agreement between these results is excellent except for the artifacts introduced by the inverse tau-p transform. A tapering at the borders of the tau-p data can reduce these artifacts, but also affects the amplitude of the reflection in the radargram, especially at the far offset. This effect can be seen in Figure 3.11 where the tau-p radargrams were tapered before transformation to the offset-time domain.

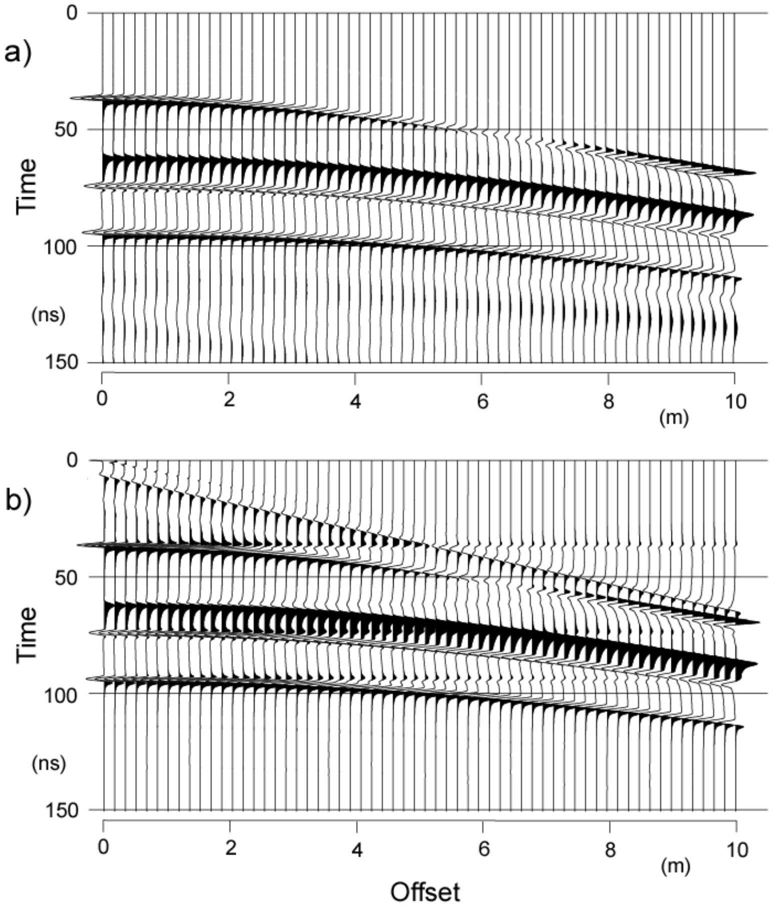

Figure 3.10. Comparison, in the x-t domain, between the radargrams obtained with (a) FDTD and (b) reflectivity technique for model II shown in Figure 3.7.

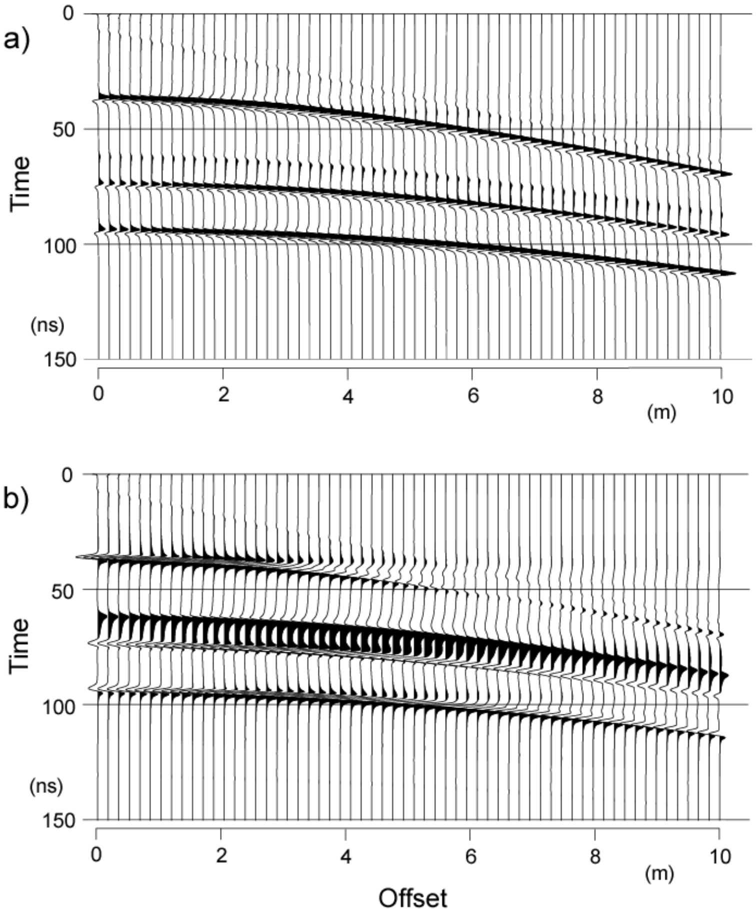

Figure 3.11. Radargrams obtained with the reflectivity technique. The tau-p data (Figure 3.8) were tapered at the lateral borders before transformation to the x-t domain.

3.5.2.2 Air-soil interface

In the last section, I presented an example for multiple layers where the source was placed at a considerable distance (greater than the wavelength) from the reflectors. In that case, I only included the reflection response and not the direct wave since, under such conditions, the interference between the direct wave and the reflected waves is not important for the offsets considered. However, in real CMP GPR data, the antenna is placed very close to the soil (a distance smaller than the wavelength), and therefore, the interaction between the direct wave and the reflected wave at the air-soil interface, is important for all practical offsets. This interaction produces a partial cancellation of the waves in the air, increasing the amount of energy that effectively penetrates into the soil, and also generates a modification of the radiation pattern in the subsurface that is important for the GPR technique. Engheta (1982) and Smith (1984) analytically computed the resulting radiation pattern using a plane wave (far-field) approximation. Since the reflectivity technique is also based on a plane wave representation of the wave field, we expect that the results obtained with the reflectivity technique should be comparable to those of Engheta and Smith. The main objective of this section is to compare these results.

Figure 3.12 shows the model used for this comparison. A line source is placed very close to the air-soil interface (2 cm above) and the characteristics of the current pulse are the same as those in the previous section. It is evident that with this small separation between the source and the air-soil interface, small offsets imply wide angles of incidence on this interface; therefore, the slowness used to generate the tau-p section must reach the maximum slowness in the air. Furthermore, it must include even higher values of slowness that are possible in the soil and are associated to the waves propagating in the ground (in this way, the direct ground wave is included in the generation of the synthetic data).

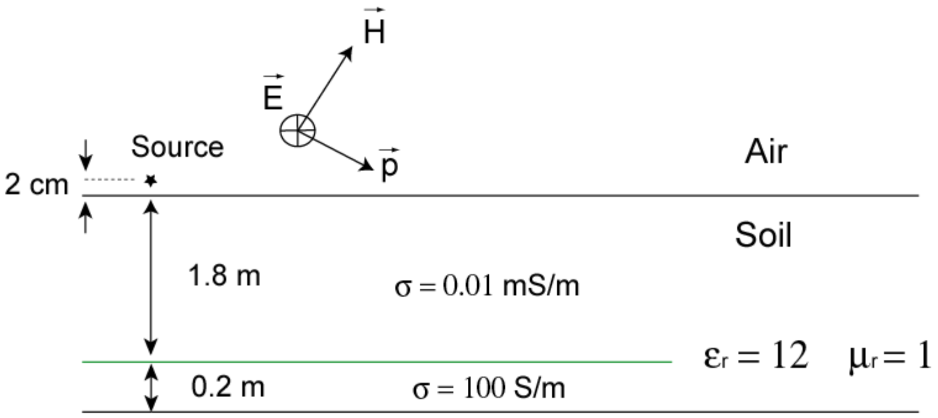

Figure 3.12. Model used to compare the reflectivity and FDTD responses for a line source placed very close to the air-soil interface. The bottom layer of the model has a very high conductivity so that the reflection coefficient at the interface with the soil layer (green line) is practically equal to –1 for all angles of incidence.

Figure 3.13 shows the tau-p radargram obtained with the reflectivity technique. Notice how after passing the maximum slowness in the air several orders of reverberation are observed in the tau-p radargram, and the character of the wavelet has changed. The maximum magnitude of the signal is also reached at this value of slowness ($P_{\max}$ in the air). This behavior is expected theoretically (see Appendix B). Notice that the soil layer (limited by the air on the top and a high conductivity layer at the bottom) acts as a wave guide and most of the energy that penetrates into the soil reverberates inside this layer. This energy partially leaks out from the layer or is dissipated by resistivity losses.

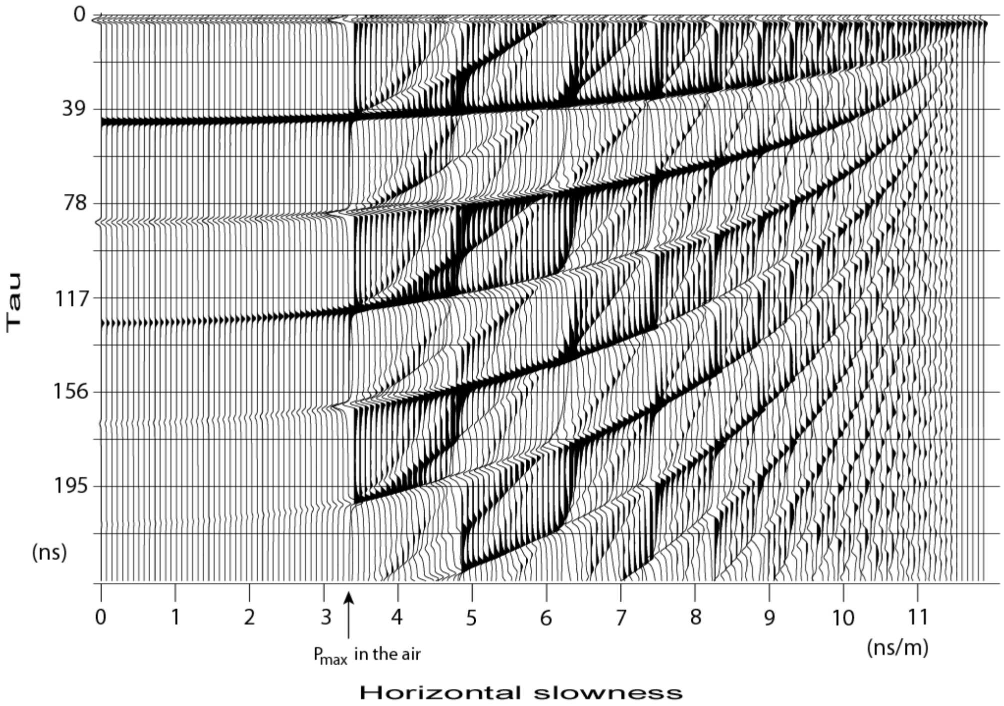

Figure 3.13. Tau-p response generated with the reflectivity technique for the model shown in Figure 3.12. Notice that the horizontal slowness used in the modeling goes beyond the maximum slowness in the air and that, for those higher values of slowness (corresponding to an evanescent wave in the air but propagating waves in the ground), a complex pattern of multiples is observed. The maximum slowness in the soil corresponds to about 11.5 ns/m.

Figure 3.14 (a) shows the offset-time domain radargram obtained with the FDTD technique, and Figure 3.14 (b) shows the offset-time domain radargram obtained by inverse transform of the tau-p radargram obtained with reflectivity technique. “A” and “B” are the so called direct air and ground wave, respectively.

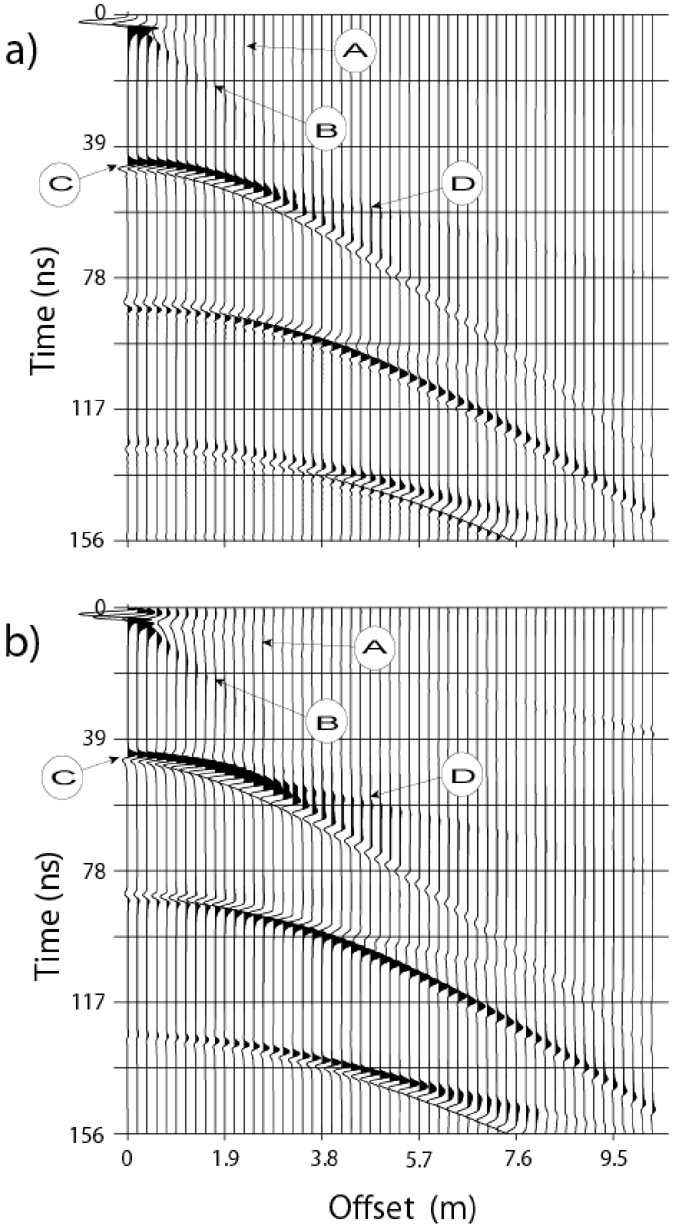

Figure 3.14. (a) FDTD and (b) reflectivity offset-time responses computed for the model shown in Figure 3.12. See main text for the explanation of the events (A, B, C and D) indicated in the figure.

Indicated as “C” is the first reflection coming from the interface between the soil layer and the high conductivity layer below it (see Figure 3.12), and “D” is the refracted air wave associated with this reflection. The following reflections are multiples (reverberations). Notice how, in both the plots, there is a maximum of amplitude for the reflection “C” just at the offset position where the refracted wave “D” merges with the reflection. This offset corresponds to the so called critical angle. This maximum is more accentuated in the reflectivity than in the FDTD data. Since the conductivity of the bottom layer is very high, the reflection coefficient at its interface with the soil layer is practically constant for all the angles of incidence. Therefore, the amplitude of the reflection is essentially proportional to the amplitude of the incident wave. Even though the received reflected wave is affected by the transmission coefficient when going from the soil to the air, we see that the amplitude of the reflection is still maximum at the critical angle. Comparing qualitatively these results with those presented by Lampe (see Figure 2.5, Chapter 2), we see that the results obtained with the reflectivity technique are in good agreement with those of the analytical solution given by Engheta (1982) and Smith (1984), indicating that the reflectivity technique also represents a far field approximation.

3.5.3 Comparison between real and reflectivity GPR data

One of the most important applications of modeling techniques is to help with the interpretation of real data. In this regard, the reflectivity technique can help us to make a quantitative interpretation of the GPR data. In general, CMP gathers are commonly used for velocity analysis. However, this type of data can also give us information about the electromagnetic impedance of the layers whose contrast produces the observed reflections. The reflectivity technique can help us estimate these impedances by matching the characters of the reflections observed in the real GPR data with those obtained by this modeling technique. For a more accurate estimation of these parameters an inversion technique have to be implemented. In this case, the reflectivity method can be used as a very efficient forward modeling technique, as has been shown in inversion of seismic data (e.g., Sen and Stoffa (1991), and Stoffa and Sen (1991)).

In this section, I make a quantitative interpretation of a real GPR-CMP gather by matching these data with the synthetic gathers generated using the reflectivity technique.

An initial model is estimated by a stack velocity analysis. Because the velocity of the radar signal mostly depends on the electric permittivity of the media, only the initial thicknesses and permittivities are estimated by this analysis. Then, I change the model until the best observable match between the real and the synthetic data is obtained. In changing the model, the attenuation and character of the reflection wavelets in the data help us to direct the changes of the model.

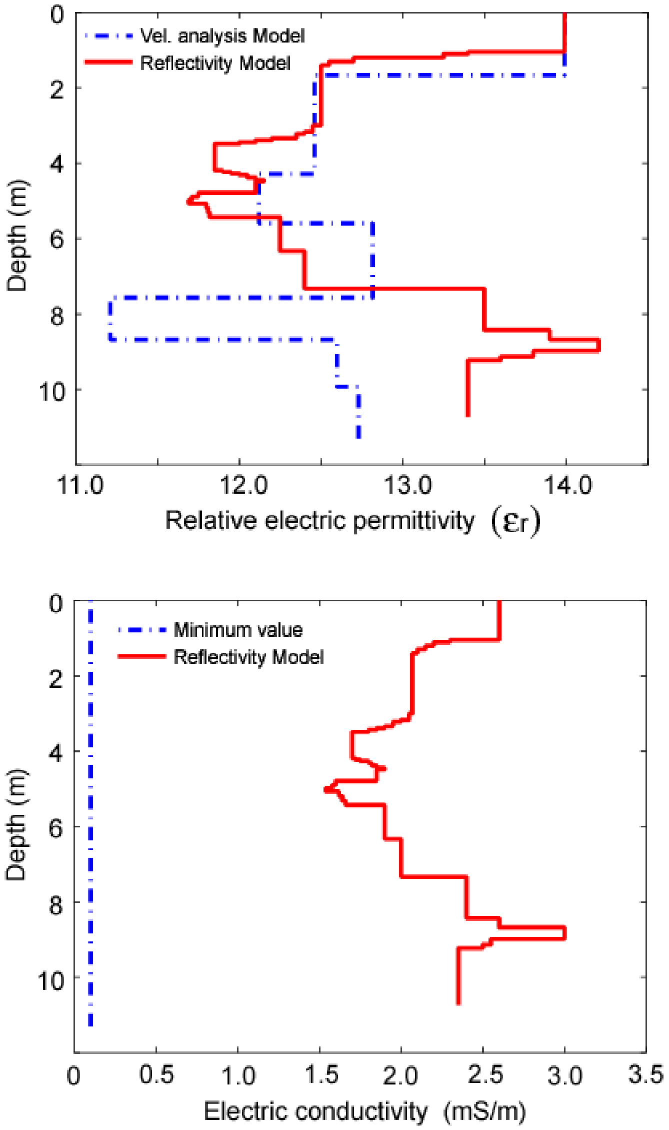

Figure 3.15. (a) Relative electric permittivity models obtained by velocity analysis and matching the real data with the synthetic reflectivity data. (b) Electric conductivity model obtained by matching the real data with the synthetic reflectivity data. See main text for the explanation of the curve indicated as “minimum value”.

Figure 3.15 (a) and (b) show the initial model obtained with the velocity analysis and the final model obtained by matching the reflectivity synthetic data with the real data. Figure 3.15 (a) shows the relative electric permittivity as a function of depth. As we can see, both the models are similar except at the deepest part, where the velocity analysis gives a reduction of the electric permittivity. However, the synthetic data obtained with the velocity analysis model (see figures 3.16 and 3.17), do not match correctly the reflection characteristics of the real data. Additionally, the error of the velocity analysis technique could generate uncertainties, in the estimated permittivity values, of the same order of magnitude than the differences obtained between the two models. These observations allow us to conclude that the reflectivity modeling can give us a more accurate inversion of the data by matching not only the kinematics of the data (hyperbolic events), but also their dynamic characteristics (amplitude and phase of the reflections).

Figure 3.15 (b) shows the conductivity models. Because the velocity analysis does not strongly depend on the conductivity of the model, we have supposed a minimum value of conductivity to generate the corresponding synthetic data (curve indicated as “minimum value”). On the other hand, the conductivity obtained from the matching the real data with the reflectivity technique shows some correlation with the electric permittivity model. However, the sensitivity of the model response to the conductivity is smaller than to the permittivity parameter, therefore, the uncertainty for this parameter is expected to be greater than for the permittivity and could be of the order of magnitude of the oscillations or changes of the conductivity observed in the model. Nevertheless, the order of magnitude of the conductivity values must be correct since they explain the attenuation of the radar signal and improve the match between the real and synthetic data for some particular reflections (as for example, the very shallow and deepest ones).

Figure 3.16 (a) shows the real CMP data used in this section (this CMP corresponds to the acquired at the location X=14m, in the line shown in figure 4.17, chapter 4). A gain proportional to the square root of time has been applied to partially compensate for divergence (i.e., the natural spherical divergence is approximately reduced to cylindrical, and therefore, we can compare the real data with the synthetic 2D tau-p inverse transformed reflectivity data). Figure 3.16 (b) show the synthetic data generated with the initial model obtained by velocity analysis (see Figure 3.15); Figure 3.16 (c) show the synthetic data generated with the final model obtained by matching the real and synthetic data; and Figure 3.16 (d) show the synthetic data generated for the same permittivity model than Figure 3.16 (c) but with a lower conductivity (“minimum value” shown in Figure 3.15(b)). The use of a minimum conductivity is to avoid the effects of tuning in the model, which will require an excessive slowness sampling to avoid noisy artifacts.

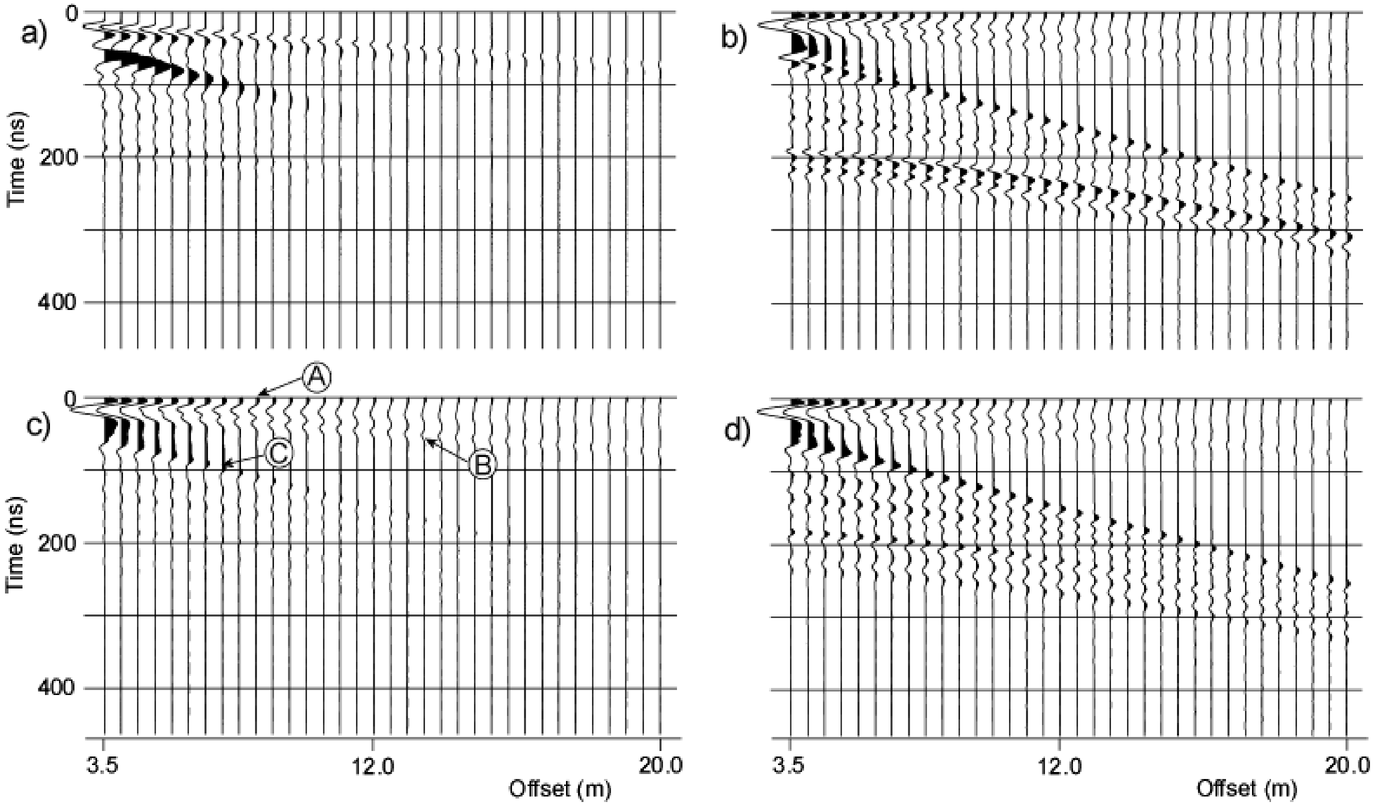

Figure 3.16. (a) Real CMP GPR data. (b) Synthetic data generated with the model obtained from the velocity analysis and using a uniform and small value of conductivity ("minimum value" indicated in Figure 3.15). (c) Synthetic data generated with the final model for which a good match with the real data was obtained. (d) Same as (c) but using the "minimum value" of conductivity indicated in Figure 3.15. See main text for an explanation of the events pointed as A, B and C.

Notice that the amplitude of the direct air and ground waves are greater than the subsurface reflections in both the real and the synthetic data. In the synthetic data (Figures 3.16 (b), (c) and (d)) the event pointed out as “A” (see Figure 3.16 (c)) is an artifact generated by the inverse tau-p transform and is associated with the high amplitude of the source at zero offset. This artifact affects the character of the direct wave (pointed out as “B”) at small offsets, but for far offset we can see that the direct wave of the synthetic data is comparable to the observed in the real data. Comparing the figures 3.16 (a) and (c), we see that the direct ground wave (pointed out as “C”) agrees in the shape, velocity and decay of amplitude with offset. However, at very small offset the wavelet does not agree very well. This discrepancy may indicate that the soil has a gradient in the shallow part that has not been included in the model or the presence of other factors such as, the roughness of the soil surface, vegetation (grass) and lateral heterogeneities of the soil which are not considered in the modeling technique. The last but more important characteristic to be considered is the matching of the subsurface reflections. To be able to compare these reflections, I muted the air and ground waves (as well as the artifact indicated as “A”) and plotted the results in Figure 3.17. Comparing these plots we can see that the final model generates the synthetic response that is closest to the real CMP data. The reflections shown in Figure 3.17 (b) do not have the same character as the real data and the amplitude of the reflections increases appreciably with the offset. In Figure 3.17 (d) the character of the reflections do not change appreciably at small offset respect to those in Figure 3.17 (a) and (c). However, for increasing offsets

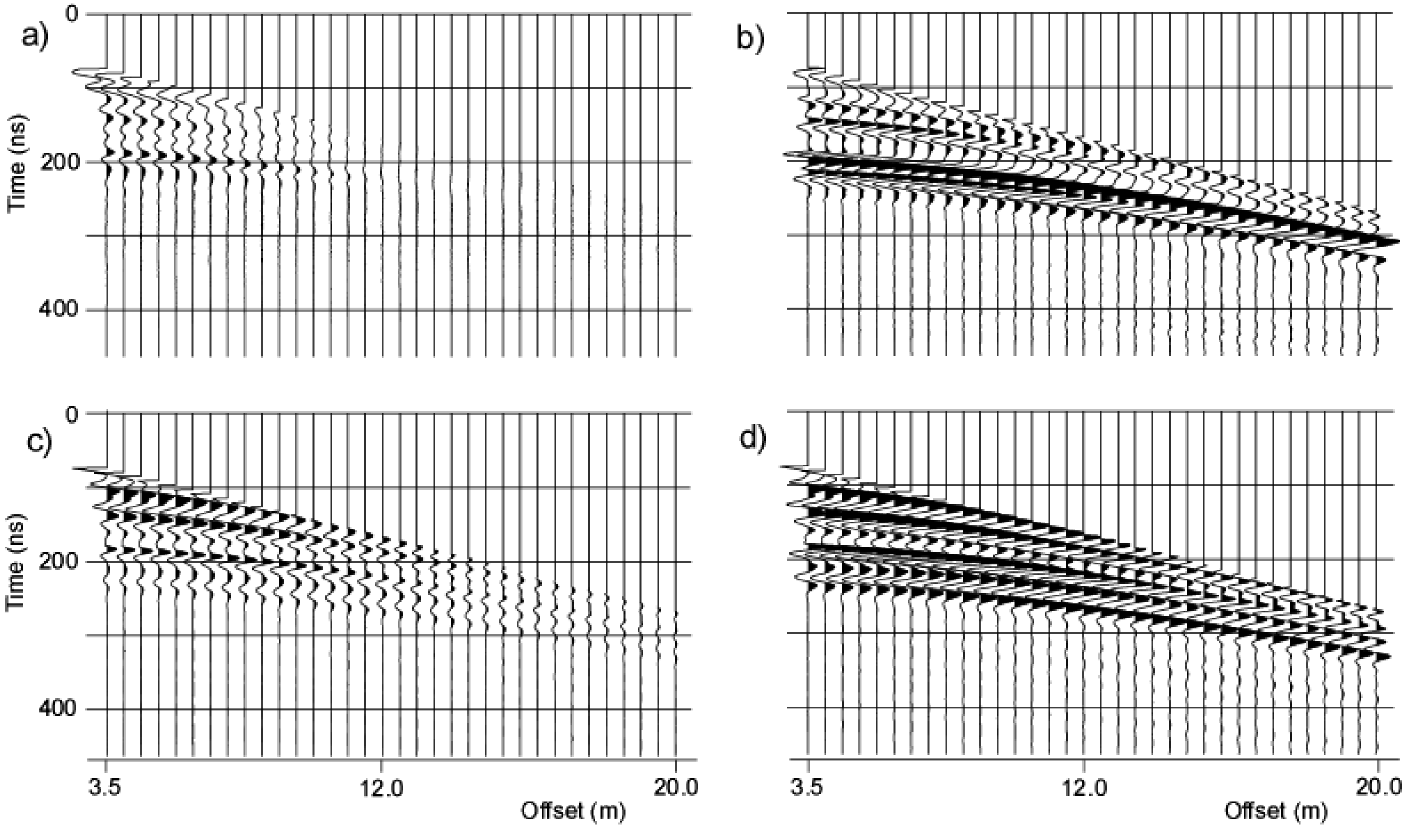

Figure 3.17. Same as Figure 3.16 but the events “A”, “B” and “C” have been muted. See main text for details.

the character (waveform), of the reflections, changes and the amplitude also increases. Therefore, we see that the conductivity parameter in the model is very important to obtain a closer modeling response to the real data.

Finally, another aspect that can be observed in Figure 3.17 (c) compared to (a), is the slightly higher amplitude of the reflections in the synthetic data for intermediate offsets. This difference with the real data can be due to the following factors: First, the fact that the reflectivity technique accentuates the radiation pattern at intermediate offsets (corresponding to the critical angle) as has been shown in the synthetic example of the air-soil interface (previous section), and second, the surface roughness, vegetation and soil lateral heterogeneities of the real system can produce a differential penetration of the energy in the subsurface, altering the intensity of the reflection with offset. Nevertheless, the good agreement between the real and synthetic data demonstrates the capabilities of the reflectivity technique to reproduce real CMP GPR data and is encouraging for future applications on inversion techniques.

3.6 SUMMARY

Modeling of GPR data in laterally homogeneous media is very important because horizontally layered media are often encountered in shallow exploration geophysics, or such a model can represent the simplest approximation to the subsurface, which allows an initial interpretation of the data (as is the case when

CMP velocity analysis is carried out, which assumes a horizontally layered media). In laterally homogeneous media Fourier transforms in the horizontal coordinates reduce the electromagnetic equations to a system of ordinary first order differential equations in the vertical direction. I have considered the case of isotropic laterally homogeneous media and developed the slowness reflectivity technique, initially proposed by Kennett to model elastic waves. This technique is unconditionally stable and has the following additional advantages: it is numerically efficient (for example, it requires hundreds of times less resources, and computational time, than finite difference modeling techniques), it includes all the orders of reverberation (multiples) in the media and the technique allow us also to limit the order of reverberation if desired, the dynamic and kinematics responses of the media are generated simultaneously and, since the wavelet character of the source is introduced at the end of the computation by convolution with the data generated by the reflectivity matrices (in the plane wave domain), it is possible to change the response for different wavelet or sources signatures without having to compute again the reflectivity matrices. All these characteristics make this modeling technique an excellent tool for model-based inversion of GPR data.

I have compared the results obtained with the developed reflectivity and FDTD techniques, and the agreement is excellent in the far field and reasonably good for the near field, indicating that the reflectivity technique, which is based on a plane wave representation of the wave field, is a far field approximation and generates equivalent results to the approximate analytical solutions for the radiation pattern of antennas in a air-soil interface as presented by Engheta (1982) and Smith (1984). I have also compared the results between real data and synthetic data obtained with the reflectivity technique. In this case, I changed the model manually still obtaining a good match between the real and the synthetic data. These results show that the reflectivity technique reproduces the main characteristics of the real data (direct air wave and ground wave, and the deeper reflections), and therefore, an improvement of the match is possible using inversion techniques. For intermediate offsets (corresponding to the so called critical angle) the reflectivity technique produces a slightly higher amplitude for the reflections. As has been pointed out in the air-soil example comparing the FDTD and reflectivity results, this may be due to the fact that the plane wave representation of the wave field is a far field approximation or also to effects not considered in the modeling technique such as surface roughness, vegetation, and lateral heterogeneities in the soil. However, if necessary, a correction for these effects could be introduced in the modeling technique to compensate for these effects. Finally, I have shown that the conductivity of the subsurface is an important factor that affects the intensity of the GPR data and the character of the reflections (i.e., the wavelet form and phase). Therefore, it must be taken into account in modeling and inversion of GPR data.

Chapter 4: Migration of GPR data

Migration of Ground Penetrating Radar data has traditionally been implemented assuming homogeneous, non-conductive and non-dispersive media. However, in many real applications, the effects of heterogeneities, conduction and/or dispersion can be important and it is necessary to take into account these effects to image the data correctly. I implement the split step Fourier technique for migration of GPR data in 2D media (TE or TM propagation modes) and present the formalism for its extension to 3D heterogeneous media. I demonstrate how this technique takes into account, in a natural and efficient way, the effects of dispersion and attenuation, as well as the heterogeneities of the media. Using synthetic and real data, to evaluate the new technique, I have obtained very good results for low to medium lossy media, improving the resulting images and restoring the correct reflection amplitudes.

4.1 INTRODUCTION

The similarity between GPR and seismic reflection has led to the application of processing techniques used in seismic data processing to process GPR data (e.g., Davis and Annan, 1989; and Grasmueck and Horstmeyer, 1994). However, these migration techniques do not take into account the dispersion and attenuation effects that are commonly produced on electromagnetic waves in shallow subsurface applications and, in many cases, the heterogeneities of the media are not considered even though the influence of these effects on migration of GPR data can be important.

Dispersion and attenuation effects define the applicable bandwidth of the GPR technique. For example, dispersion effects related to the conductivity of the media are important for frequencies below a few MHz (in typical soil conductivities); at these low frequencies a mixed regime of diffusion and propagation is present, making the traditional interpretation of radargrams very difficult. Conversely, the strong attenuation at high frequencies (above ~1 GHz), due to conduction or dielectric absorption, defines a high frequency limit for the GPR technique in geological applications. As a consequence of these effects, there is a compromise between penetration and resolution, and the usual depth of penetration of the GPR technique ranges between a few centimeters to tens or hundreds of meters, depending on the main frequency employed and the characteristics of the medium.

The conductive and dispersive characteristics of soils and rocks have been extensively studied in the literature (e.g., Hoekstra and Delaney, 1974; Scott et. al., 1963; and Sherman, 1988). Most soils and rocks are conductive, and therefore, attenuation of the GPR signal is almost ubiquitous of this technique. The magnitude of the conductivity can vary widely and depend on diverse factors such as water and clay content, porosity, concentration of electrolytes, temperature, etc. Most of these factors may also induce dispersion of the electric permittivity of the soil and rocks, making the phase velocity dependent on frequency and causing dielectric absorption. The dispersion of the electromagnetic waves is important because it produces a broadening of the radar pulse that degrades the resolution of the resulting GPR image.

In the split step Fourier technique (Stoffa, et al., 1990), a heterogeneous medium is decomposed into a vertical stack of horizontal layers. In each layer, the slowness is represented by an average value and a perturbation term that depends only on the lateral coordinates. Under this model, a phase shift is computed based on the average slowness and applied in the frequency-wave number domain to extrapolate the wave field through each depth interval “dz” corresponding to the thickness of a layer. Subsequently, a phase shift correction is applied in the frequency-space domain to take into account (first order approximation) the effects of the lateral variation of the slowness during the extrapolation of the wave field through the layer. In the present work, I implement this technique for migration of GPR data and demonstrate the benefits of introducing, in a natural and efficient way, the effects of dispersion and attenuation in the media. These effects are represented by a complex slowness whose imaginary part appears as a consequence of absorption in the media (conductive, dielectric or magnetic losses). Even in the case that the electromagnetic properties of the media do not depend on frequency, the presence of conductivity in the media makes the imaginary part of the complex electric permittivity dependent on frequency, changing the phase velocity (dispersion) and attenuating the waves. Therefore, by introducing a complex slowness in the wave field extrapolation, each plane wave is propagated and amplified depending on its frequency and wave number component. The approximation of homogeneous plane waves is introduced to enhance the stability of the migration algorithm, allowing migration through thicknesses equivalent to two or three times the characteristic skin depth of the media computed at the dominant frequency of the GPR signal. Of course, introducing the attenuation and dispersion effects into the migration algorithm is only useful for media where the conductivity or losses are small enough to allow the propagation of energy through them and back to the surface (i.e., media with absorption zones whose thicknesses are comparable to their characteristic skin depths computed at the dominant frequency of the radar signal), and therefore, the range of stability obtained with the developed migration algorithm is approximately equal to the physical depth of observation that can be expected.

To show the improvement obtained by using the split step Fourier technique for imaging GPR data in dispersive and conductive media, examples of real and synthetic data are presented. I use an explicit Finite Difference Time Domain (FDTD) algorithm (presented in chapter 2) to generate the synthetic data in dispersive and heterogeneous media. Even though the examples shown in this work are migration of zero (or common) offset sections, the extension for 2D pre-stack migration can follow the simpler seismic analog of Tanis (1998). In the 3D case, the split step Fourier technique will lead to a coupling between the different components of the electric field. This coupling is induced by the gradient of the electromagnetic properties in the media and the split step Fourier technique will lead to a coupled extrapolation operator.

4.2 SPLIT STEP FOURIER MIGRATION OF GPR DATA

4.2.1 Electromagnetic vector wave equations

Maxwell's equations in isotropic media can be expressed (SI units) as,

$$\nabla x \underline{E} = -\mu \frac{\partial \underline{H}}{\partial t} \quad , \qquad (4.1)$$
$$\nabla x \underline{H} = \sigma \underline{E} + \varepsilon \frac{\partial \underline{E}}{\partial t} + \underline{J}_s \quad ,$$

where $\underline{E}$ is the electric field, $\underline{H}$ is the induction magnetic field, μ is the magnetic permeability, ε is the electric permittivity, σ is the electric conductivity and $\underline{J}_s$ is the current density (source).

Applying a Fourier transform from time to frequency domain, we obtain,

$$\nabla x \underline{E} = -i\omega\mu \underline{H} \quad , \qquad (4.2)$$
$$\nabla x \underline{H} = \sigma \underline{E} + i\omega\varepsilon \underline{E} + \underline{J}_s \quad .$$

In these equations, we can now suppose that μ, ε and σ depend on the angular frequency ω to account for dispersion in the media (e.g., Jackson, 1975).

In the absence of sources ($\underline{J}_s = 0$), applying the curl operator to both equations in (4.2) and using them to eliminate the curl of the fields on the right sides of the resulting equations, we obtain the following electromagnetic vector wave equations,

$$\nabla\times\nabla\times\underline{E} = \mu(\omega^2\varepsilon - i\omega\sigma)\underline{E} - i\omega\nabla\mu\times\underline{H} \ , \qquad (4.3)$$

$$\nabla\times\nabla\times\underline{H} = \mu(\omega^2\varepsilon - i\omega\sigma)\underline{H} + (i\omega\nabla\varepsilon + \nabla\sigma)\times\underline{E} \ , \qquad (4.4)$$

Note that the gradient of the electromagnetic properties introduce a coupling between the two fields and modify the relative values of their components during propagation, changing the direction, intensity and phase of the fields, and the double curl operator on the left side of these equations introduces a self-coupling among the three components of each field separately, also due to heterogeneities in the media.

If we consider a 2D medium and the plane of incidence perpendicular to the strike direction of the medium, the propagation problem can be decomposed into the so called transverse electric (TE) and transverse magnetic (TM) modes (e.g., Jackson, 1975); furthermore, if the lateral heterogeneities of the media are very small, the horizontal gradient of the properties can be neglected without changing appreciably the physical description of the system because the main component of each mode will only change its amplitude and phase but will not change its direction. In contrast, for the general 3D case, the gradients of the properties must be retained to allow the interaction between the components of the fields, and so, the electric and magnetic fields can change their directions when the direction of propagation changes.

In the next section, I will develop the migration technique in 2D laterally weak heterogeneous media. Then, in the section that follows, I will establish the basis for Split step Fourier migration of GPR data in 3D laterally weak heterogeneous media.

4.2.2 Migration in 2D heterogeneous media

In practice, GPR data are acquired in lines that are generally perpendicular to the strike of the geological structures or the main axis (greater length) of specific targets (as for example, pipes, cavities or buried structures). Additionally, the perpendicular broadside mode (see Figure 1.1) is commonly used to maximize the response of the targets that are below the survey line. Under these conditions, we can see that the transversal electric (TE) mode is the best representation of the propagation of the radar signal, and therefore, I used this mode to develop the migration technique in 2D media.

Neglecting the terms containing the gradients of the properties in equation (4.3) and choosing the “y” axis in the direction perpendicular to the plane of incidence that contains the survey line, the propagation problem is reduced to the following scalar (stationary wave) equation,

$$\nabla^2 E + \omega^2 u^2 E = 0 \ , \tag{4.5}$$

where E is the transverse component of the electric field (in our reference system, it is the “y” component of the electric field), and the complex slowness “u” is given by,

$$u = \sqrt{\mu \gamma^*} \ ,$$

and $\gamma^* = \varepsilon - i\,\sigma/\omega$ is the conjugate of the complex permittivity (see the definition of the complex permittivity in Chapter 2). The sign of the Fourier transform applied to equation 4.1 is opposite to that used in Chapter 2, but it is in accordance with the sign convention used by Stoffa et. al. (1990) on the development of the split step Fourier technique. I have made this choice because, in addition to being consistent with the sign convention of Stoffa et. al. (1990), the complex slowness defined in this way will automatically compensate for the attenuation of the GPR signal produced by absorption or conductive losses in the media.

Now, following the development of the split step Fourier technique (Stoffa, et. al., 1990), we divide the medium into horizontal layers of small thickness “dz” such that we consider only lateral variation of the electrical and magnetic properties inside each layer (see Figure 4.1); then, we can write,

$$\mu(z,x) = \overline{\mu} + \Delta\mu(x)\,,$$

$$\varepsilon(z,x) = \overline{\varepsilon} + \Delta\varepsilon(x)\,,\ \text{and} \qquad (4.6)$$

$$\sigma(z,x) = \overline{\sigma} + \Delta\sigma(x)\,,$$

where $\overline{\mu}$, $\overline{\varepsilon}$ and $\overline{\sigma}$ are the mean values of the properties in each layer, and $\Delta\mu(x)$, $\Delta\varepsilon(x)$ and $\Delta\sigma(x)$ are their lateral variations. Note that we have chosen the "x" direction as the lateral coordinate, the "z" direction (pointing downward) as the vertical coordinate and, as commented before, the transversal electric field is oriented in the "y" direction.

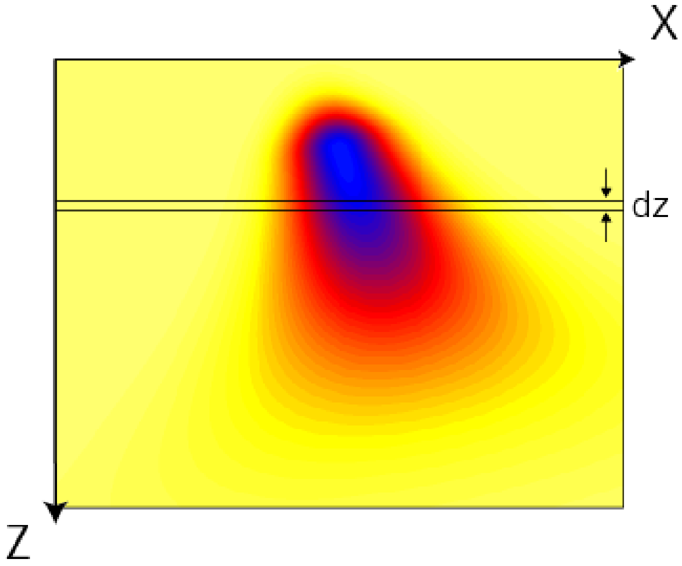

Figure 4.1. Model representation of the subsurface in the Split step Fourier technique. The subsurface is considered as a stack of layers, each one thin enough to suppose that the electromagnetic properties inside each layer only vary in the lateral direction.

Now, substituting the equations (4.6) in the wave equation (4.5), we get:

$$\nabla^2 E + \omega^2 u_0^2 E = -\omega^2 \left[\Delta\mu(\bar{\varepsilon} - i\bar{\sigma}/\omega) + \bar{\mu}(\Delta\varepsilon - i\Delta\sigma/\omega)\right]E \quad , \quad (4.7)$$

where we can identify

$$\Delta\mu(\bar{\varepsilon} - i\bar{\sigma}/\omega) + \bar{\mu}(\Delta\varepsilon - i\Delta\sigma/\omega) \equiv 2u_0\Delta u \quad , \qquad (4.8)$$

with the mean slowness "u_0" given by

$$u_0 = \sqrt{\bar{\mu}(\bar{\varepsilon} - i\bar{\sigma}/\omega)} = \sqrt{\bar{\mu}\bar{\gamma}^*} \quad . \qquad (4.9)$$

It is interesting to note that, in this case, there is no quadratic term (Δu^2) in the source term of equation (4.9) and so, the split step approximation is more accurate when it is directly expressed in terms of the electromagnetic properties than the slowness itself.

With these definitions of Δu and u_0, given by equations (4.8) and (4.9) respectively, and taking into account the approximation of homogeneous waves (see next section), the application of the split step technique follows naturally. Figure 4.2 shows a schematic diagram of the split step Fourier algorithm. Initially the electric field at the surface $E(x, z = 0, t)$ is transformed into the frequency-wave number domain to downward extrapolate the field through each "dz" interval. For each "dz", Δu and u_0 are defined for all the frequencies used and all the positions in the layer. This part of the computation is an important feature of the algorithm because it allows us to introduce, in a natural and efficient manner, the dispersion and attenuation effects as represented by the complex slowness. When these effects are important, the additional but small computational cost can improve the results significantly.

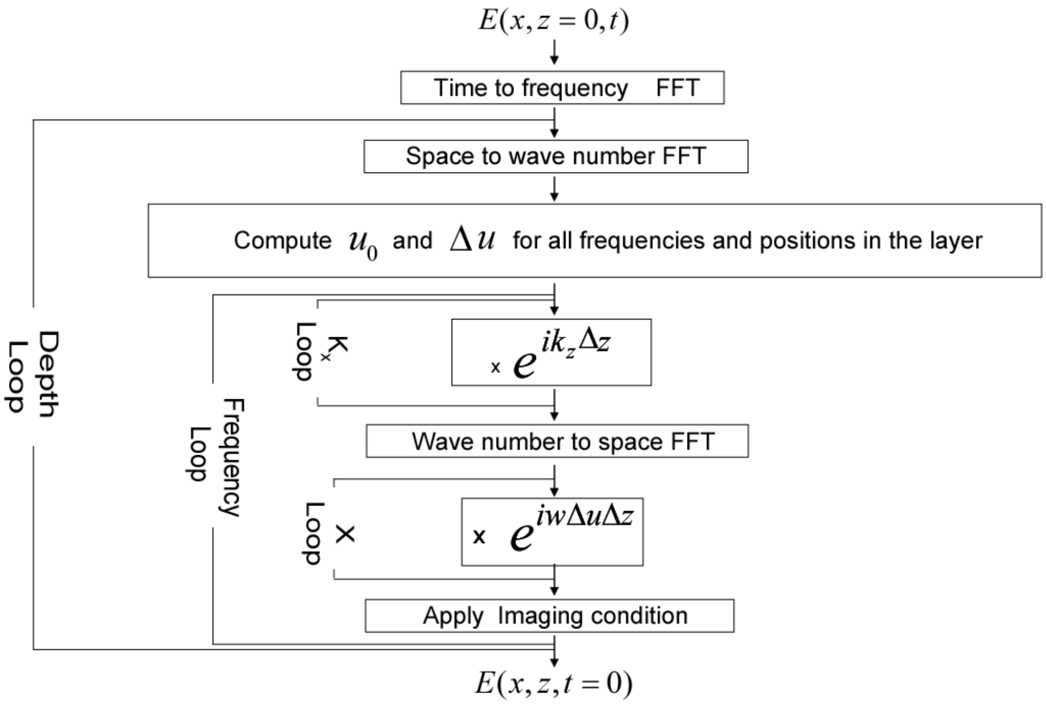

Figure 4.2. Flowchart of the Split step Fourier technique in lossy, dispersive and heterogeneous 2D media.

4.2.2.1 Homogeneous, inhomogeneous and evanescent waves

In lossy media, attenuation is represented by the imaginary part of the slowness, and the dispersion effects are generated by the dependence of the slowness on frequency. Taking into account these effects during migration implies that we must compute the slowness for each frequency and apply a gain to the wave field during its extrapolation. In the split step Fourier technique, these effects are applied through operators that include the vertical slowness and the slowness perturbations.

In general, soils are lossy media for electromagnetic waves. If we suppose that they are laterally homogeneous then any plane wave impinging from the air will generate a transmitted heterogeneous wave with its plane of constant amplitude parallel to the soil surface and its plane of constant phase forming an angle with the soil surface that depends on the angle of incidence of the impinging plane wave and the properties of the soil; only for normal incidence will the transmitted wave be homogeneous (e.g., Chen, 1983). If we implement the migration algorithm under this supposition, good results can be obtained till depths approximately equal to the corresponding skin depth of the conductive zones (Sena, et. al., 2003). However, if we want to migrate the data to depths greater than the corresponding skin depth, the algorithm becomes unstable (especially when the medium is laterally heterogeneous). We have observed that this instability is produced by the invalidity of the assumption of laterally homogeneous media and the erroneous amplification of near horizontally propagating waves.

If the medium is conductive and laterally heterogeneous, the approximation of plane waves can still be used but a more general and plausible approximation about the direction between the constant amplitude and constant phase planes of each plane wave must be made. Since the interfaces between the different zones in a laterally heterogeneous medium are not horizontal or uniform, a reasonable approximation would be to suppose that the propagating waves are homogeneous (i.e., that their planes of constant amplitude are parallel to their planes of constant phase). Under this approximation, the vertical slowness will be given by (see Appendix C),

$$q_z = \frac{k_z}{\omega} = u_0 \sqrt{1 - k_x^2 / a^2} \quad , \tag{4.10}$$

where $a = \omega \mathrm{Re}(u_0)$.

Notice that ω / a is effectively the phase velocity in the medium. If $\mathrm{Re}(u_0) >> \mathrm{Im}(u_0)$ the value of a could be approximated by $a \cong \omega |u_0|$ or neglecting the imaginary part of u_0^2 by $a \cong \omega (\mathrm{Re}(u_0^2))^{1/2}$.

Physically, the approximation of homogeneous waves implies that the amplification of the waves, during extrapolation, is along their direction of propagation and depends on the path length traversed by each wave when they are extrapolated through each layer. This approximation is physically more reasonable and introduces stability to the migration algorithm, avoiding the excessive amplification of near horizontally propagating waves and making it possible to extrapolate the wave field through depths greater than the corresponding skin depth of the conductive zones.

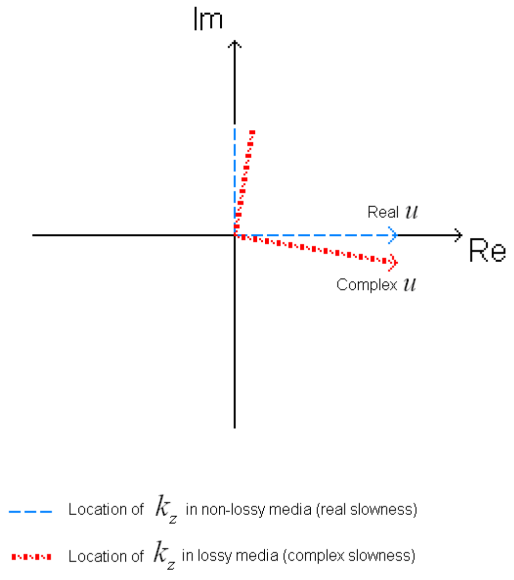

Figure 4.3. Locations of the vertical slowness k_z in lossy and non-lossy media. The values of k_z located in the line parallel to the slowness direction correspond to homogeneous waves whereas those located in the line perpendicular to the slowness direction correspond to the so called evanescent waves.

An important consideration when computing the vertical slowness is the presence of evanescent waves. They correspond to angles of incidence greater than the critical angle, for which the quantity inside the square root in equation (4.10) becomes negative (this is analogous to the case obtained for real slowness media). Figure 4.3 shows a diagram of the location paths of k_z in the complex plane for lossy and non-lossy media. For $k_x = 0$ (vertical incidence) $k_z = \omega u_0$. When the value of k_x increases, the square root of equation (4.10) approaches zero and the value of k_z approaches the origin moving in a line parallel to u_0. Note that for these values of k_z (with a negative imaginary part), the extrapolation operator will amplify these waves (propagating waves). On the other hand, when the square root becomes complex, the values of k_z follow a new path whose direction is perpendicular to the direction of u_0 (rotated 90° counter clock wise). In this new path, the imaginary part of k_z is positive, and therefore, the extrapolation operator will attenuate these (evanescent) waves.

4.2.2.2 Limited gain modifications for high lossy media

For highly lossy media, the gain introduced by the imaginary part of the complex slowness can lead to enormous values of total gain and make the migration algorithm unstable. This instability is inherently related to the approximate nature of the technique and the attempt to amplify the wave field beyond the real limit of physical detection. I explore the possibility of limiting this gain by two different modifications to the algorithm.

In the first modification, a limit to the natural gain is applied in both, the frequency-wave number and the frequency-space domain. Accumulated gain matrices (in each domain) are stored, updated and used to compute the effective gains to be applied to each frequency-wave number and frequency-space component in order to keep the cumulative gain limited to a specified maximum value. In the second modification, no gain is allowed in the frequency-wave number domain and a limited gain is applied only in the frequency-space domain; therefore, in this modification, the gain is applied only in the vertical direction and its magnitude is defined by the whole imaginary part of the slowness. In this way, the following g_{eff} operators substitute the pure exponential operators of the split step technique,

$$g_{eff} = \left[\left(g_{cc} + g_{\max} - 1\right) / \left(g_{cc} . g_{abs} + g_{\max} - 1\right)\right] \exp\left(i\phi\right) , \qquad (4.11)$$

where $g_{abs} = \left|\exp\left(i\phi\right)\right|$,

with $\phi = ik_z \Delta z$ for the frequency-wave number domain, and

$\phi = i\omega\eta\Delta z$ for the frequency-space domain;

$g_{cc} = g_{cc} . g_{abs}$; $g_{\max}$ are the maximum gains specified and η takes the value $\mathrm{Re}(\Delta u) + i\,\mathrm{Im}(\Delta u)$ in the first modification and $\mathrm{Re}(\Delta u) + i\,\mathrm{Im}(u)$ in the second one. The matrices g_{cc} (one depending on the frequency and wave number, and the other on the frequency and horizontal space coordinate) are updated and stored after g_{eff} is computed. The effective gain algorithms are applied only when $g_{abs} \geq 1$. There are two g_{cc} matrices in the first modified algorithm, whereas in the second, only one g_{cc} matrix is needed. The initial values of the elements of the g_{cc} matrices are set to 1. Comparisons of the two modified algorithms are presented in the results section for heterogeneous and conductive media.

4.2.3 Migration in 3D heterogeneous media

In this section, I present the basis for a possible extension of the split step Fourier technique for migration of 3D multi-component GPR data. Even though multi-component GPR data is not commonly acquired in practice at the present time, some theoretical studies have been already published on migration of this type of data (e.g., van der Kruk, et. al., 2003). However, these migration or imaging techniques assume that the subsurface is homogeneous, and therefore, they can give us a low quality final image if the heterogeneities of the subsurface are important (i.e., if the relative variations of the subsurface properties affect considerably the accuracy and resolution of the final image).

It has been a common practice in the GPR technique that if a 3D GPR image of the subsurface is needed, then a pseudo 3D GPR data set is acquired (i.e., a set of parallel common offset GPR lines using, in general, the broadside-perpendicular mode). This pseudo 3D GPR data is then migrated using seismic software that have been developed for migration of acoustic waves. As we see, this procedure not only fails to take advantage of the extra information associated to the vectorial character of the GPR data, but also can produce unreliable results if the heterogeneities (and, in some exceptional but possible cases, the anisotropy) of the media are not taken into account. In the following lines, I will briefly present the basis to a possible extension of the Split step Fourier migration technique in 3D media.

First, we extend equations 4.6 so that the parameters inside each layer can also vary in the "y" direction, i.e.,

$$\begin{aligned} &\mu(z,x,y) = \bar{\mu} + \Delta\mu(x,y), \\ &\varepsilon(z,x,y) = \bar{\varepsilon} + \Delta\varepsilon(x,y), \text{ and} \\ &\sigma(z,x,y) = \bar{\sigma} + \Delta\sigma(x,y). \end{aligned} \tag{4.12}$$

Then, in the absence of sources, the wave vector equations (4.3 and 4.4) can be written as,

$$\nabla^2 \underline{E} + \bar{\mu}(\omega^2 \bar{\varepsilon} - i\omega\bar{\sigma})\underline{E} = -\left[\underline{J}_E + \underline{J}_m + \nabla\left(\frac{\nabla(\Delta\varepsilon)}{\varepsilon} \cdot \underline{E} \right) \right], \tag{4.13}$$

$$\nabla^2 \underline{H} + \bar{\mu}(\omega^2 \bar{\varepsilon} - i\omega\bar{\sigma})\underline{H} = -\left[\underline{J}_H + \underline{J}_e + \nabla\left(\frac{\nabla(\Delta\mu)}{\mu} \cdot \underline{H} \right) \right], \qquad (4.14)$$

where

$$\underline{J}_E = 2\omega^2 u_0 \Delta u \underline{E} \ ,$$

$$\underline{J}_H = 2\omega^2 u_0 \Delta u \underline{H} \ ,$$

and

$$\underline{J}_m = -i\omega\nabla(\Delta\mu)\times\underline{H} \ ,$$

$$\underline{J}_e = (i\omega\nabla(\Delta\varepsilon) + \nabla(\Delta\sigma))\times\underline{E} \ .$$

Notice that the gradient of the variation of the electromagnetic parameters are responsible for the coupling terms, but these gradients only have horizontal components inside each layer of our model. The definition of u_0 and Δu are the same as in equations 4.8 and 4.9.

First, let us consider the possibilities about the spatial variation of the magnetic permeability. Since most geologic media are not magnetic, the gradient of the magnetic permeability can, in most cases, be neglected (i.e., if $\nabla(\Delta\mu) \approx 0$); then, the vector equation (4.13) will depend only on the electric field (i.e., the explicit coupling term on the magnetic field is neglected), and therefore, this condition simplifies the description of the electromagnetic waves in the subsurface. On the other hand, if the gradient of the magnetic permeability cannot be neglected, then we can use the first equation of 4.2 to express the magnetic field as function of the electric field, and so, the problem can be again reduced to only one wave vector equation on the electric field.

Let us now consider the last term on the right side of equation 4.13. This term depends on the spatial variation of the electric permittivity and is important because it is the responsible to produce a coupling between the components of the electric field in a media where only the electric permittivity is not uniform, changing the magnitude of the components of the electric field when the direction of propagation of the wave changes. Since most geologic media are, essentially, non-magnetic, we expect that this coupling term will be more important than the coupling due to the variation of the magnetic permeability. However, as we will see (and can be intuitively inferred from its form), this coupling term will depend on first and second order derivatives of the electric permittivity making this coupling term very small for smooth heterogeneous media.

Now, taking into account that the variation of the electric permittivity inside each layer (of our model) is only in the horizontal direction, this coupling term can be reduced to,

$$\nabla\left(\frac{\nabla(\Delta\varepsilon)}{\varepsilon}\cdot\underline{E}\right)=\nabla\left[\frac{1}{\overline{\varepsilon}+\Delta\varepsilon}\left(\frac{\partial(\Delta\varepsilon)}{\partial x}E_x+\frac{\partial(\Delta\varepsilon)}{\partial y}E_y\right)\right], \tag{4.15}$$

then, developing the fraction of the electric permittivity in a Taylor's series (dropping quadratic and higher terms of the expansion), we get,

$$\nabla\left(\frac{\nabla(\Delta\varepsilon)}{\varepsilon}\cdot\underline{E}\right)\cong\frac{1}{\overline{\varepsilon}}\nabla\left[\left(\frac{\partial(\Delta\varepsilon)}{\partial x}E_x+\frac{\partial(\Delta\varepsilon)}{\partial y}E_y\right)\right.$$
$$\left.-\frac{1}{2\overline{\varepsilon}}\left(\frac{\partial(\Delta\varepsilon)^2}{\partial x}E_x+\frac{\partial(\Delta\varepsilon)^2}{\partial y}E_y\right)\right], \qquad (4.16)$$

and finally, I neglect the quadratic terms in $\Delta\varepsilon$ to obtain,

$$\nabla\left(\frac{\nabla(\Delta\varepsilon)}{\varepsilon}\cdot\underline{E}\right)\cong\frac{1}{\overline{\varepsilon}}\nabla\left[\left(\frac{\partial(\Delta\varepsilon)}{\partial x}E_x+\frac{\partial(\Delta\varepsilon)}{\partial y}E_y\right)\right]. \qquad (4.17)$$

Notice that this coupling term includes up to second order derivatives of the electric permittivity, as well as first order derivatives (including, in the "z" direction) of the E_x and E_y components.

Now, in equation 4.13, we can substitute the magnetic field as a function of the electric field (using equation 4.2), substitute the source term of equation 4.17, and write the equations for each component separately to obtain,

$$\nabla^2E_x+\omega^2u_0^2E_x=-\omega^2 2u_0\Delta uE_x-\frac{1}{\overline{\mu}}\left[\frac{\partial(\Delta\mu)}{\partial y}\left(\frac{\partial E_y}{\partial x}-\frac{\partial E_x}{\partial y}\right)\right]$$
$$-\frac{1}{\overline{\varepsilon}}\frac{\partial}{\partial x}\left(\frac{\partial(\Delta\varepsilon)}{\partial x}E_x+\frac{\partial(\Delta\varepsilon)}{\partial y}E_y\right), \qquad (4.18)$$

$$\nabla^2 E_y + \omega^2 u_0^2 E_y = -\omega^2 2u_0 \Delta u E_y + \frac{1}{\bar{\mu}}\left[\frac{\partial(\Delta\mu)}{\partial x}\left(\frac{\partial E_y}{\partial x} - \frac{\partial E_x}{\partial y}\right)\right]$$

$$-\frac{1}{\bar{\varepsilon}}\frac{\partial}{\partial y}\left(\frac{\partial(\Delta\varepsilon)}{\partial x}E_x + \frac{\partial(\Delta\varepsilon)}{\partial y}E_y\right), \qquad (4.19)$$

and

$$\nabla^2 E_z + \omega^2 u_0^2 E_z = -\omega^2 2u_0 \Delta u E_z - \frac{1}{\bar{\mu}}\left[\frac{\partial(\Delta\mu)}{\partial x}\left(\frac{\partial E_x}{\partial z} - \frac{\partial E_z}{\partial x}\right) - \frac{\partial(\Delta\mu)}{\partial y}\left(\frac{\partial E_z}{\partial y} - \frac{\partial E_y}{\partial z}\right)\right]$$

$$-\frac{1}{\bar{\varepsilon}}\left(\frac{\partial(\Delta\varepsilon)}{\partial x}\frac{\partial E_x}{\partial z} + \frac{\partial(\Delta\varepsilon)}{\partial y}\frac{\partial E_y}{\partial z}\right). \qquad (4.20)$$

In these equations, I have also made the approximation $1/(\bar{\mu}+\Delta\mu) \approx 1/\bar{\mu}$, which neglects the higher order terms on $\Delta\mu$ (i.e., the same approximation made for $1/(\bar{\varepsilon}+\Delta\varepsilon)$ and described in equations 4.16 and 4.17).

Notice that in the first two equations (4.18 and 4.19) only the E_x and E_y components appear, and no derivatives (in the vertical direction) appear on the right side. As we can see, these two equations are coupled between each other but they can be solved separately from the third equation. After a solution is obtained for the E_x and E_y components, the third equation can be solved to obtain the E_z component (the presence of the vertical derivatives of E_x and E_y in the third equation make not possible to solve this equation simultaneously since a Fourier transform, in the horizontal coordinates, do not eliminate these derivatives).

Applying a Fourier transform in the horizontal coordinates, the first two equations can be solved using the approximation of small angle of incidence that is used in the split step Fourier technique. This approximation simplifies the integrals involving the Green's function and recast the integrals as convolutions that transform to the space domain as multiplications. The solution of these two equations will lead to a matrix operator that correct, in the space domain, the two components simultaneously. An important aspect of this procedure is that it will require the first and second order derivatives of the parameters (magnetic permeability and electric permittivity) in the horizontal directions. These derivatives can be computed in the wave number domain and transformed to the space domain where they can be used for the solution of these equations (notice that we can make a further approximation by neglecting the terms that includes the second order derivatives, and therefore, only the first order derivatives would have to be computed).

The procedure for split step Fourier migration of GPR data in 3D heterogeneous media can be sketched as follows:

1. The multi-component GPR data (i.e., E_x, E_y and E_z components) are Fourier transformed to the frequency and horizontal wave number domains.
2. The phase shift operator, identical to the one used in the 2D case (which includes the imaginary part of the slowness, and therefore also changes the

amplitude of the field), is applied to downward extrapolate the plane waves through the layer (which has mean value properties $\bar{\mu}$, $\bar{\varepsilon}$ and $\bar{\sigma}$).

3. The components are transformed back to the horizontal coordinates domain, and a correction (matrix operator) is applied to the E_x and E_y components at each horizontal position in the layer. Then, these values at the bottom of the layer together with the previous values at the top of the layer are used to compute the local vertical derivative of these components that must be used to apply the correction for the E_z component (in this regard, a normalization by E_z of these derivatives, will linearize the equation for this component, making the correction a multiplication process).
4. The imaging condition is applied to obtain the image at the bottom of the layer.
5. Finally, the components are transformed to the wave number domain and the process is repeated again for the next layer. This loop is carry out until the last layer is reached (bottom of the migration volume).

Some important observations about this technique can be made:

- In general, it is not necessary to acquire the “z” component of the electric field. If we suppose that the recorded E_x and E_y components are associated to homogeneous plane waves that arrive to the receiver antennas, then we can use the fact that the wave vector $\underline{k}$ must be perpendicular to the electric field (i.e., $\underline{k} \cdot \underline{E} = 0$) for such plane waves in the air (whose electromagnetic properties we know). In this way, a decomposition in the plane wave domain of the E_x and E_y components and the application of the above conditions can give us the desired E_z component.

- In the development of this extension of the split step Fourier technique, no correction has been considered to account for the change of the components at the interface between two layers. As I have commented before, when the direction of propagation changes then the relative magnitude of the components of the electric and magnetic fields must also change. At the interfaces, the transmission coefficients give us not only the modification of the components due to the change of direction of propagation, but also the modification of their amplitudes due to the contrast of impedance. The reflectivity technique (chapter 3) can be used to accomplish this correction. The transmission matrices at an interface can be used to correct for the changes of the horizontal components of the electric field. If no correction of the amplitude due to the contrast of impedance wants to be done, the transmission matrices can be normalized to make their determinants equal to 1. Since the application of this correction will be made in the plane wave domain, it will not affect significantly the efficiency of the technique. Notice that this correction is approximated since it assumes that the two layers are homogeneous.

- The fact that equations 4.18 and 4.19 do not depend on E_z and the correction aforementioned does not requires this component, implies that the migration technique can be implemented without it. This is a very important aspect because it reduces the amount of necessary data as well as the computational cost. Notice that not using this component, in the migration technique, has a limitation: it implies that the propagation of the waves should be, preferentially, in the vertical direction since that the component of the electric field parallel to the plane of incidence for a electromagnetic wave that travel almost horizontally is, essentially represented by the E_z component. Nevertheless, this simplification does not restrict more the technique, since this approximation is already made in the split step Fourier technique.

- Finally, if the terms that include the derivative of the electric permittivity and magnetic permeability are neglected, then equations 4.18 to 4.20 reduce to the same form of equation 4.7. This means that, under this coarser approximation, each component can be migrated independently using the technique developed for 2D media (section 4.2.2) and, as expected, the computational cost can be further reduced.

4.2.4 Pre-stack and Post-stack migration

The migration techniques presented in the precedent sections were developed for stack or zero offset GPR sections. However, they can be extended for migration of prestack data using the reflector mapping principle (Claerbout, 1971). Tanis (1998) have shown that the split step Fourier technique is particularly efficient for parallel implementation of prestack migration.

The mathematical expression of the reflector mapping principle is given by (adapted from Claerbout, 1971),

$$M(x,y,z)=\int U(x,y,z,\omega)/D(x,y,z,\omega)\,d\omega \quad , \tag{4.21}$$

where $U(x,y,z,\omega)$ and $D(x,y,z,\omega)$ are the up-going (receiver) and down-going (source) wave fields, respectively, which have been downward extrapolated to the depth "z" where the image (or map) $M(x,y,z)$ is obtained. To avoid the divergence that can occur if $D(x,y,z,\omega)$ becomes very small or equal to zero, the integrand can be substituted by $UD^*/(\zeta+DD^*)$, where ζ is a small positive constant and D^* is the complex conjugate of D. If the spectrum of D is approximately constant, we can suppose that the denominator is constant, and only keep the numerator, reducing the equation 4.21 to,

$$M(x,y,z)=\int U(x,y,z,\omega)D^*(x,y,z,\omega)d\omega \quad . \tag{4.22}$$

This equation represents the imaging condition for prestack migration and requires the downward propagation of the up-going (reflected) and down-going (incident) wave fields. In migration of shot gathers, the incident wave field is generated by the source at the shot point position (with its characteristic radiation pattern), whereas the up-going wave field is recorded at the receiver array on the surface. These wave fields are extrapolated independently and cross-correlated at each depth (equation 4.22) to generate the migrated data at that depth. The final migrated section (or volume) is obtained by superposition of all the independently migrated shot records.

Due to practical reasons, multi-offset reflection data are normally recorded as shot gathers. Prestack migration of these gathers (i.e., in the source-offset coordinates) is more natural because the wave equation that describe the phenomenon is originally expressed in that system of coordinates, thus facilitating the theoretical development of migration techniques; in addition, the data do not have to be reordered. An example of prestack migration of seismic data in the source-offset coordinate system, using the split step Fourier technique, has been presented by Tanis, et. al. (1998). However, diverse reasons such as computational efficiency, reduction of border effects, etc, prestack migration has also be implemented in others coordinate systems, such as receiver-offset or midpoint-offset (e.g., Ottolini and Claerbout, 1984; Purnell, et. al., 2002; and Jin, et. al., 2002), as well as in the tau-p domain (e.g., Akbar, et. al., 1996).

Finally, the correlation between the different components of the incident (source) and reflected (receivers) wave field at each extrapolated level should give us quantitative information about the radar scattering section of the anomalies that generate the reflections. An example of this type of application have been presented by Van Gestel, et. al. (2001) to obtain the orientation of scatterers in the subsurface by using Alford rotation.

4.3 MIGRATION RESULTS IN HETEROGENEOUS AND CONDUCTIVE MEDIA

4.3.1 Effects of the conductivity on the propagation of electromagnetic waves and migration of GPR data

Before I present some results on migration of GPR data in heterogeneous and conductive media, in this section I briefly discuss the effects produce by the conductivity of the media in the propagation of electromagnetic waves and migration of GPR data. To show the importance off these effects, I have plotted the phase velocity, power attenuation by unit distance and gain factor per unit distance as a function of the loss tangent for different frequencies. These curves are shown in Figures 4.4(a), 4.4(b) and 4.4(c), respectively. The loss tangent represents, in general, the ratio between the imaginary and real parts of the square of the slowness and it may include the losses due to conductive, dielectric or magnetic absorption. To generate these curves, we used a constant value for the relative electric permittivity ($\varepsilon_r = 3$) and varied the electric conductivity from 1x10^{-3} S/m to 9x10^{-2} S/m.

Note that for these frequencies, which are within the bandwidth of the GPR technique, and typical values of electrical conductivity and permittivity, the loss tangent can be smaller, equal to or even greater than one. Therefore, the approximation that the loss tangent is much smaller than one depends on frequency, and therefore, it is not valid in general. In this respect, it is interesting to mention that a pulsed radar with a center frequency of about 300 MHz, can

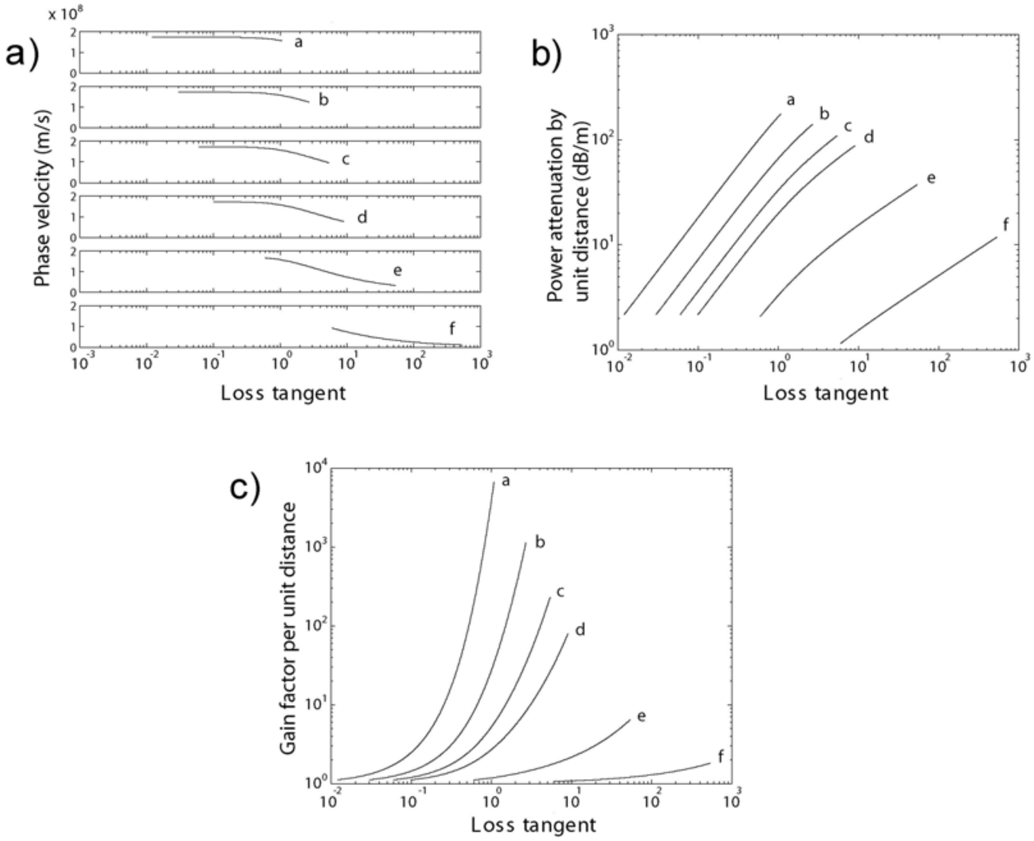

Figure 4.4. Effects of the electric conductivity on the propagation of electromagnetic waves and migration of GPR data. (a) Phase velocity, (b) Power attenuation and (c) Gain factor per unit distance (1 m), in function of the loss tangent. Curves a, b, c, d, e and f correspond to 500, 200, 100, 60, 10 and 1 MHz, respectively.

have frequency components that range from tens of MHz to about 600 MHz (e.g., Bernabini, et al., 1995). Thus, if the high frequencies are rapidly attenuated during propagation, the spectrum of the wavelet will change and the effects of dispersion may become more important (this can be inferred from the different plots in Figure 4.4).

Figure 4.4(c) shows the gain factor per unit distance by which the amplitude of the electric field must be multiplied in order to compensate for the losses due to attenuation. We can see that the slopes of the curves increase with frequency and the gain can change several orders of magnitude for a relatively small change in the loss tangent, making compensation of attenuation naturally unstable. However, for relatively small loss tangent, this problem does not occur and the inclusion of the conductivity can help to improve the resulting image. Synthetic and real data presented in the following sections demonstrate some of these benefits.

4.3.2 Airborne radar data

In this section, I present a portion of a 2D air-borne radar line acquired in Antarctica. It is used to show the importance of applying an algorithm that allows us to take into account the lateral variation of the velocity (no conductivity or dispersion is considered in this example). Figure 4.5(a) shows the raw airborne radar data and Figure 4.5(b) shows the two models used to migrate the data. In

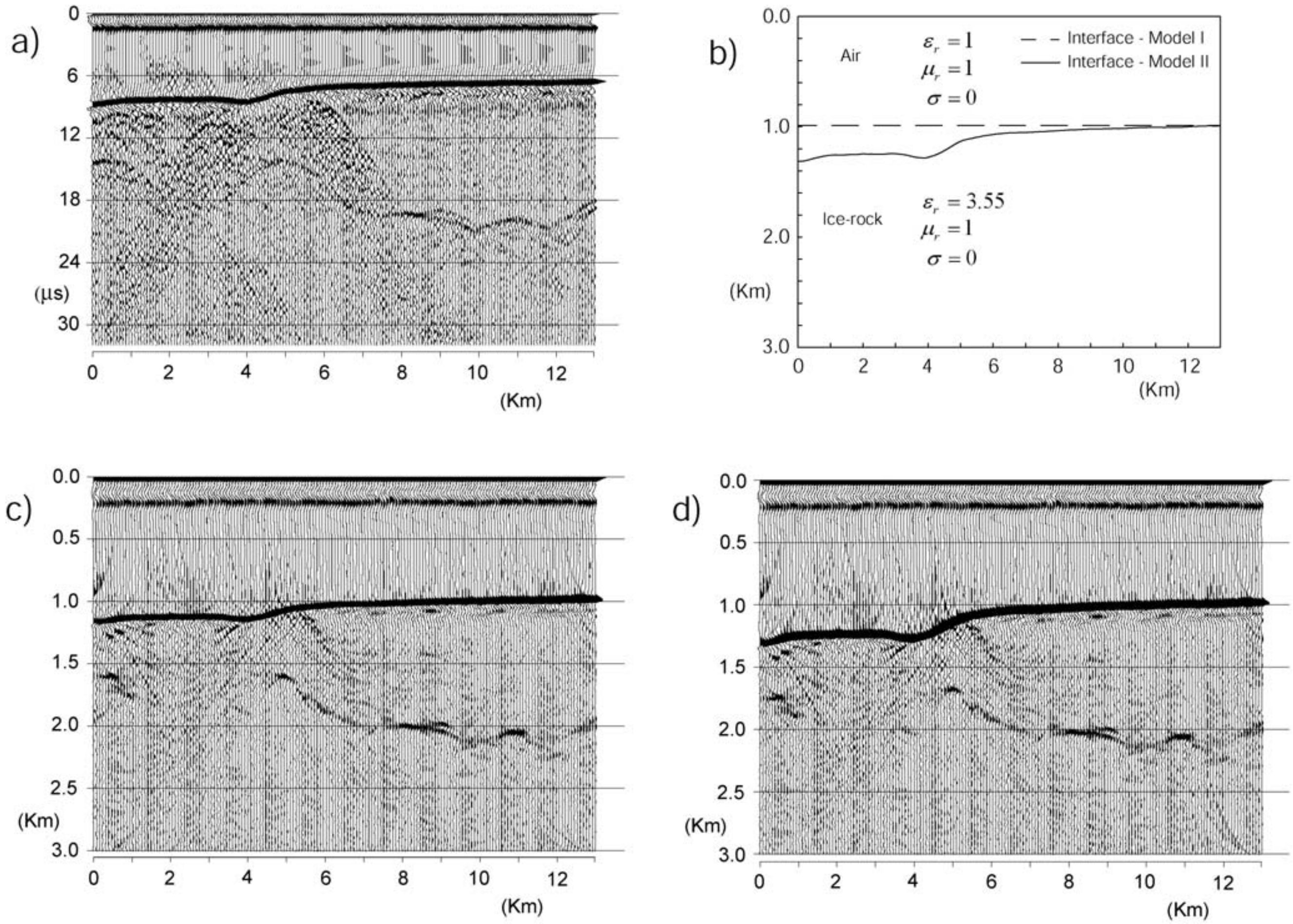

Figure 4.5. (a) Unmigrated airborne radar data, (b) employed models for migration, (c) migration using model I, and (d) migration using model II.

both the models only two homogeneous media (air and ice) are considered and the difference between the two models is restricted to the form of the air-ice interface. The intention of this example is to demonstrate the effect that the lateral change in velocity (due to the ice topography) produces in the migrated section; the smaller heterogeneities within the ice are ignored. Figures 4.5(c) and 4.5(d) show the migrated sections obtained by using a planar interface (model I) and a non-planar interface (model II), respectively. Note how the air-ice interface imaged with the model II is placed at a different position and how the topographic details are improved. Similarly, note the improved image for the ice-bedrock interface and internal reflections inside the ice layer, especially in the middle of the section where slope of the ice topography is high. In summary, an improved image of the reflectors, due to increased resolution and focusing of the diffractions, is obtained when the lateral variations of the velocity are taken into account.

4.3.3 Synthetic data: examples of migration in conductive media

In this section, a set of synthetic data (2D case) is used to show how, by taking into account the conductivity of the media in the migration algorithm, we can improve the image and recover the reflectivity values in the migrated section.

Figure 4.6 shows the models used to generate the synthetic data. The main difference between the models shown in Figure 4.6 (a) with those in Figure 4.6 (b) is the smoothness of the lateral borders of the conductivity zones (rectangles). In Figure 4.6 (a) the lateral change of the conductivity is abrupt whereas in Figure

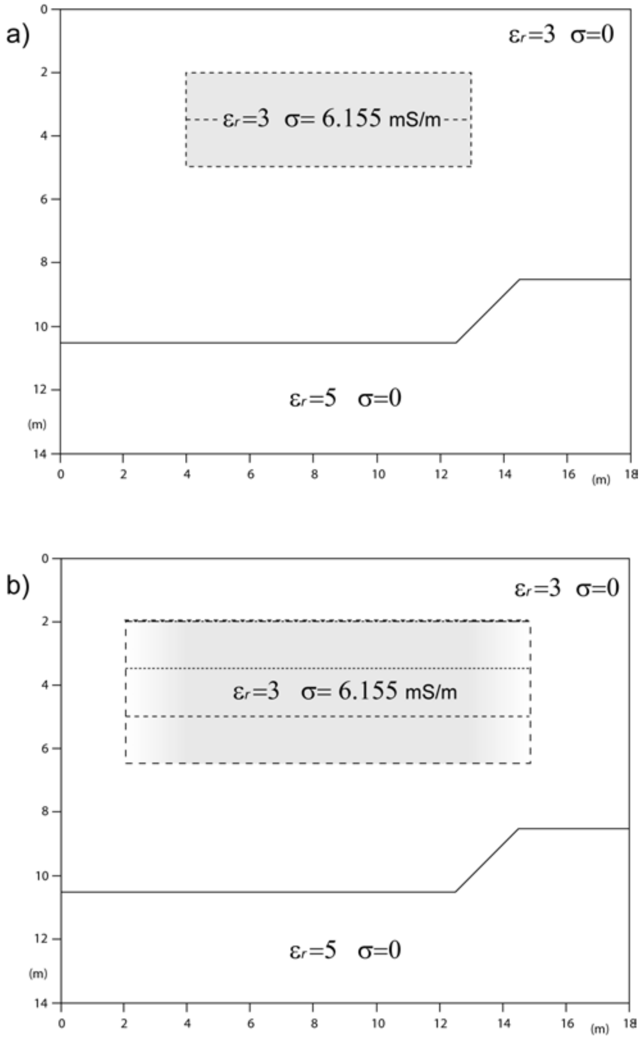

Figure 4.6. Models used to generate the synthetic data used to compare the migration algorithm for different thicknesses of the conductivity zones and the effect of its lateral variation. The models in figures (a) and (b) are essentially the same except that in (b) the lateral borders of the conductivity zones are smoothed by adding transition zones (semi-hanning windows) of length 2 m. The relative magnetic permeability is equal to 1 in all the media.

4.6 (b) the change is gradual (semi-hanning window). In both the figures the dashed lines represent rectangular conductivity zones with different thicknesses (one and two skin depths in Figure 4.6 (a), and one, two and three skin depths in Figure 4.6 (b)). Each rectangle represents a different model used in the synthesis of the data. The electrical and magnetic properties inside the different media of each model are uniform except in Figure 4.6 (b) where the conductivity zones are smoothed at their lateral borders. Note that the tops of the rectangles are common for all the models. Now, we can compare the effects produced by different lateral variation and thicknesses of the conductivity zones.

To generate the synthetic data, I used a 2D time domain finite difference technique (TE mode, see chapter II). The source consisted of a line current (perpendicular to the plane of the page in Figure 4.6) placed on the upper boundary of the model. I generated zero offset sections by placing the source in each horizontal position and recording the electric field at the same position; in this way, we naturally generate the data (as recorded in practice) and avoid any possible artifact that could be introduced by using an exploding reflector modeling technique. This aspect is important because we are interested in both, the qualitative and quantitative aspects of the resulting image. The form of the current pulse used to generate the fields was a squared hanning window with a duration of 5 ns. This makes the principal frequency of the radar equal to 200 MHz. At this frequency, the skin depth in the conductivity zones (6.155 mS/m) is

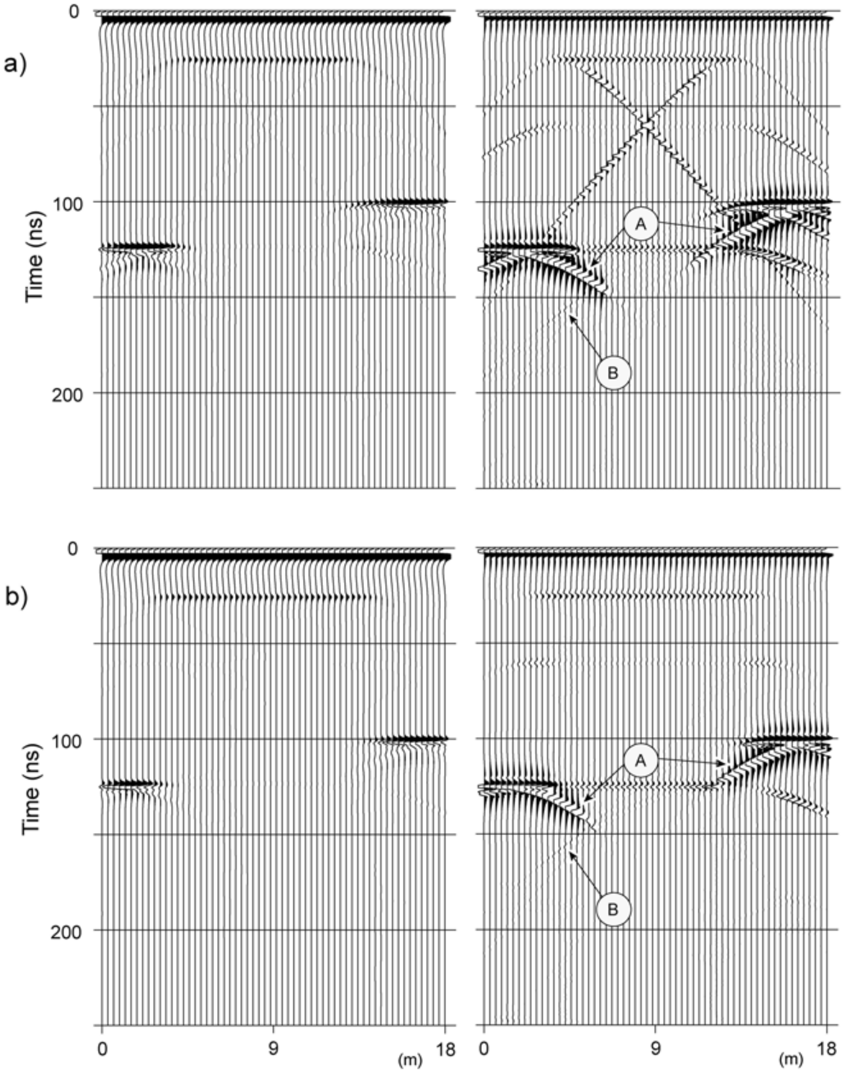

Figure 4.7. Zero offset sections obtained for the models whose conductivity zones have a thickness equal to two times the skin depth. (a) Corresponds to the model with abrupt lateral change of the conductivity (Figure 4.6(a)). (b) Corresponds to the model with smooth lateral change of the conductivity (Figure 4.6(b)). On the left are the unmigrated sections without AGC and on the right, the same sections with AGC. The length of the window used for the AGC operator is equal to the length of the wavelet. See main text for comments on the signals marked as "A" and "B".

equal to 1.5 m. An absorbing boundary condition was used to minimize the reflections coming from the boundary of the model.

Figure 4.7 shows the zero offset sections obtained for the models whose conductivity zones have a thickness equal to two times the skin depth. The signal has been compensated for cylindrical divergence and their plots, with and without AGC, are shown. Note how the conductivity strongly reduces the amplitude of the underlying reflectors, in such a way that even with an optimal AGC (with a window length equal to the duration of the wavelet) they are hardly observed. For example, the reflected energy (pointed as “B”) coming from the dipping reflector of the lower interface is hardly recognized. In the same way, note the incomplete hyperbolas (pointed as “A”) that appear below the horizontal reflector. These diffraction-like signals are generated by the reflection of the waves in the vertical walls of the conductivity zones or by diffraction around these borders.

Figures 4.8 and 4.9 show the migrated sections (without and with AGC applied, respectively) corresponding to the models of figure 4.6(a), and figures 4.10 and 4.11 show the migrated sections corresponding to the models of figure 4.6 (b) (one and two skin depths, only). The panels on the left are the migrated sections obtained without taking into account the conductivity of the media, whereas those on the right are the sections obtained by taking into account the

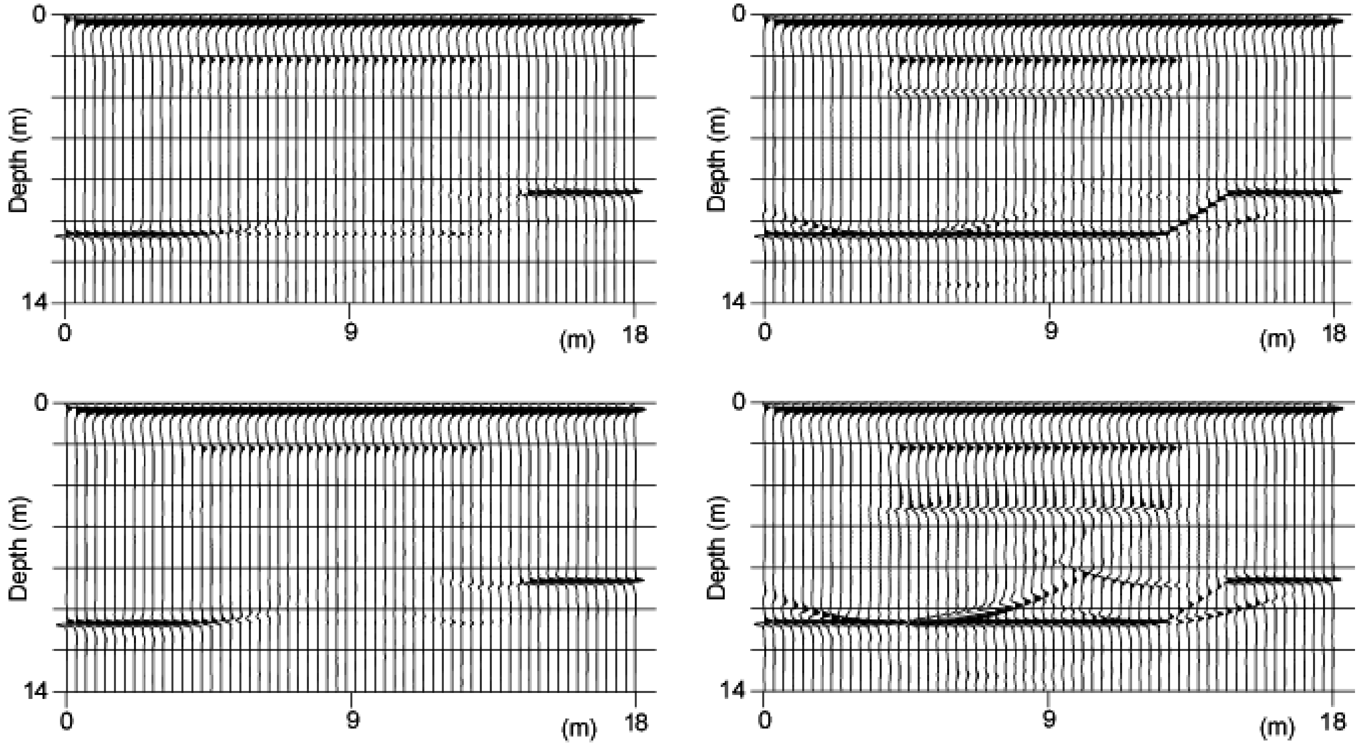

Figure 4.8. Migrated sections corresponding to the models with abrupt lateral change of their conductivity zones (Figure 4.6(a)). On the top are the migrated sections corresponding to the model with a conductivity zone with thickness equal to one characteristic skin depth, whereas on the bottom are the migrated sections corresponding to a thickness equivalent to two skin depths. On the left are the migrated sections obtained without taking into account the conductivity and on the right are the migrated section obtained by taking into account the conductivity of the media.

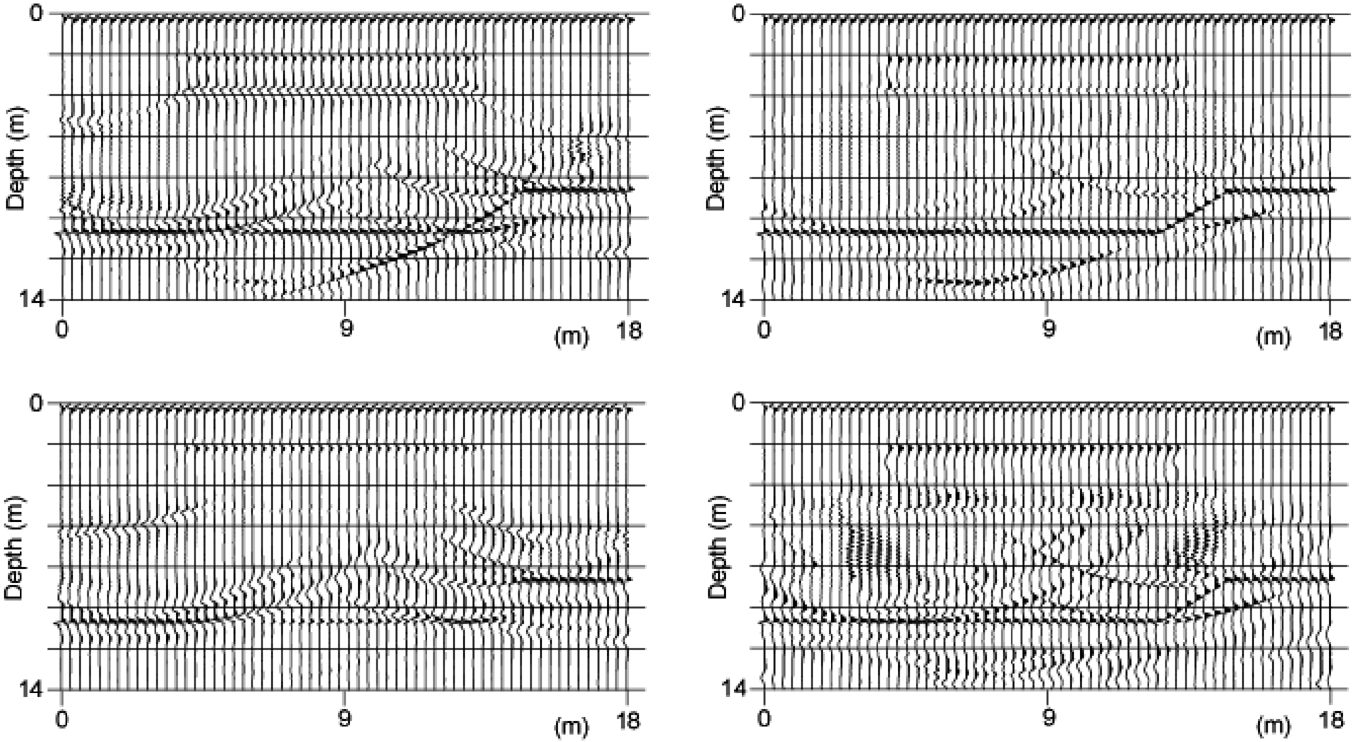

Figure 4.9. Same as Figure 4.8 but with AGC applied.

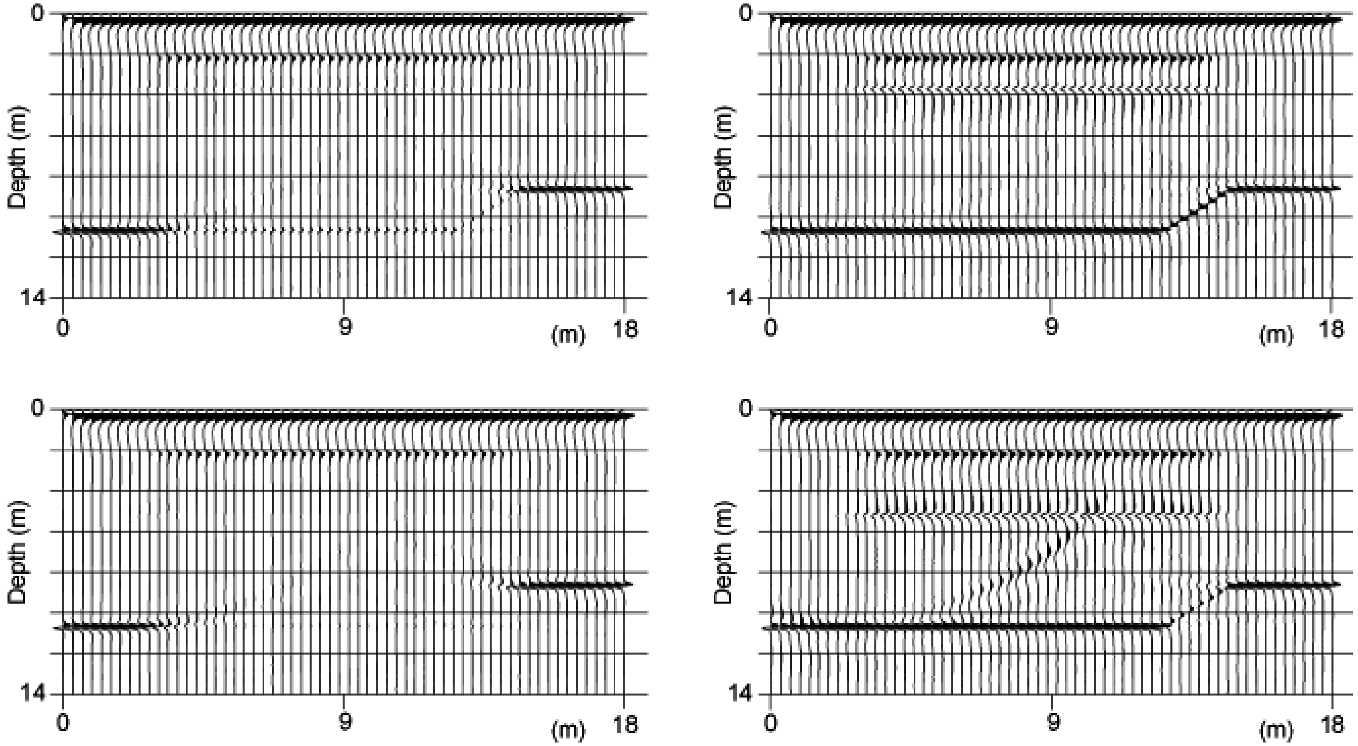

Figure 4.10. Migrated sections corresponding to the models with thicknesses equal to one and two skin depths and smoothed lateral changes of their conductivity zones (Figure 4.6(b)). On the left are the migrated sections obtained without taking into account the conductivity and on the right are the migrated section obtained by taking into account the conductivity of the media.

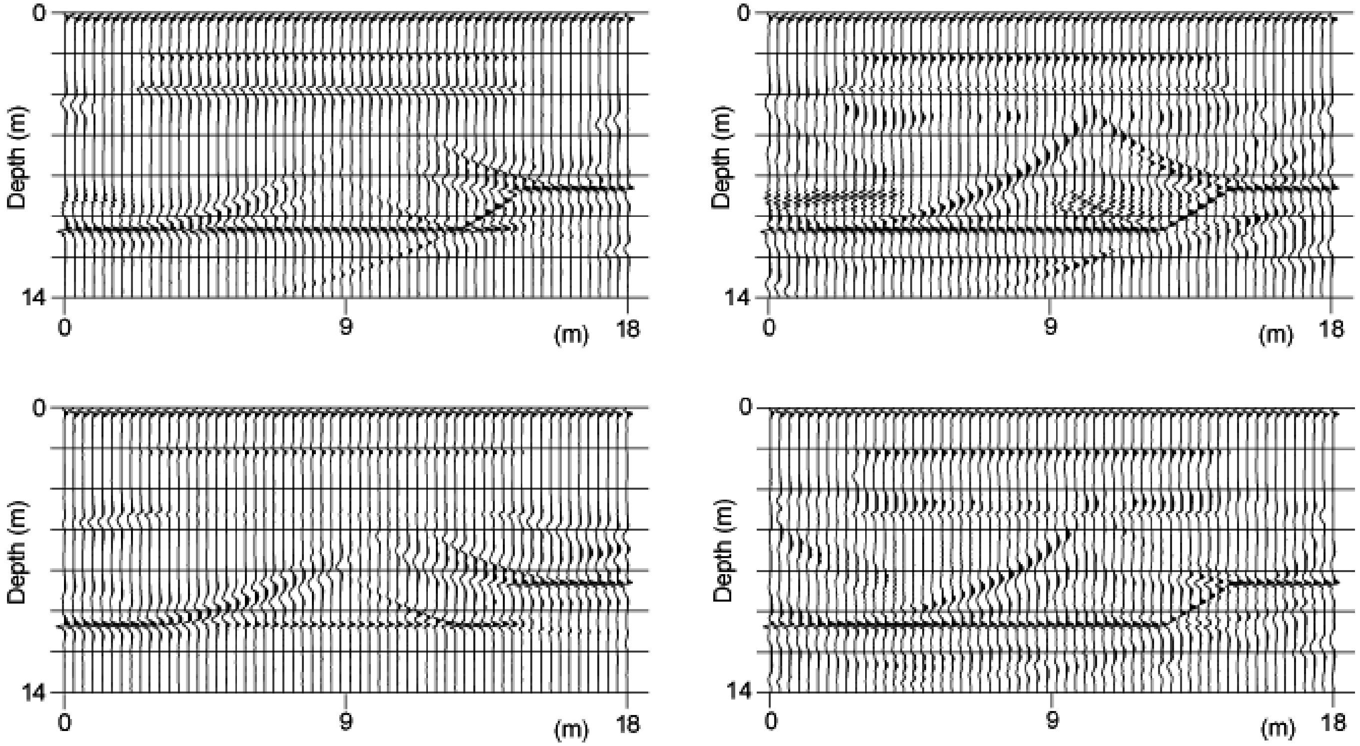

Figure 4.11. Same as Figure 4.10 but with AGC applied.

conductivity. The direct arrival has not been suppressed in any of the sections; so, in the plots without AGC (Figures 4.8 and 4.10) a maximum deflection equal to 8 and a clip level equal to 1 has been used to allow observation of the reflections. In the sections with AGC applied, the length of the window used for the AGC operator was 0.63 m, which is slightly smaller than the main wavelength of the radar signal in the upper media, $\lambda_{main} \cong 0.86\,\text{m}$, and no clipping was used. Additionally, all the migrated sections where filtered with a band pass filter ($\lambda_{\min} = 0.16\,\text{m}$ to $\lambda_{\max} = 3.15\,\text{m}$). The effect of this filter on the sections without AGC is not significant, but it is particularly important for the sections with AGC because of the amplification that the AGC does to the relatively small noise.

Comparing these results, we see that even with AGC applied, the quality of the migrated sections is improved when the conductivity of the media is taken into account, not only in defining the form of the reflector but also in recovering the reflectivity values (plots without AGC). When the thickness of the conductivity zone increases, the reflectivity data from the dipping reflector begins to deteriorate. This deterioration of the reflectivity data from the dipping reflector, with increasing thickness of the conductivity zones, is related to the approximation of the homogeneous waves. For the particular form of the conductivity zones used in these models, the approximation of homogeneous waves is most satisfactory for those waves that travel vertically, making possible to completely recover the reflectivity data from the horizontal reflectors. Nonetheless, we have seen that very good results can be obtained for cases where the thickness of the conductivity zones are on the order of two times the skin depth and that, for slightly larger thicknesses (of the conductivity zones), the approximation of homogeneous waves still allows the migration to be numerically stable. When the lateral change of conductivity is smooth, the quality of the migration is still preserved for conductivity zones even thicker than two times the skin depth. Figure 4.12(a) and 4.12(b) show the migrated sections obtained without taking and by taking into account, respectively, the conductivity during migration of the section that correspond to the model with a thickness equivalent to three skin depths shown in Figure 4.6(b). On the left are the migrated sections without AGC applied, and on the right the same sections with AGC applied. Notice that even in this case, including the conductivity in the migration process improves the quality of the final image, recovering correctly the reflectivity of the horizontal reflectors and still revealing the dipping reflector whose presence can not be inferred from the migrated section obtained without taking into account the conductivity of the media.

In Figures 4.8 through 4.12 we can notice that there are some smile-like signals centered below the lateral borders of the conductivity zones. This energy is related to the reflections and diffractions indicated by arrows (A) in Figure 4.7. The amplification of this energy causes degradation of the quality of the migrated section, but their effects are smaller for the models with laterally smoothed

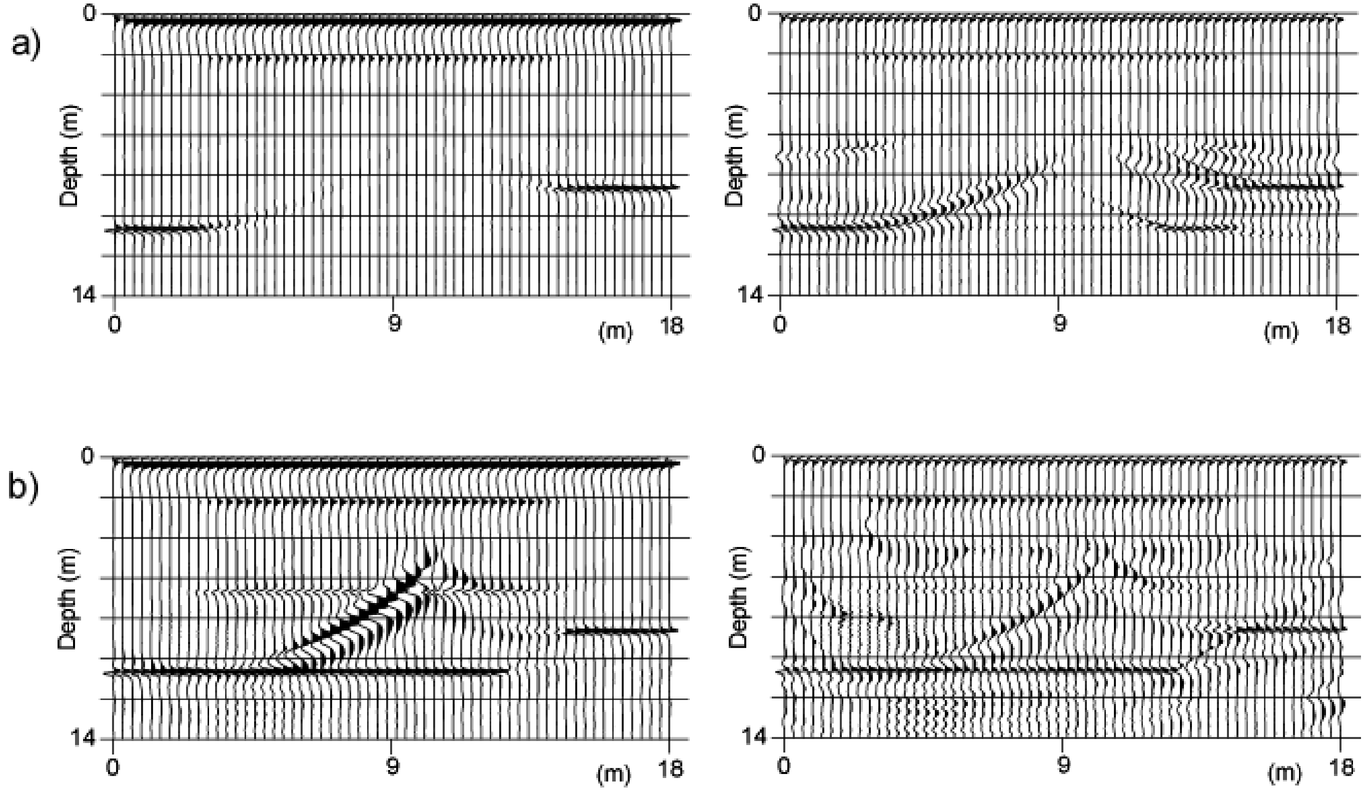

Figure 4.12. Migrated sections corresponding to the model with a laterally smoothed conductivity zone whose thickness is equivalent to three skin depths (Figure 4.6(b)). (a) Migration without taking into accounts the conductivity of the media. (b) Migration taking into accounts the conductivity of the media. On the left and on the right are the sections without and with AGC, respectively.

conductivity zones. We see that these signals become appreciable when the thickness of the conductivity zone is about two times the skin depth in the case of laterally abrupt conductivity zones (Figures 4.8 and 4.9) and about three times the skin depth in the case of laterally smoothed conductivity zones (Figure 4.12). Therefore, we can conclude that greater stability and better results are obtained when the lateral changes of the model are smooth. This observation is expected based on the fundamental assumption of the split step Fourier technique.

To test the modifications of the migration algorithm for higher conductivities, we use the model shown in Figure 4.13. In this model, the upper medium has a uniform conductivity so that the bottom reflector (interface between upper and lower media) is at a depth approximately equal to one skin depth. Embedded in the upper medium is a small zone of high conductivity 40 mS/m (with smoothed lateral boundaries). Inside this high conductivity zone, the radar signal has a skin depth of about 26 cm, i.e., about a quarter the thickness of the zone. Figures 4.14 and 4.15 show the results of the migrated sections without and with AGC, respectively. No filtering was applied to the sections shown in Figure 4.14. A special case is shown in Figures 4.14(b) and 4.15(b) corresponding to the migration obtained by considering the upper medium as homogeneous (i.e., without the high conductivity zone) with a uniform conductivity of 1 mS/m and no gain limitation was used during migration.

Comparing these results (Figures 4.14 and 4.15), we see that the first modification of the migration algorithm, using a total limiting gain equal to the compensation that should be applied in a two-way pass through a two skin depths length (total limiting gain equal to 54.6) yields the best results for imaging the bottom of the high conductivity zone while still preserving the quality of the lower reflector (interface between the upper and lower media). In Figure 4.14(b) the image of the lower interface (which includes the dipping reflector) is good. However, in this migrated section, the reflection from the bottom of the high conductivity zone is not very well distinguished, even with the application of AGC.

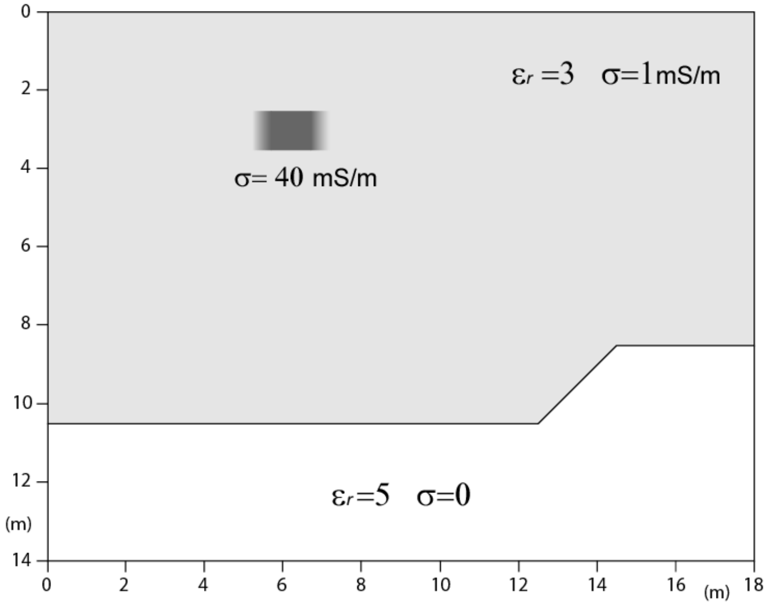

Figure 4.13. Model used to test the limited gain modifications of the migration algorithm implemented for high conductivity (or highly lossy) media.

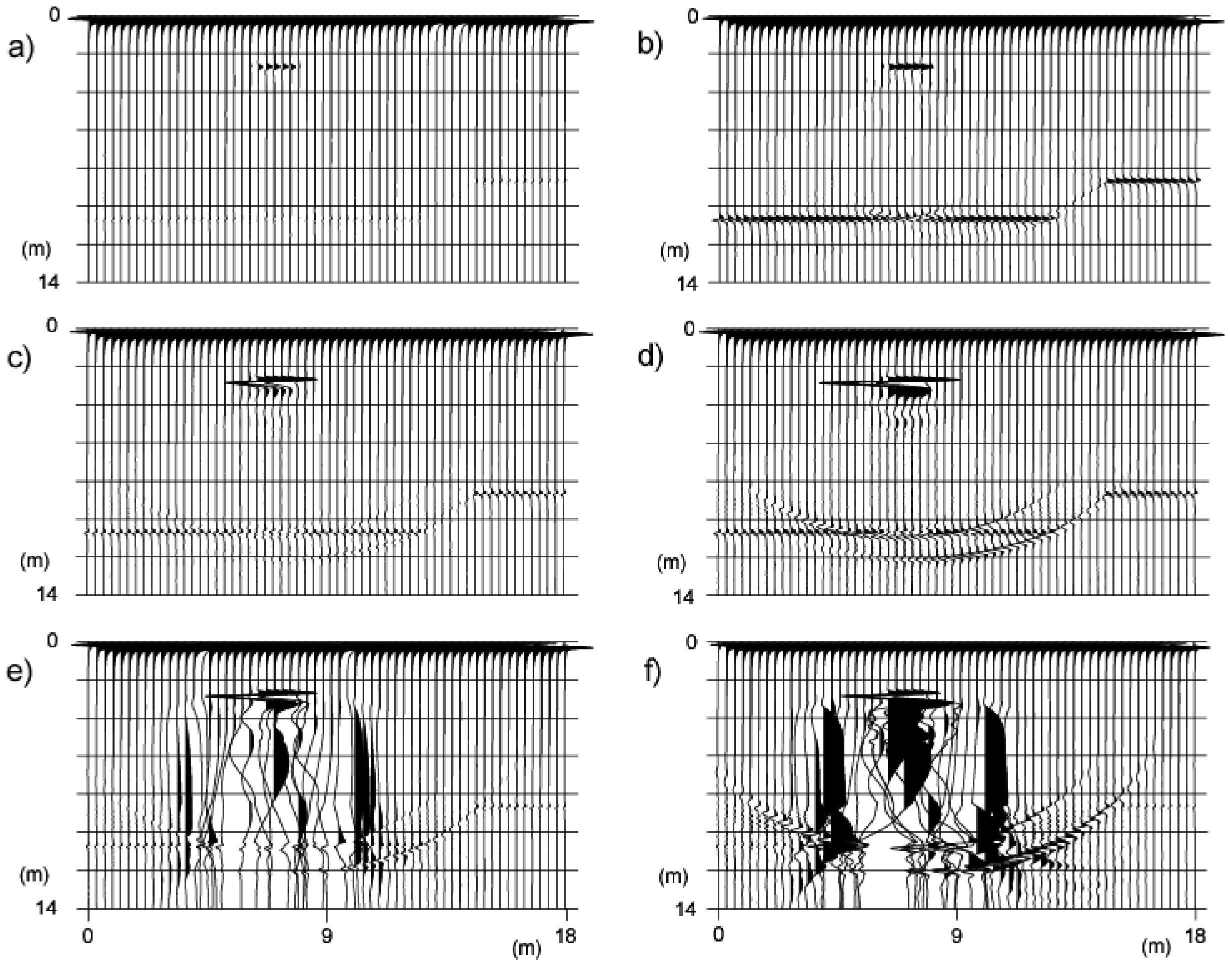

Figure 4.14. Migrated sections for high conductivity media (model shown in Figure 4.13). (a) Migrated section obtained without including the conductivity. (b) Migrated section obtained with a uniform conductivity in the upper medium equal to 1 mS/m (ignoring the high conductivity zone). (c) and (d) show the migrated sections obtained with the first modification of the migration algorithm using a total limited gain equal to 54.6 and 403.4, respectively. (e) and (f) show the migrated sections obtained with the second modification of the algorithm using a total limited gain equal to 54.6 and 403.4, respectively. No filter and no AGC have been applied to these sections in order to compare, quantitatively, the results of these algorithms. Note the deterioration and distortion produced by the second modification of the migration algorithm.

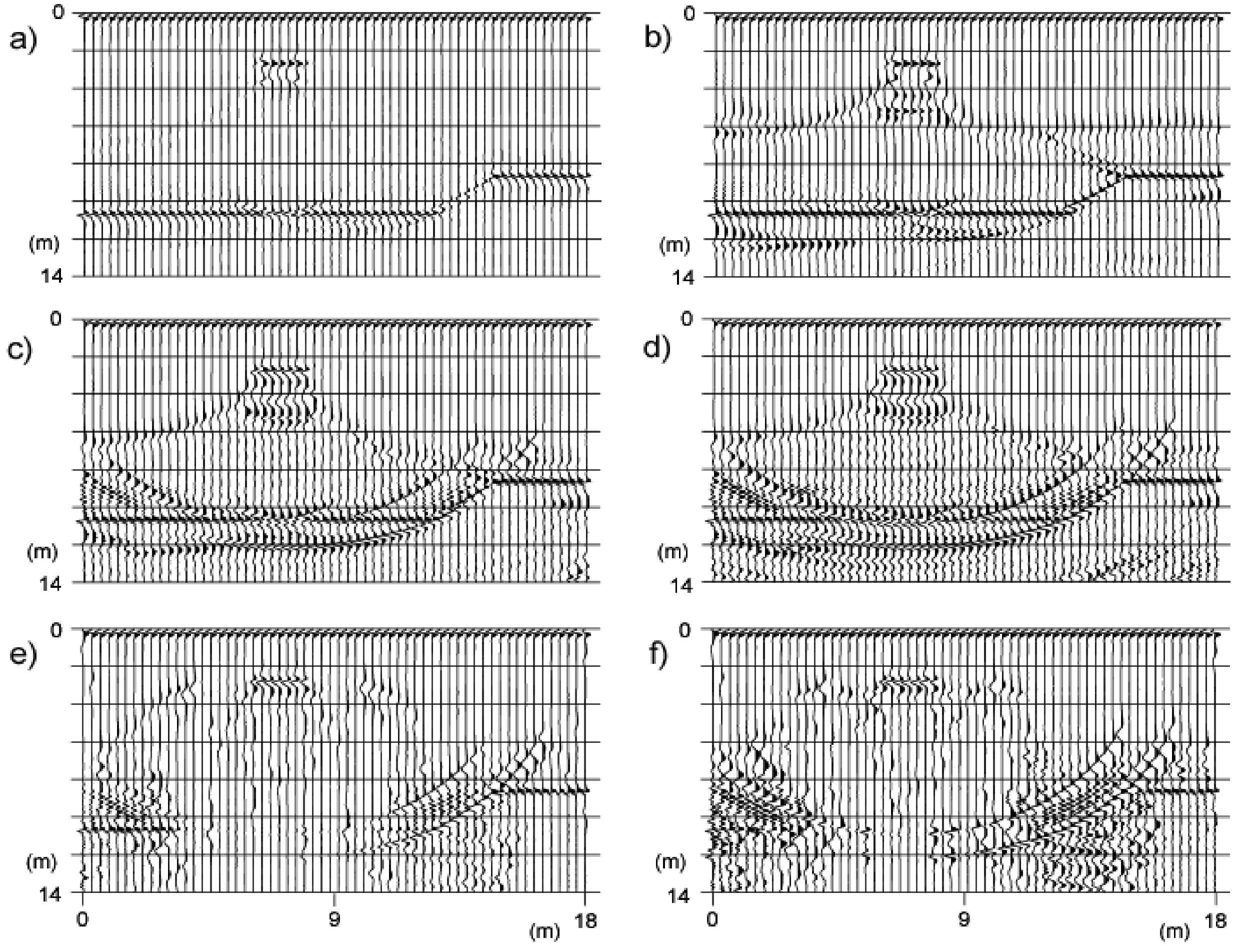

Figure 4.15. Same as Figure 4.14 but with AGC applied.

It is also interesting to note that the high conductivity zone not only strongly attenuates the higher frequency components of the radar signal but also the dispersion effects are expected to be appreciable (the loss tangent in this media, at a frequency of 200 MHz, is equal to 1.2). In Figures 4.15(a) and 4.15(b) we see that the image of the dipping reflector and part of the horizontal interface directly below the high conductivity zone are migrated incorrectly. The image observed at these positions is affected by dispersion and strong attenuation caused by the high conductivity zone. However, in Figures (c) and (d) of Figure 4.14 (or 4.15), the image at these positions begins to form at the right location, and with the right phase, when the total limiting gain is increased. Unfortunately, the high conductivity zone produces reflections on their lateral border that are also amplified by the migration algorithm (smile or semi-circle like signals) and they begin to deteriorate the image. Because of their origin, these reflected (or scattered) waves are imaged very close to the interface of interest and interfere with the formation of the image at these critical areas. This situation makes it very difficult to evaluate how much of this improvement is due to the compensation of the dispersion effects and how much could be attributed to this interference. In any case, we have seen that the improvement obtained with the first modification of the migration algorithm is appreciable, even when we use a total limiting gain equal to 403.4 (compensation gain corresponding to three skin depths). Finally, the results obtained with the second modification of the method (gain applied only in the frequency-space domain) are shown in (e) and (f) of Figures 4.14 and 4.15. These results indicate that a compensation of the attenuation applied only in the vertical direction is not adequate, altering and deteriorating considerably the reflectivity data, in particular the low frequency component.

4.3.4 Cave site GPR data

In this section, I present the results obtained for a GPR data set acquired at a cave site located 5 km south of Georgetown, Texas (a paleo-karst system developed in the Edwards Formation and overlaid by the Georgetown Formation). A common offset 2D line and four CMP gathers (at selected locations in the line) were acquired using the perpendicular broadside mode. Figure 4.16 shows the location of the line relative to the underlying cave and filled paleo-sink structures. Figure 4.17 shows the raw data (common offset section), indicating the selected location where the CMP gathers were acquired. The dominant frequency of the radar signal was 50 MHz. In the acquisition of the common offset section, the separation between the transmitter and receiver antennas was 1.6 m, the displacement (or distance) between mid-points 0.2 m, and the time sampling interval 0.8 ns. In the acquisition of the CMP data the same frequency and time sampling interval were used, but the offset between transmitter and receiver was increased in step of 0.5 m. The number of shots stacked per location was 128 for all the data.

Figure 4.18 (a) shows an example of the CMP data collected at the mid-point location x=14 m (AGC has been applied, and only the interval where coherent reflections are observed is shown in the figure). The data were converted to SEG-Y format and a velocity analysis was carried out using seismic processing software. Figure 4.18 (b) shows the CMP after NMO using the velocities shown on the right side. The velocities obtained from this analysis are used to compute the electric permittivity of the media supposing that $\mu_r \cong 1$ (this is generally the case for carbonate rocks, the type of rocks present in this area). At the dominant frequency of the radar signal and with the estimated mean value of the electric conductivity (see discussion below), the correction due to the conductivity of the media on the computation of the electric permittivity using the velocity values is very small (less than 1%) and can be ignored in the initial estimate of the electric permittivity.

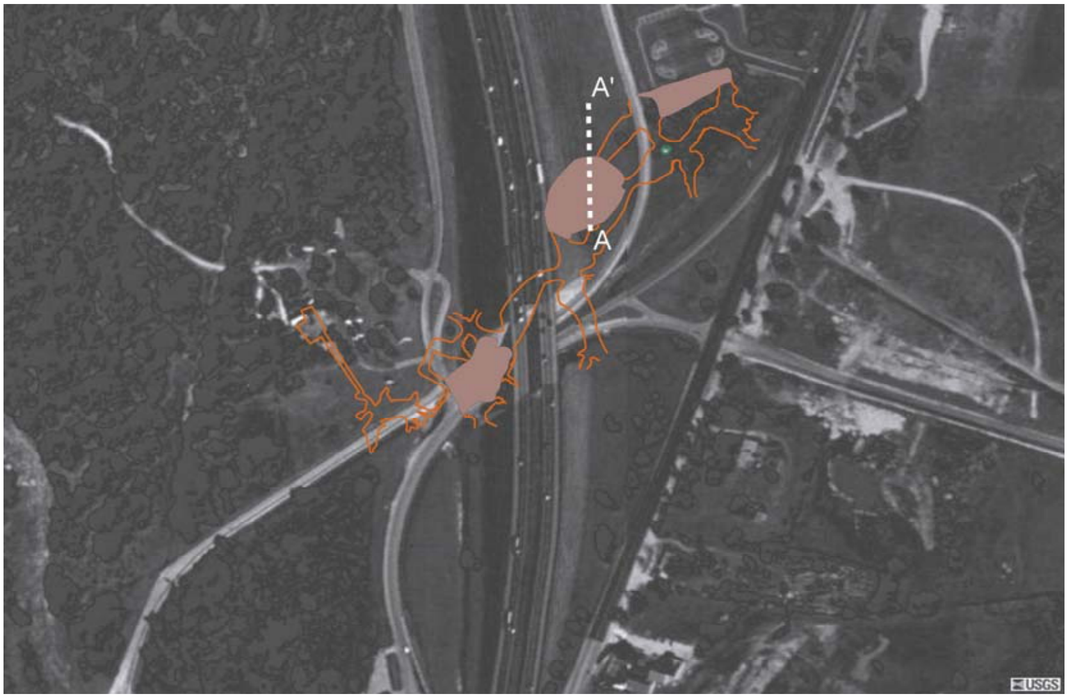

Figure 4.16. Cave site location. The white dashed straight line indicates the location of the GPR line. A partial map of the Inner Space Cavern is sketched on this aerial photo to indicate the relative position of the GPR line respect to the cavern. The shadowed zones indicate filled paleo-sinks. The areas between open lines represent the passages of the cavern (Fieseler, et. al., 1978). The mean depth to the ceiling of the cavern, near to the GPR line, is about 18 m.

From the observed attenuation of the radar signal (through the overlying carbonate layers of the Georgetown Formation), the conductivity of the layers is estimated to be on the order of 3 or 4 mS/m. This result could be expected from the observation (in the subsurface, North West Texas) that the Georgetown Formation has a low permeability and constitutes an effective seal of the Edwards formation (Galloway, et. al, 1983). Reviewing the literature, I could not find specific information on the conductivity of the Georgetown Formation. However, the Ellenberger Group (Ordovician) has a similar depositional environment to the Georgetown Formation (Cretaceous) and also has a low permeability. McMechan, et. al. (2002) made a study of the properties of the Ellenberger rocks and their response to the GPR signal. They found that, for very low water saturation (ambient humidity), the conductivity of these carbonate rocks are of the order of 1 or 2 mS/m. In general, the conductivity of carbonate rocks can be increased if they have intermediate to high porosity and are filled with a conductive fluid. In the case of the Ellenberger Group and the Georgetown Formation, a high saturation of fresh water could increase its conductivity, but due to the low conductivity of fresh water and low permeability of these formations, we expect that the conductivity will remain in the same order of magnitude, in agreement with the estimation obtained from the observed attenuation of the GPR signal.

To obtain a better estimate of the local conductivity in the medium, I used two empirical relationships: Archie's law and a general correlation between water content and electric permittivity (of soils) as reported by Topp (1980); a brief explanation of this computation procedure is given in Appendix D. The values of permittivity and conductivity obtained at the CMP locations are then interpolated and smoothed to build the models shown in Figure 4.19. The high correlation between these two models is expected from the observation that the pore fluid, in carbonate rocks, mainly defines the electric conductivity and permittivity of these

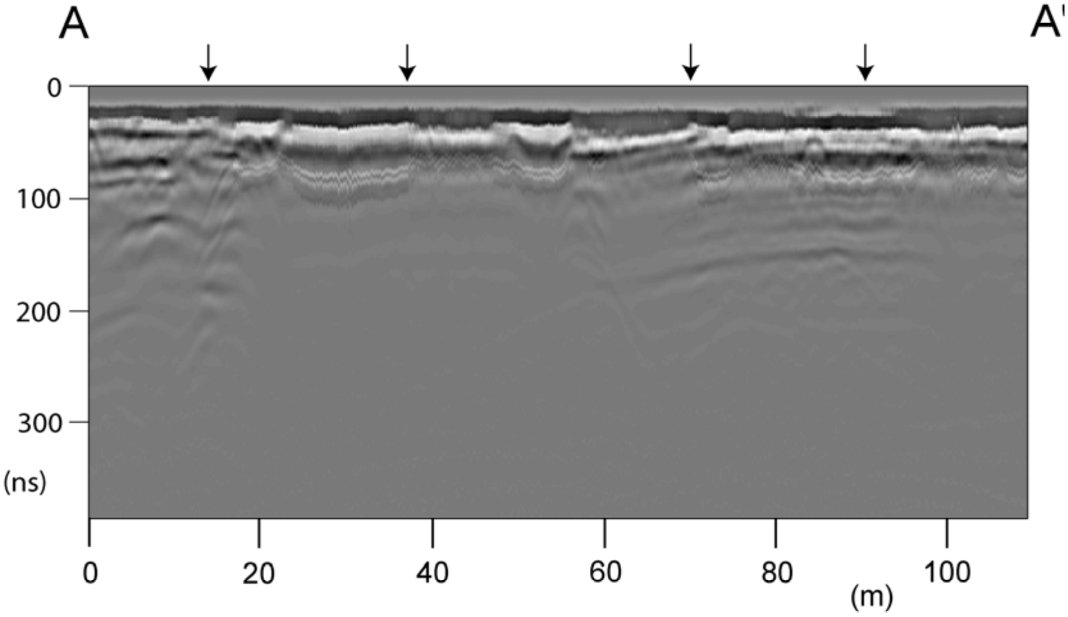

Figure 4.17. Unmigrated GPR line (common offset section) at the cave site. The arrows indicate the position where CMPs where acquired. A spherical gain correction has been applied to these data but neither AGC nor clipping has been used. Note the attenuation of the radar signal. The zone where nearly no signal is observed (below 100 ns and between 20 and 55 m) corresponds to a filled paleo-sink (see Figure 4.16). This absence of signal could be due to the lack of contrasting electromagnetic impedances or/and a higher attenuation of the GPR signal in this zone.

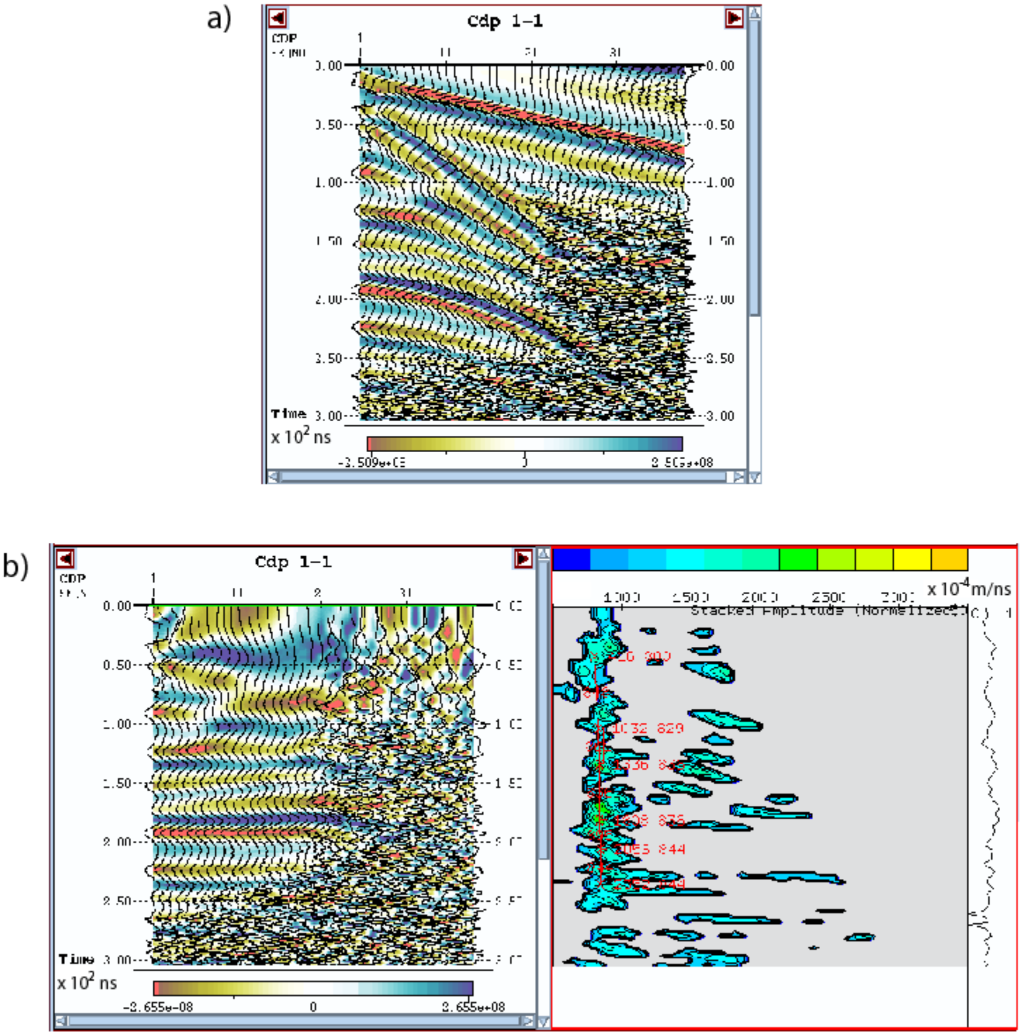

Figure 4.18. Velocity analysis of the GPR CMP gather acquired at the location x=14 m (see Figure 4.17). (a) CMP gather and (b) NMO corrected using the velocity shown on the right. AGC is used in both the plots.

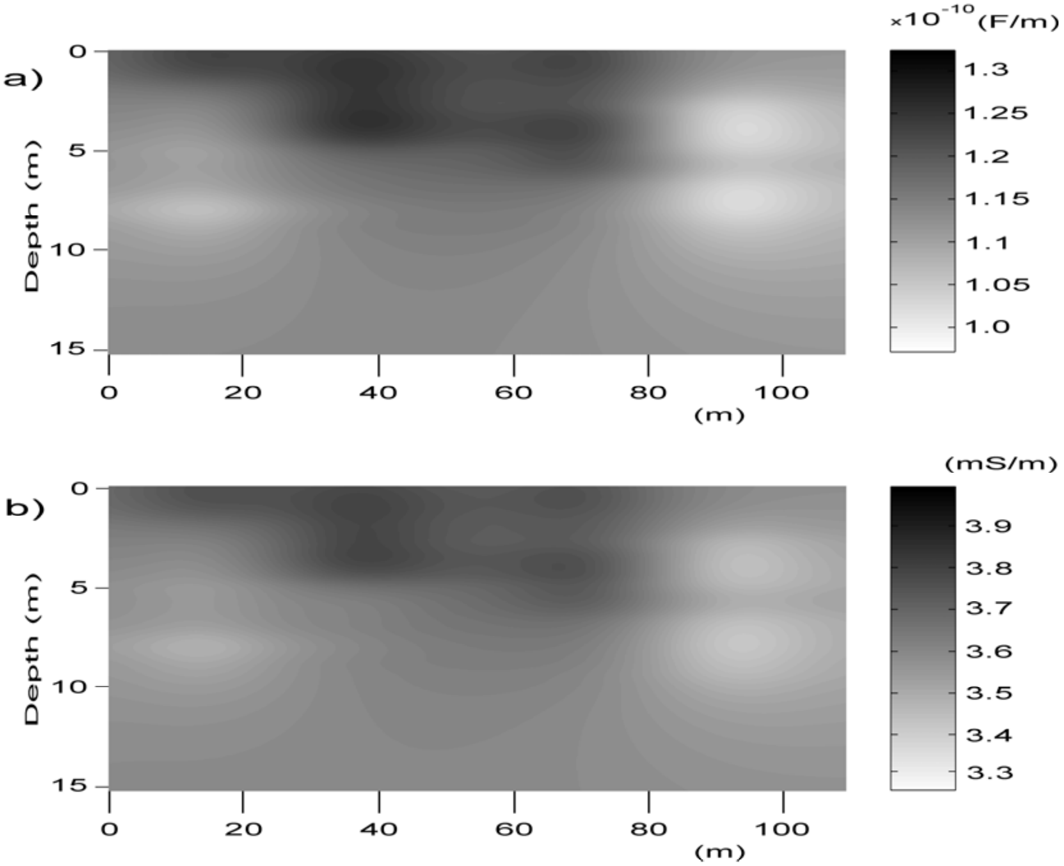

Figure 4.19. Estimated subsurface models for the electric permittivity (a) and conductivity (b) at the location of the GPR line in the cave site.

rocks. Even though these models where estimated at the main frequency of the radar signal, we suppose that the electric permittivity and conductivity do not change within the bandwidth of the radar signal (the variation of these parameters could be included in the migration process if this information were available). It must be mentioned that the conductivity of the filled paleo-sink zones (areas of reduced amplitude for the radar signal in Figure 4.18) might be greater than the values estimated in Figure 4.19. This is due to its lithology (probably carbonaceous claylike sediments) that can make the contribution of the grain surface conductivity in Archie's law important. Using the conductivity model of Figure 4.19(b), under the supposition that the conductivity of the filled paleo-sinks are underestimated, would yield results equivalent to the case shown on Figure 4.14(b). However, if necessary, we still could use the first modification of the migration algorithm to obtain good results. More important than this is the fact that, for this conductivity model (Figure 4.19(b)), the mean skin depth value (at 50 MHz) is about 5.2 m. This means that I have been able to obtain a stable migration (without limiting the applied gain) to a depth greater than three times the skin depth, as shown in Figure 4.20(b). We can see that noise and diffractions from scatterers on the surface are the main deteriorating factors at the bottom of the migrated section.

Comparing Figures 4.20(a) and 4.20(b), we can see that including the conductivity of the media allowed us to recover a better estimate of the reflectivity. Even though the conductivity model has been estimated from empirical laws that relate the electric permittivity and conductivity in these rocks, the conductivity of the media could be estimated by other geophysical techniques (DC resistivity, TDEM or FDEM) giving us a better conductivity model in order to migrate, more accurately, the GPR data. In any case, the results obtained by using the present conductivity model are encouraging.

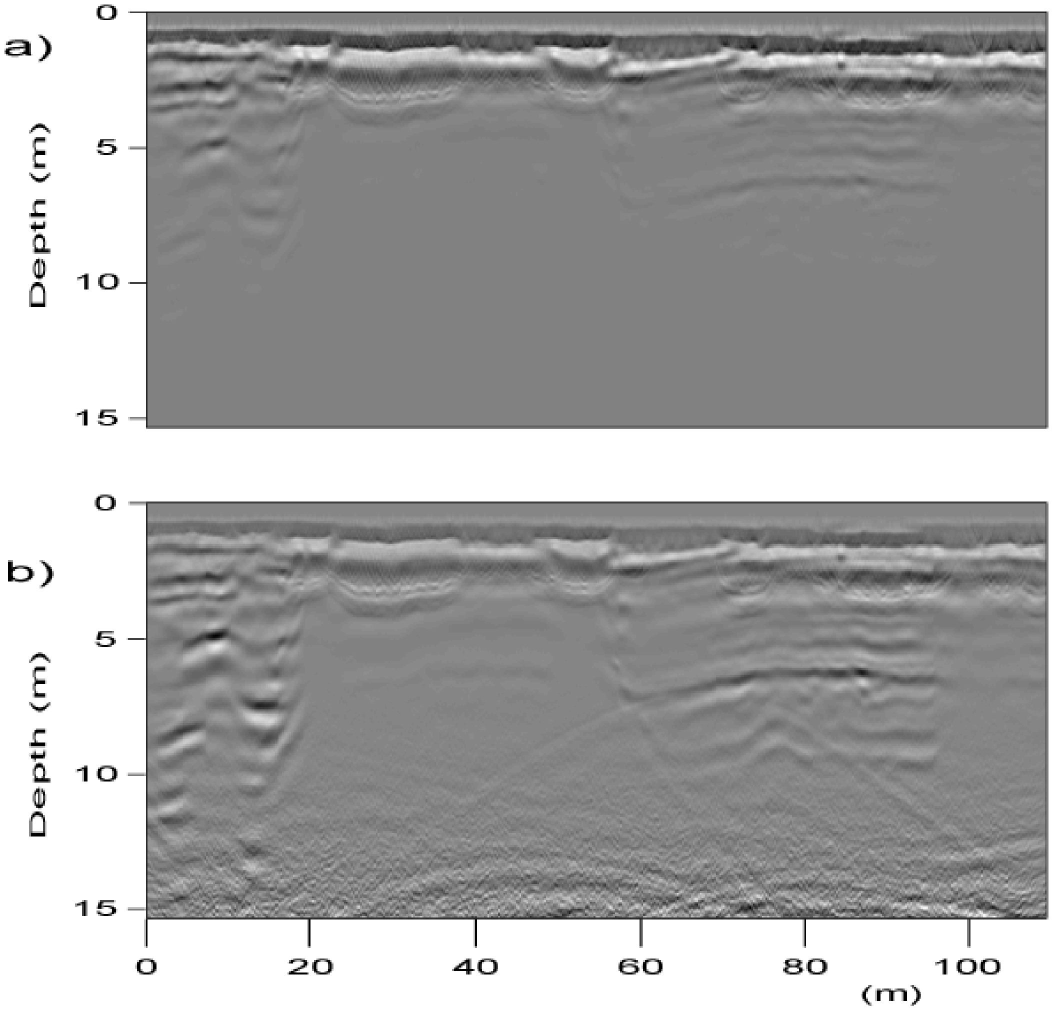

Figure 4.20. Migration of the GPR data shown in Figure 4.17. Migrated sections obtained without taking into account (a) and by taking into account (b) the conductivity of the media. No filtering has been applied and neither AGC nor clipping has been used to plot these sections. Notice the overall improvement of the image and recovering of the reflectivity values in (b). The diffractions (wide hyperbolas) on the middle and bottom of the section (pointed by arrows in Figure 4.21(a)) correspond to scatterers on the surface. The amplification of these diffractions, as well as the noise present in the data, reduces the quality of the image in the deeper part of the section.

To compare the migrated (and unmigrated) sections as they might be displayed for interpretation, I plot in Figure 4.21 the sections of Figure 4.18, 4.20(a) and 4.20(b) with AGC applied. However, no frequency filtering was used so that we can compare the final resolution of the sections. The first point to be noticed is that migration of these data definitely improves its interpretation because of the complex structures that are present in this area. Another important observation is that, even though both the migrated sections appear very similar when an AGC is applied, we can notice some areas (indicated by ellipses) where the resolution of the section has been slightly improved by including the conductivity of the media in the migration process. Therefore, including the dispersion and attenuation effects in the migration process produced an overall improvement of the resulting image and allowed us to better recover the reflectivity.

The diffractions coming from scatterers on the surface are an important drawback of the GPR technique (shielded antennas can reduce these unwanted signals). Their presence, as well as that of noise, is noticed in all the sections when an AGC filter is applied (see arrows). These unwanted signals significantly affect the reflectivity data that can be recovered by compensating the attenuation and dispersion during migration (Figure 4.20(b)). This noise has been amplified to an appreciable level only at the bottom of the section. Therefore, the deterioration of the reflectivity data due to its presence is only important in a very small part of the section, allowing a better quantitative interpretation of the reflectivity data in

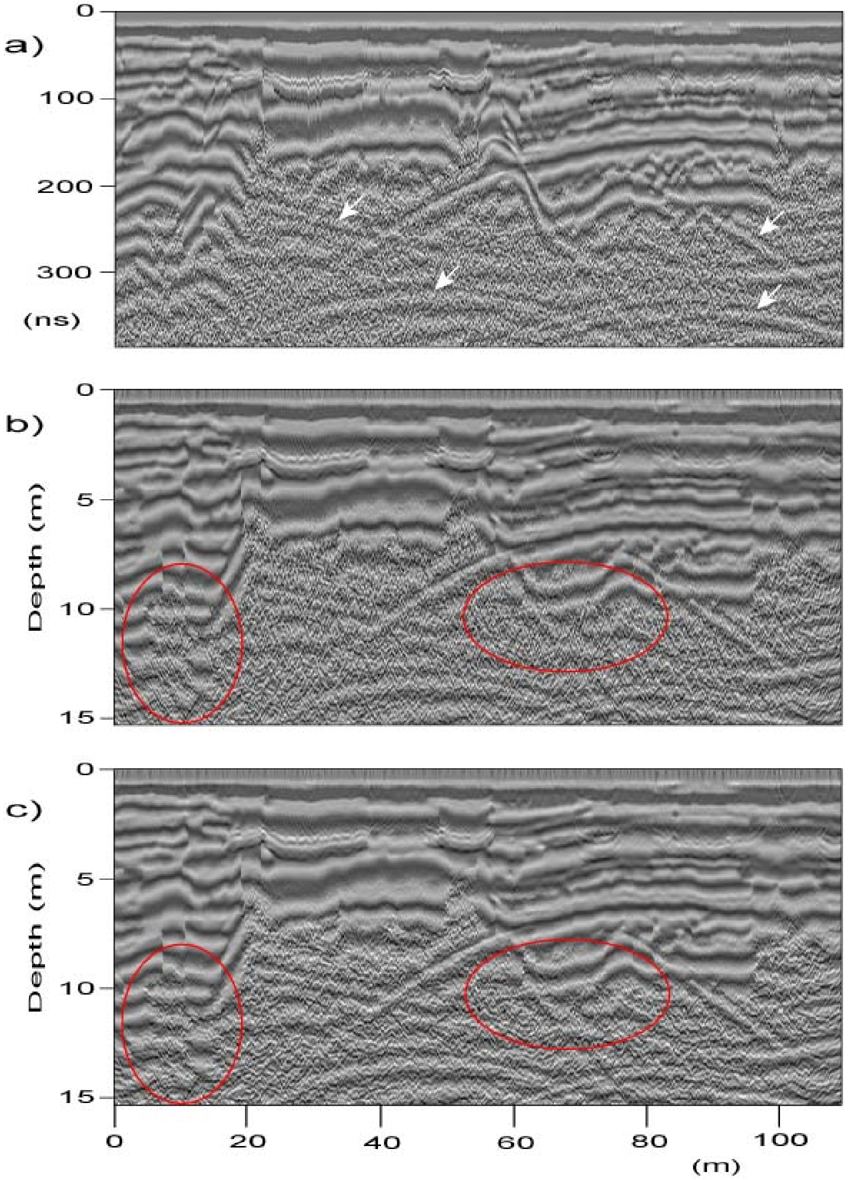

Figure 4.21. Unmigrated and migrated sections with AGC applied; (a) corresponds to Figure 4.17; (b) and (c) correspond to Figures 4.20(a) and 4.20(b), respectively. The arrows indicate diffractions generated from scatterers on the surface. The ellipses indicate two areas where higher resolution of the migrated section is observed in Figure (c) respect to (b). The length of the AGC window is 16 ns in (a), and 0.68 m in (b) and (c).

the shallower parts of the section. This is very important since the reflectivity data is related to the electromagnetic properties of the scatterers and help us to identify their nature during interpretation or even through the application of inversion techniques.

To observe the improvement in the frequency content of the resulting image by taking into account the effects of the conductivity during migration, I have computed the mean frequency of the migrated signal using a short Fourier analysis technique with a Hamming window. The window is moved along each trace and the power spectrum of the sampled window is obtained (using an FFT). Then, the mean frequency of the spectrum is computed and the value is assigned to the position (in the trace) that is at the center of the window. The mean frequency value computed in this way could be considered as a semi-instantaneous attribute. Figure 4.22 shows the mean frequency obtained for the sections presented in Figure 4.20. Even though the differences between these two plots are subtle, they can be identified if we observe the plots in detail (most of these differences can be identified by comparing the areas indicated by circles). For example, a better focusing (collapsing) of the peaks in both the vertical and horizontal directions, indicating that a better focusing of the reflections (in the real data) has been achieved. Other features that can be observed (see the area indicated by the left circle) are the improved contrast between the zones of lower and higher mean frequencies, the reallocation of some mean frequency peaks

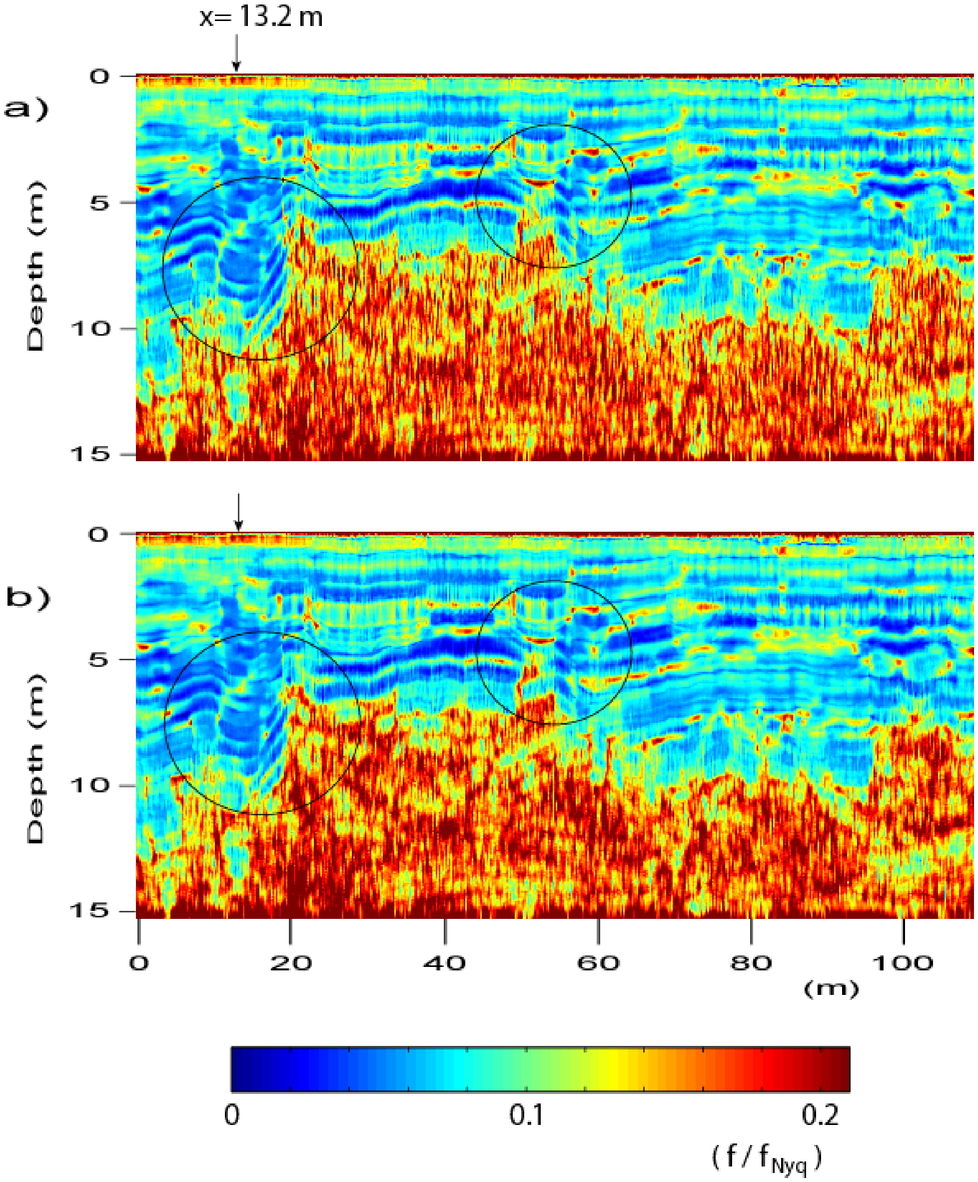

Figure 4.22. Semi-instantaneous mean frequency of the migrated sections shown in Figure 4.20. (a) and (b) corresponds to the cases (a) and (b) of Figure 4.20. The circles point out some areas where the differences between both plots are representative. The arrows point out the location of the trace whose frequency spectrum is shown in Figure 4.23. See main text for details and analysis of these plots.

improving the definition of the reflectors (see upper right area of the left circle) and the increase of the mean frequency in some areas. Even though the noise present in the bottom of the section looks similar on both the plots, the low frequency areas appear more clear in Figure 4.22 (b) than in Figure 4.22 (a), which means that the introduction of the conductivity in the migration algorithm not only amplifies the lower frequency components of the data but also compensate for the dispersion effect associated with the conductivity, which is more important for the low frequency components of the radar signal, improving the focusing of the signal, and therefore, contributing to the increase in the effective depth of penetration of the technique.

In order to compare the changes generated in the frequency content, Figure 4.23 shows the semi-instantaneous power spectrum for a given trace (located at x=13.2 m). Some important features can be observed in this figure. First, there is an increase of the amplitude of the power spectrum with depth (associated to the amplitude recovery of the signal); second, the higher frequency components of the signal have also been amplified and, for depths greater than 9 m (approximately), the shape of the spectrum at some particular depths (see arrows) is effectively changed by the increase of the higher frequency components.

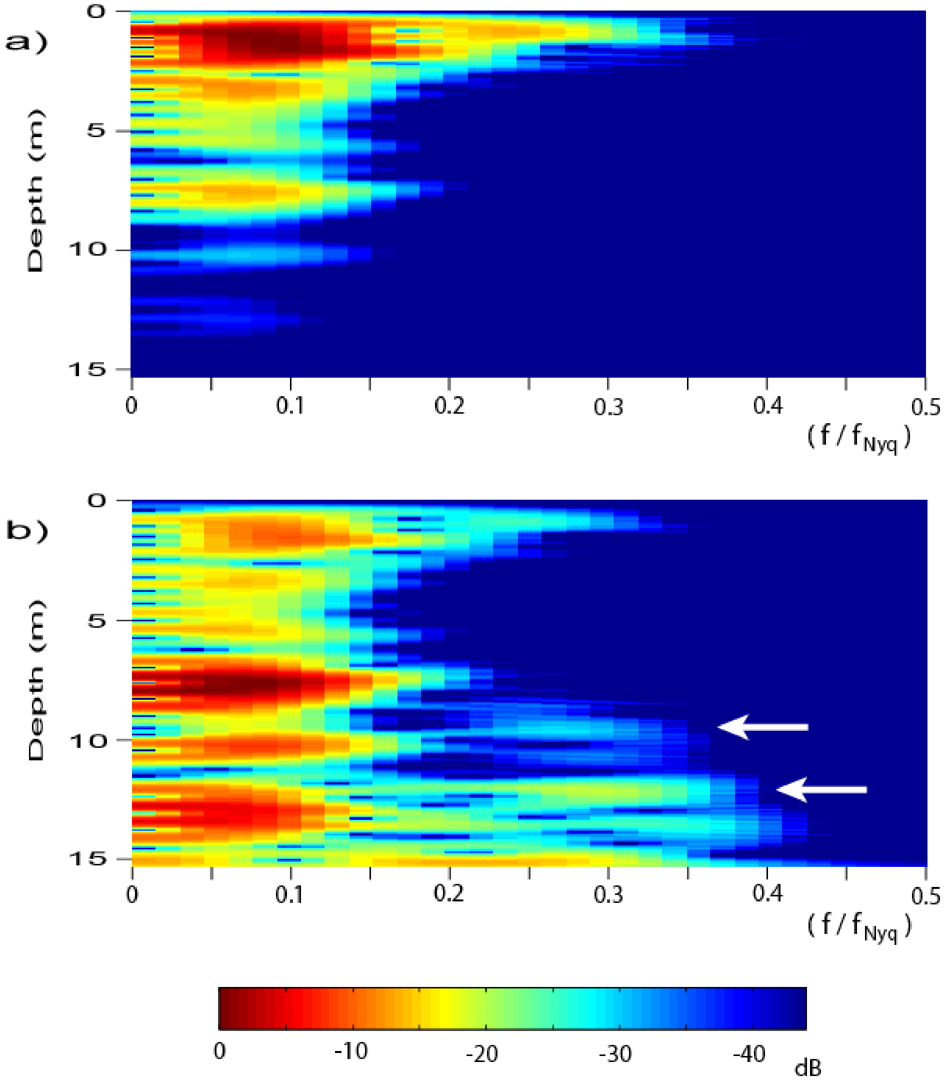

Figure 4.23. Power spectrum for the trace located at x=13.2 m (see Figure 4.22). (a) and (b) corresponds to the cases (a) and (b) in Figure 4.20. Notice the power recovery of the signal with depth and the differential increase of the frequency components (for example, at the depths indicated by arrows).

4.4 MIGRATION RESULTS IN HETEROGENEOUS AND DIELECTRICALLY DISPERSIVE MEDIA

In this section, I present a synthetic example of migration in media with dielectric absorption, and therefore, dispersion. The data generated and shown in chapter 2, for media with dielectric absorption, are used in this section. Figure 4.24(a) shows the model with one of the medium having dielectric absorption, and Figure 4.24(b) shows the corresponding zero offset section generated with this model (see Chapter 2, Figure 2.15, for an explanation on the generation of these data).

Figure 4.25(a) shows the migrated sections obtained when the conductivity and dispersion of the media are not taken into account, whereas Figure 4.25(b) shows the resulting migration when the conductivity and dispersion of the media are taken into account. In both the cases, the lateral variations of the model have been taken into account. Notice how the resolution, amplitude and position of the reflector are improved by introducing the attenuation and dispersion effects of the media. For example, the deepest reflections on the left side of the profile are clearly separated when the dispersion of the media is taken into account, also the intensity of the reflections have been correctly recovered and their position have been corrected (moved upward). Therefore, including the dispersion, attenuation and lateral heterogeneities of the media can considerably improve the quantitative and qualitative characteristic of the final migrated section.

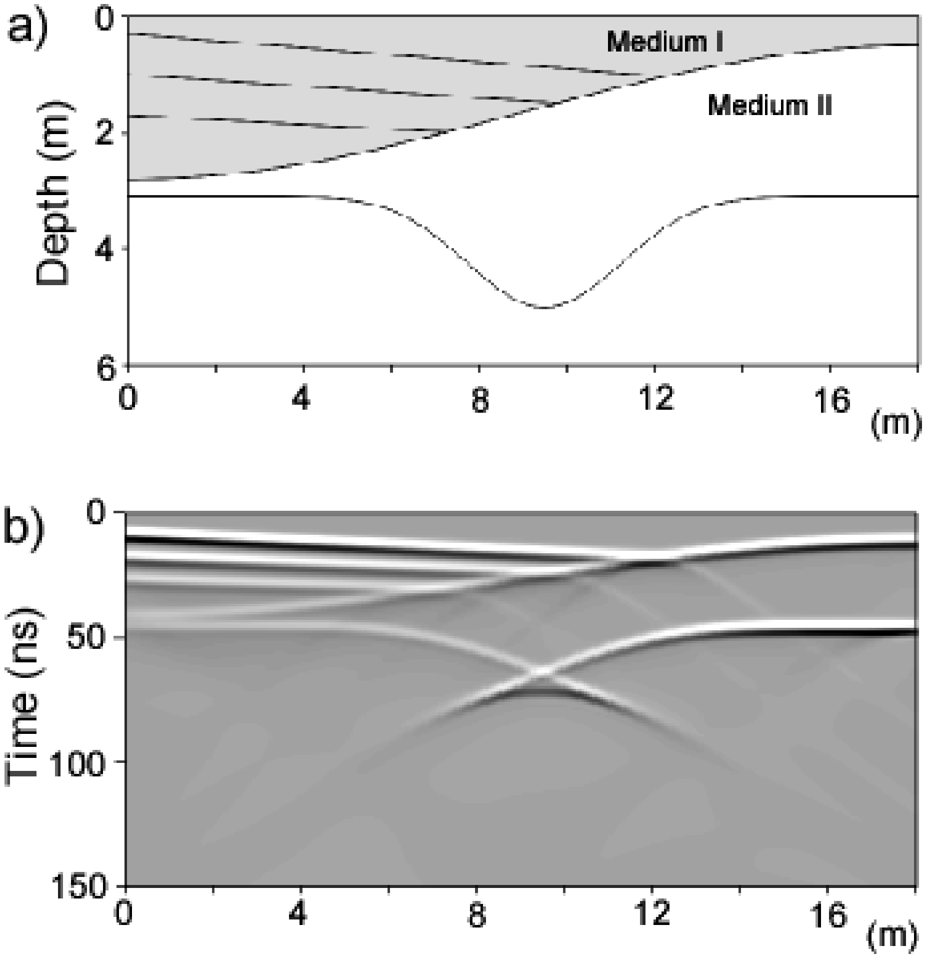

Figure 4.24. (a) Subsurface model used to generate the synthetic data. (b) Zero offset section generated with the model presented in (a).

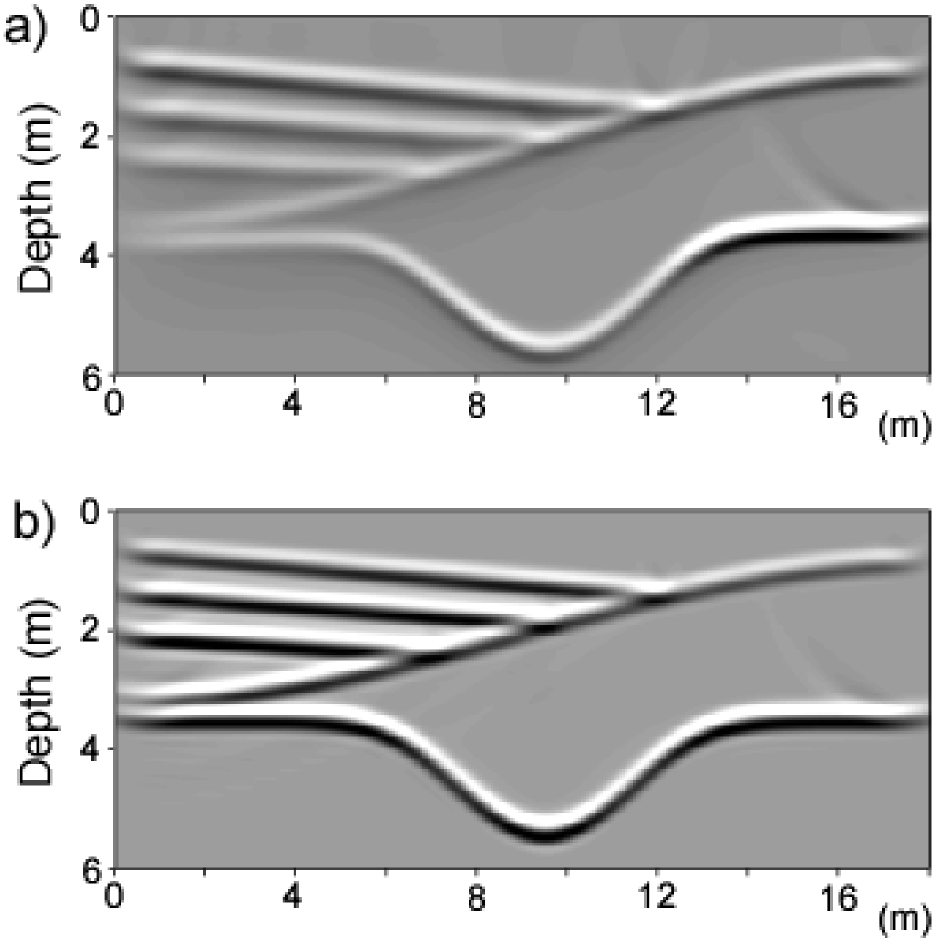

Figure 4.25. Migration of the synthetic data shown in the Figure 4.24(b). (a) Without taking into account the dispersion and conductivity effects in the medium I (see Figure 4.24(a)). (b) Taking into accounts those effects; note the overall improvement of the image, and the correct amplitude and location of the reflectors.

Figure 4.26 show the semi-instantaneous mean frequency (see last section for an explanation of this attribute) of the radar sections presented in Figure 4.25. An important feature to notice in this figure is the high frequency observed at the onset of the signal in both the Figures 4.26 (a) and (b). This high frequency is also observed at the termination of the reflections in Figure 4.26 (b) but not in Figure 4.26 (a), indicating that the reflections has a well defined end in radar section obtained by taking into account the dispersion effects. Another interesting feature is observed in the area within the circle where there is a higher frequency content of the signal, indicating an improvement of resolution in that location. These figures indicate that not only the amplitude has been recovered, but also the frequency content and therefore, the resolution of the resulting image is increased when the dispersion effects are taking into account during migration of the GPR data.

Finally, to show the effects produced on the power spectrum of the signal, Figure 4.27 shows the semi-instantaneous power spectrum for a trace located at x= 1.82 m (see Figure 4.26). These plots show clearly that taking into account the dispersion (absorptions) in the media not only recovers the correct amplitude of the reflections, but also produces an increase in the high frequency components (compare the spectrums in Figures 4.27 (a) and (b) at the depths z= 2 m or z=3 m, for example). Another feature interesting is the definition of termination of the reflection obtained in Figure 4.27 (b) where no tail (low frequency energy components) is observed after a depth of approximately 3.5 m.

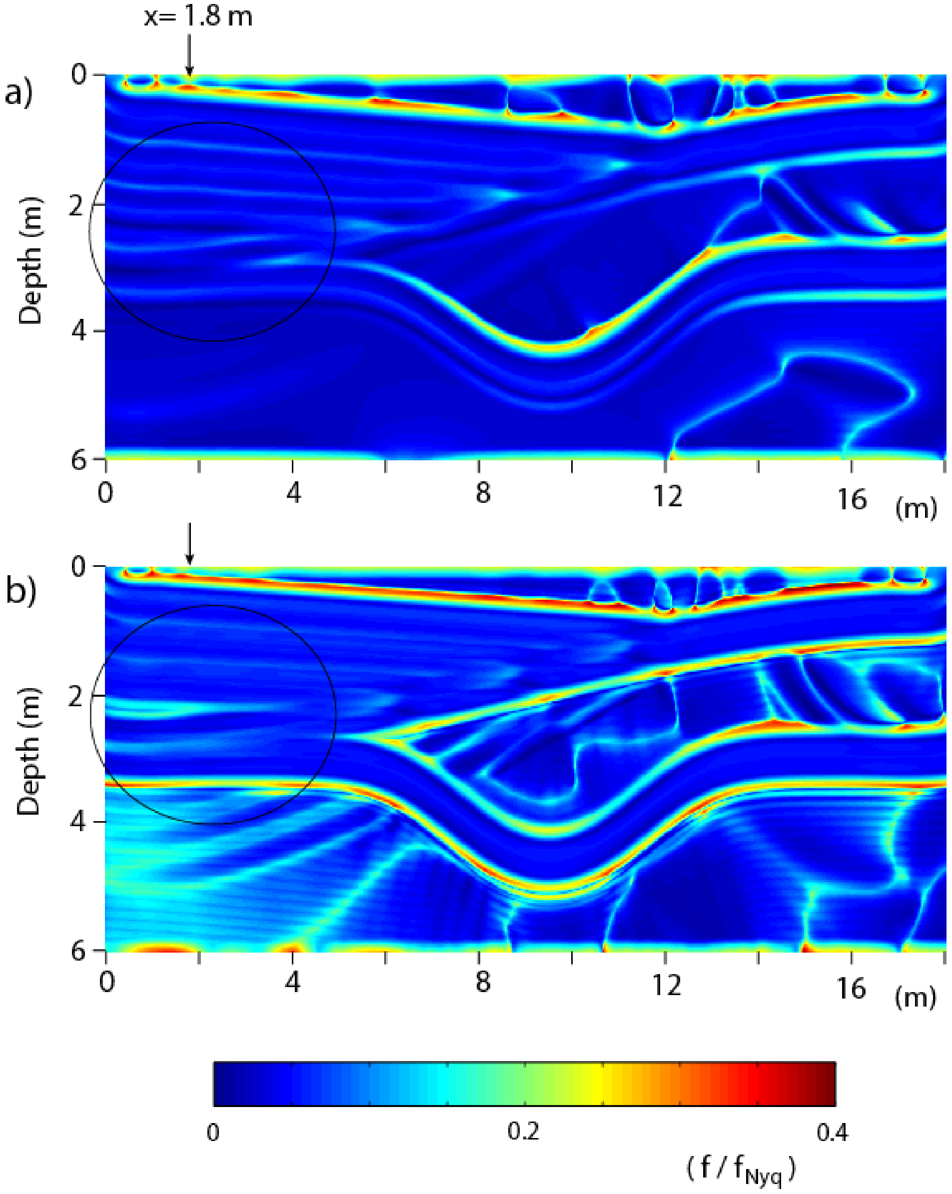

Figure 4.26. Semi-instantaneous mean frequency of the radar sections presented in Figure 4.25. Notice the higher frequency content of the radar section obtained by taking into account the dispersion effects during migration (in (b)). The noise-like signals and multiples have very small amplitudes in the migrated sections (see Figure 4.25), and therefore, are not relevant for this comparison.

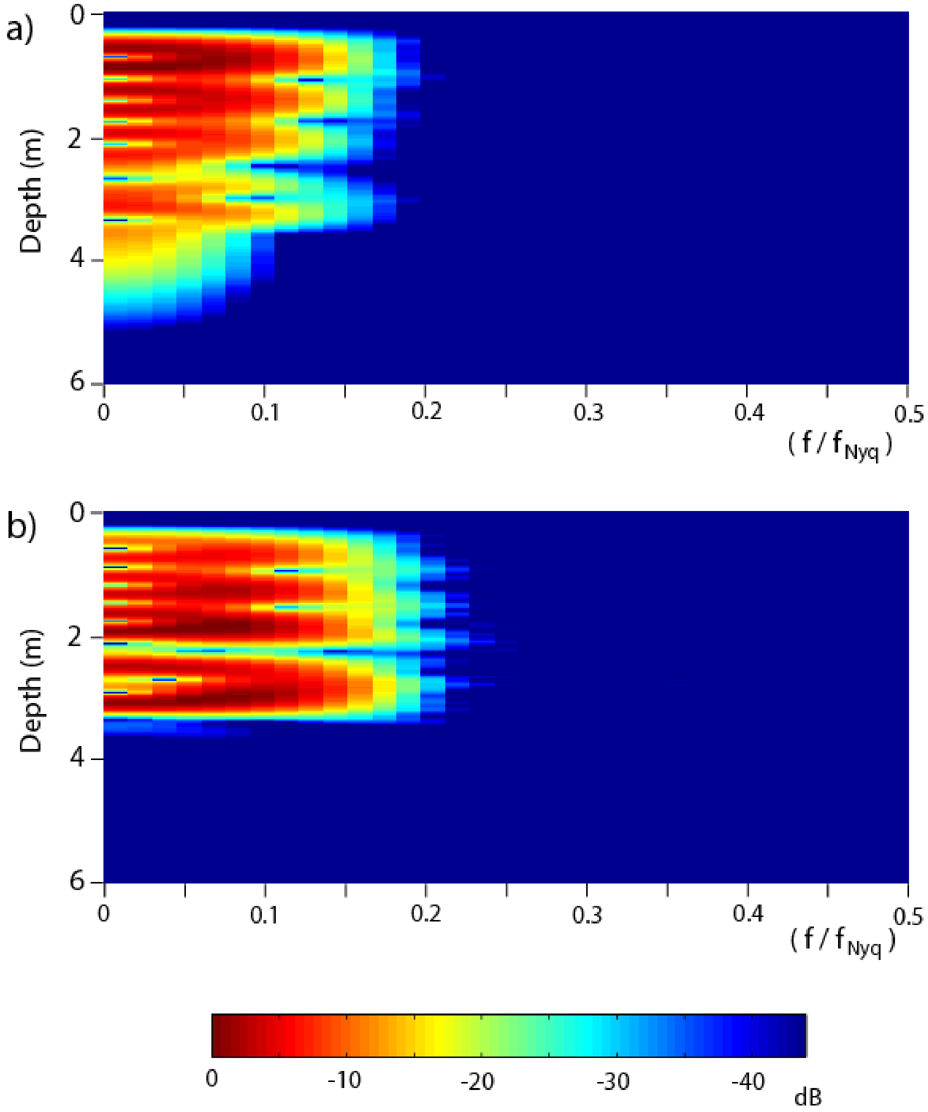

Figure 4.27. Power spectrum for the trace located at x=1.8 m (see Figure 4.26). (a) and (b) corresponds to the cases (a) and (b) in Figure 4.25. Notice the differences in the power spectrums. In particular, how the long tail related to the last reflection (see (a)) is collapsed vertically by taking into account the dispersion effects during migration (see (b)).

4.5 SUMMARY

I have shown how the split step Fourier migration technique can be applied directly for migration of GPR in 2D media and presented the basis for the extension of the technique to 3D media. In the latter case, I have shown that multi-component GPR data is necessary to account for the lateral variations, allowing the change of direction of the electric field when the direction of propagation changes. The terms that give us these corrections depend, at least, of the first order derivatives in the horizontal directions of the property of the media. If these derivatives are ignored, the components of the field are decoupled and each component can be migrated independently (using an analogous scheme to that employed for TE mode in 2D media).

An important aspect of the split step Fourier technique is that it naturally incorporates the effects of dispersion and attenuation in the migration algorithm because the phase shift operator and the phase corrector operator are both applied in the frequency domain. I have shown, using synthetic and real data, that for low to intermediate conductive or dispersive media, the incorporation of the attenuation and dispersion effects in the migration algorithm can effectively improve the quality of the resulting image and restore the correct reflectivity data. The reasonable approximation of homogeneous waves allows the migration algorithm to be stable even for extrapolation through depths greater than two or three times the characteristic skin depth of the media computed at the dominant frequency of the radar signal.

For highly lossy media, I have proposed and tested two modifications of the migration algorithm that limit the gain applied during the wave field extrapolation. The first modification, which allows the gain to be applied in both the frequency-wave number and frequency-space domains, is more stable and does not deteriorate the final image and reflectivity data. Furthermore, the results obtained with this modification converge continuously to both extremes: when no gain is allowed (total gain equal to 1) and when no limiting gain is specified (original algorithm). This modification improves the stability of the migration algorithm when small zones of very high conductivity are present in the media. The second modification of the algorithm, which allows the gain to be applied only in the frequency-space domain (equivalent to a gain applied locally in space but only in the vertical direction), was shown to be unstable, deteriorates the quality of the final image, and does not converge to the result obtained with the original algorithm when no limitation to the gain is specified. This means that a simple gain applied in the vertical direction cannot correctly compensate for the effects produced by attenuation and dispersion.

I also have presented an example that shows how the new migration technique can, without any additional modification, take into account the effects of dielectric dispersion in the media. Dispersion effects due to magnetic absorption and variation of the conductivity with frequency can similarly be taken into account (even though these dispersion effects are not common in geologic media) by the new migration technique.

Finally, we have seen that diffractions coming from scatterers on the surface represent an important drawback of the GPR technique. Shielding the antennas is a possible solution. However, for low frequency GPR antennas (10 to 100 MHz) that solution is not practical since it makes the antennas too heavy, therefore reducing the efficiency of data acquisition. Therefore, other solutions must be developed to eliminate or reduce these diffractions. In Chapter 5, I propose two possible techniques to accomplish this objective, and therefore, improve the quality of the final GPR image.

Chapter 5: Summary and future work

5.1 SUMMARY

Two main aspects associated with the Ground Penetrating Radar (GPR) technique have been addressed in this dissertation: modeling (forward problem) and imaging (reflectivity inverse problem).

For the first problem, I have developed a modeling technique for stratified media based on the invariant embedding formalism and Kennett's (1983) technique analogous to modeling elastic waves in stratified media. I adapted Kennett's seismic modeling approach to model electromagnetic waves in layered media and obtained a very fast, accurate, and unconditionally stable GPR modeling technique. This method has the capability to model all the waves that are observed in GPR data, i.e., the so called direct air waves, direct "ground waves", reflected waves, reverberations, air waves refracted into the ground, and ground waves refracted into the air. Comparison with the results obtained with a finite difference time domain (FDTD) modeling technique confirms that the reflectivity modeling technique, which is based on the plane wave decomposition of the wave field, is a far field approximation that is very accurate in this region. The results obtained for the radiation pattern generated in the subsurface when the antenna is placed very close to the air-soil interface are in agreement with previous analytical results that are also based on the plane wave approximation, but show a small difference with the results obtained with the FDTD technique.

Real GPR data were used to verify the capabilities of the reflectivity technique to generate synthetic response that matches the real data. In this regard, I have observed that for the specific real data set used, good agreement (amplitude, phase and velocity) was obtained for the reflections produced from the subsurface, except for a small difference in the amplitude of the reflection at intermediate offsets. This difference is in part expected from the fact that the reflectivity technique is a far field approximation (producing slightly greater amplitudes at intermediate offsets, which correspond to the critical angle in the soil) This also could be due to additional factors (in the real system) that are not considered in the modeling technique such as lateral heterogeneities in the subsurface, or effects produced by the vegetation or the soil roughness. Nevertheless, the comparison shows that for a stratified medium the reflections observed in the radargram can be simulated with the reflectivity technique, and the electromagnetic properties of the subsurface, obtained by matching the synthetic and real radargrams (dynamics response), will in general be different and more accurate than those obtained by a simple velocity analysis (kinematics response). I have also noticed that the conductivity of the media is constrained by the attenuation characteristic of the radargram and phase of the reflections. This indicates that a successful inversion of the permittivity and conductivity of a stratified media is possible by using the reflectivity technique as a forward modeling tool.

Even though the developed reflectivity technique is shown to be very fast, stable and accurate, it is only valid for layered media. Therefore, we still need other techniques to model GPR data in laterally heterogeneous media. With this in mind, I have implemented an explicit finite difference time domain (FDTD) technique for modeling GPR data in 2D and 3D media. Dispersion and anisotropy have also been incorporated in the modeling technique, and a description of the most common dispersion mechanisms in geologic media as well as its representation (insertion) in the finite difference scheme has been presented from a physical point of view, i.e., beginning with the general representation of the dispersion mechanisms (through the so called constitutive relations) and reducing them to simpler expressions that can describe most geologic media. I have presented and discussed several synthetic examples obtained with the FDTD technique. In particular, the results obtained for the radiation pattern of the antenna in the air-soil interface allow us to understand the origin and interaction between the different waves that are generated. This has been particularly interesting because in the reviewed literature on this topic the origin of such effects have not been pointed out or commented on, as for example, the origin of the increase (in the H plane) or decrease (in the E plane) of the intensity of the ground wave at the critical angle. Another interesting point observed in these examples are the effects that anisotropy can produce on the reflections at an interface. Even though such strong anisotropy (of electromagnetic parameters) is not commonly observed in geologic media (bulk rocks), it is important to understand that such effects could be present and, if the quality of the real data is improved, it could be possible to obtain the anisotropy parameters for such reflector media or scatterers.

Finally, in relation to the reflectivity inverse problem (so called imaging or migration), I have developed a new migration technique for heterogeneous, dispersive, and lossy media. The new GPR imaging technique is based on the Split step migration technique (well known in the seismic literature), because it takes into account (first order approximation) the lateral variation in the media as well as the refraction and diffraction effects during propagation since it is a wave equation migration technique (in fact, a one-way wave equation migration technique since no interactions between up-going and down-going waves are considered). The Split step Fourier migration is ideal in taking into account the effects of dispersion and attenuation during migration because the technique is completely implemented in the frequency domain, allowing me to directly introduce the frequency dependence of the electromagnetic parameters in the slowness equation. Compensation of the attenuation produced by Joule's effect, dielectric, or magnetic absorption is taken into account by the complex part of the vertical slowness. However, if the losses in the media are too high (i.e., so that the equivalent skin depth in the media, computed at the dominant frequency of the GPR signal, is smaller than the desired depth of migration) the technique becomes unstable. To circumvent this problem, I have proposed and developed an approximation of homogeneous plane waves that introduces greater stability to the migration technique. Migration of synthetic and real data indicate that the new migration technique is stable for depths of migration up to three times the equivalent skin depth of the medium, and that taking into account the dispersion and attenuation effects effectively allows us to recover the correct amplitude of the reflections, improve their location, shape and continuity, and increase the resolution of the final image.

5.2 FUTURE WORK

A first and direct application of the new reflectivity technique is its utilization as a forward modeling solver for an iterative or stochastic inversion technique to estimate electromagnetic properties of the subsurface. The comparison between real and synthetic data generated with the reflectivity technique not only indicates the feasibility of its used in such inversion techniques, but also that the constraints in the conductivity should be good enough to obtain the simultaneous inversion of the electric permittivity and conductivity of the media. The magnetic permeability could also be considered for inversion. However, for most geologic materials, its value is essentially constant and unaffected by environmental changes, as contrarily happens with the electric permittivity and conductivity which are strongly affected by environmental variables.

In this dissertation, the developed GPR migration technique has been implemented only for 2D media, but the theory and guidelines for its extension to 3D media have been presented. The follow up work is to implement the migration technique in 3D media. Initially, synthetic data can be used to test the capabilities of the technique. Then, its application on real data must be tested. We must remember that for a true 3D GPR migration, at least the two horizontal components of the electric or magnetic field must be recorded.

An interesting aspect to consider in GPR data processing is the elimination of the diffractions coming from scatterers that are on the surface. Such elimination will be especially important for low frequency GPR surveys for which shielded antennas are impractical. Two possibilities could be considered. The first one is entirely based on processing and does not require extra data or acquisition instruments. It consists of predicting the position of the scatterers that are on the surface by migrating the data using the air velocity. Then we can estimate (in an optimal sense) the response of such scatterer and subtract it from the real data. The second possibility is to obtain the response of the scatterers (located on the surface) by using a dual frequency GPR instrument: a high frequency signal (with almost no penetration in the subsurface) will be used to record the signal diffracted from objects on the surface, then a filtering process can convert the "wavelet" of the high frequency radar to the "wavelet" of the low frequency radar and finally both radargrams can be subtracted (notice that this technique is based on the supposition that the RCS of the scatterers on the surface do not change appreciably with frequency). The second option will probably have a higher effectiveness but will require the extra cost of recording twice the amount of data, spending more time and energy during acquisition, and will increase the cost of the equipment. For these reasons it is important to first explore the effectiveness of the former technique.

One of the most interesting aspects of developing the reflectivity technique for GPR modeling is the possibility to combine it with the Split step Fourier technique in order to obtain a fast GPR modeling technique for smoothly laterally varying media. The method will be similar to one that has been in development for elastic waves, and is based on the so called complex screen method. Such development is very important because lateral variations of the electromagnetic properties in the shallow subsurface are very common and, in such cases, the reflectivity technique, which is very fast and efficient, will not work correctly, and the finite difference techniques (more accurate for such media) are still too inefficient to be routinely used.

Finally, an experiment to study the waves generated by the antenna when it is placed on the air-soil interface should be carried out in a test site with controlled and known subsurface properties in order to obtain a better comparison between real GPR data and the results obtained with the reflectivity and FDTD modeling techniques.

Appendices

APPENDIX A

Reflection and transmission matrices at an interface

The field vector "$\underline{b}$" must be continuous in any place where no free charges or current densities are present, even if such a region is the interface between two different media. Therefore, at such an interface the continuity of $\underline{b}$ implies:

$$\underline{b}(z^{+}) = \underline{b}(z^{-}) \tag{A-1}$$

where "z^{+}" and "z^{-}" denote the vertical position just below and above of the interface, respectively.

The above equation can be written as (see Chapter 3 for the definition of the eigenvector matrix "$\underline{\underline{L}}$"):

$$\underline{w}(z^{+}) = \underline{\underline{L}}^{-1}(z^{+})\underline{\underline{L}}(z^{-})\underline{w}(z^{-}) \tag{A-2}$$

and using the definition of $\underline{\underline{L}}$ the above expression can be written as,

$$\underline{\underline{Q}}(z^{+}, z^{-}) = \underline{\underline{L}}^{-1}(z^{+})\underline{\underline{L}}(z^{-}) = \frac{1}{2}\begin{bmatrix} \underline{\underline{a}} & \underline{\underline{d}} \\ \underline{\underline{d}} & \underline{\underline{a}} \end{bmatrix} \tag{A-3}$$

where

$$\underline{\underline{a}} = \underline{\underline{G}} + \underline{\underline{F}} \qquad \text{and} \qquad \underline{\underline{d}} = \underline{\underline{G}} - \underline{\underline{F}} \tag{A-4}$$

with

$$\underline{\underline{G}} = \frac{\lambda_0(z^-)}{\lambda_0(z^+)} \begin{bmatrix} 1 & 0 \\ 0 & 1 \end{bmatrix}, \tag{A-5}$$

$$\underline{\underline{F}} = \frac{1}{\mu(z^-)\gamma(z^+)\lambda_0^{\,2}(z^+)} \begin{bmatrix} \eta_x & -m \\ -m & \eta_y \end{bmatrix}_{(z^+)} \begin{bmatrix} \eta_y & m \\ m & \eta_x \end{bmatrix}_{(z^-)}, \tag{A-6}$$

and $\quad \eta_x = \gamma\mu - P_x^{\,2}, \qquad \eta_y = \gamma\mu - P_y^{\,2}, \qquad$ and $\qquad m = P_x P_y$.

In the above expressions λ_0 is the vertical slowness, γ the complex electric permittivity and μ the magnetic permeability. P_x and P_y are the horizontal components of the slowness.

Recalling that,

$$\underline{\underline{Q}}(z^+, z^-) = \begin{bmatrix} \underline{\underline{T}}_U^{\,-1} & -\underline{\underline{T}}_U^{\,-1}\underline{\underline{R}}_D \\ \underline{\underline{R}}_U\underline{\underline{T}}_U^{\,-1} & \underline{\underline{T}}_D - \underline{\underline{R}}_U\underline{\underline{T}}_U^{\,-1}\underline{\underline{R}}_D \end{bmatrix}_{(z^+, z^-)}, \tag{A-7}$$

then,

$$\underline{\underline{T}}_U = 2\ \underline{\underline{a}}^{-1}, \qquad \underline{\underline{R}}_U = \underline{\underline{d}}\,\underline{\underline{a}}^{-1},$$

$$\underline{\underline{T}}_D = \frac{1}{2}\left(\underline{\underline{a}} - \underline{\underline{d}}\,\underline{\underline{a}}^{-1}\underline{\underline{d}}\right), \qquad \text{and} \qquad \underline{\underline{R}}_D = -\underline{\underline{a}}^{-1}\underline{\underline{d}}\ . \tag{A-8}$$

Decomposition in up-going and down-going waves

To have a physical interpretation of how the eigenvector matrix $\underline{\underline{L}}$ decomposes the wave field $\underline{b}$ in up-going and down-going waves, I suppose without loss of generality (due to the azimuthally symmetry of the layered system) that the plane of incidence is parallel to the “zx” plane (this means that $P_y = 0$). Using this condition and the definition of the eigenvector matrix $\underline{\underline{L}}$ (Chapter 3, pages 7 and 8), we obtain,

$$\underline{w} = \frac{1}{\sqrt{2}.\lambda_0}\begin{pmatrix} E_x - \dfrac{\lambda_0}{\gamma}.H_y \\ E_y + \dfrac{\mu}{\lambda_0}.H_x \\ E_x + \dfrac{\lambda_0}{\gamma}.H_y \\ E_y - \dfrac{\mu}{\lambda_0}.H_x \end{pmatrix} \tag{A-9}$$

where all the quantities are evaluated at a common depth “z”.

For simplicity, let's suppose that the media is non lossy and that the plane waves are homogeneous. Then, for the up-going waves, the components of the magnetic field are given by,

$$H_{x\,up} = \sqrt{\frac{\gamma}{\mu}} E_{y\,up} . \cos\theta \qquad \text{and} \qquad H_{y\,up} = -\sqrt{\frac{\gamma}{\mu}} . \frac{E_{x\,up}}{\cos\theta}$$

where "θ" is the angle of incidence with the "z" axis. Analogously, for the down-going waves:

$$H_{x\,dw} = -\sqrt{\frac{\gamma}{\mu}} E_{y\,dw} . \cos\theta \qquad \text{and} \qquad H_{y\,dw} = \sqrt{\frac{\gamma}{\mu}} . \frac{E_{x\,dw}}{\cos\theta}$$

The angle "θ" is the shorter angle with respect to the "z" axis, and is the same for up-going and down-going waves because they have the same horizontal slowness P_x. Using these expressions and recalling that,

$$H_i = H_{i\,up} + H_{i\,dw},$$

$$E_i = E_{i\,up} + E_{i\,dw}$$

and $\lambda_0 = \frac{1}{\sqrt{\mu\gamma}} \sqrt{\eta_x . \eta_y - m^2}$

reduces to $\lambda_0 = \sqrt{\eta_x} = \sqrt{\mu\gamma} . \cos\theta$ when $P_y = 0$,

the equation A-9 become,

$$\underline{w} = \frac{\sqrt{2}}{\lambda_0} \begin{pmatrix} E_{xup} \\ E_{y_{up}} \\ E_{xdw} \\ E_{y_{dw}} \end{pmatrix} = \begin{pmatrix} \underline{u}_p \\ \underline{d}_w \end{pmatrix} \tag{A-10}$$

which shows that the resulting wave vector $\underline{w}$ is composed by two separated vectors whose components are proportional to the horizontal components of the electric field associated to up-going and down-going plane waves.

Reflectivity and classical Fresnel's equations

In this section I show how the reflection and transmission matrices associated to an interface contain the classical Fresnel's equations. Again, for simplicity, I choose the plane of incidence parallel to the "zx" plane (i.e., $P_y = 0$). Under this condition, the matrix $\underline{\underline{F}}$ (equation A-6) becomes diagonal,

$$\underline{\underline{F}} = \frac{1}{\mu(z-).\gamma(z+).\lambda_0^{\,2}(z+)} \begin{pmatrix} \left[\gamma(z+).\mu(z+) - P_x^{\,2}\right].\gamma(z-).\mu(z-) & 0 \\ 0 & \left[\gamma(z-).\mu(z-) - P_x^{\,2}\right].\gamma(z+).\mu(z+) \end{pmatrix}$$

which can be reduced further by noticing that, for $P_y = 0$ the expression of the slowness reduces to $\lambda_0 = \sqrt{\eta_x}$. In this way,

$$\underline{\underline{F}} = \frac{\lambda_0(z-)}{\lambda_0(z+)} \begin{pmatrix} \dfrac{\gamma(z-).\lambda_0(z+)}{\gamma(z+).\lambda_0(z-)} & 0 \\ 0 & \dfrac{\mu(z+).\lambda_0(z-)}{\mu(z-).\lambda_0(z+)} \end{pmatrix} = \frac{\lambda_0(z-)}{\lambda_0(z+)} \begin{pmatrix} \alpha & 0 \\ 0 & \beta \end{pmatrix}, \tag{A-11}$$

where the definition of the auxiliary variables "α" and "β" is clear.

Substituting the equations A-5 and A-11, in equation A-4, we obtain,

$$\underline{\underline{a}} = \frac{\lambda_0(z-)}{\lambda_0(z+)} \begin{pmatrix} 1+\alpha & 0 \\ 0 & 1+\beta \end{pmatrix} ,$$

and

$$\underline{\underline{d}} = \frac{\lambda_0(z-)}{\lambda_0(z+)} \begin{pmatrix} 1-\alpha & 0 \\ 0 & 1-\beta \end{pmatrix} .$$

Substituting these matrices in the equations A-8 we obtain the reflection and transmission matrices whose elements are the transmission and reflection coefficients given expressed in Fresnel's equations. For example,

$$R_U = \begin{pmatrix} \dfrac{1-\alpha}{1+\alpha} & 0 \\ 0 & \dfrac{1-\beta}{1+\beta} \end{pmatrix} = \begin{pmatrix} r_{up\,xx} & 0 \\ 0 & r_{up\,yy} \end{pmatrix} , \qquad \text{(A-12)}$$

where

$$r_{up_{yy}} = \frac{\mu(z-).\lambda_0(z+) - \mu(z+).\lambda_0(z-)}{\mu(z-).\lambda_0(z+) + \mu(z+).\lambda_0(z-)} = \frac{n_1 \cos\theta_1 - \dfrac{\mu_1}{\mu_2} n_2 \cos\theta_2}{n_1 \cos\theta_1 + \dfrac{\mu_1}{\mu_2} n_2 \cos\theta_2} = r_\perp$$

is equivalent to the reflection coefficient for a plane wave with its electric field perpendicular to the plane of incidence (in this case, the "y" direction).

APPENDIX B

Source term in the GPR reflectivity technique

In the reflectivity technique the source introduces a discontinuity of the wave field in a horizontal plane located at the level of the source. Following the description of Kennett (1983), I will obtain how the source is introduced in the reflectivity GPR modeling technique.

Figure B.1 shows a schematic picture of the problem. The vertical position of the source and the receiver are "z_S" and "z_R", respectively. The region between "z_1" and "z_2" is a stack of laterally homogeneous layers, and the regions above and below it are homogeneous media. In general, GPR is carried out on the surface, and so the source and receivers are immersed in the air. For the GPR technique, in contrast with seismic, at the surface of the earth it is not required that any component of the electromagnetic field be zero (as happens, for example, with some components of the stress tensor in the case of seismic waves), even though for non penetrating radar applications, the earth could be approximated as a perfect conductor. Therefore, for the modeling GPR data, no boundary conditions are required for the electromagnetic waves, except that of divergent waves propagating out from the source and the model.

Using the definition of the wave propagator matrix (equation 3.6) we can write the following equation that relates the wave vector at the levels just below the source and the stack of layers,

$$\underline{w}(z_2^+) = \underline{\underline{Q}}(z_2^+, z_S^+)\underline{w}(z_S^+) \ . \tag{B-1}$$

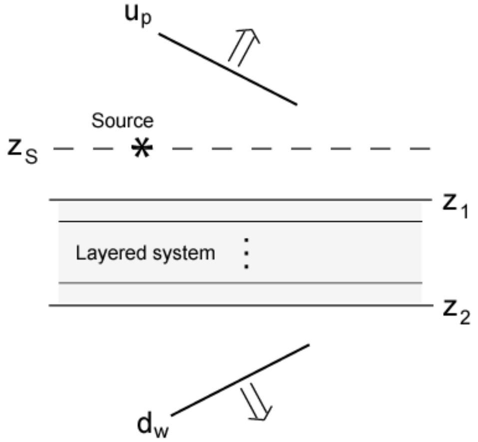

Figure B-1. Common boundary conditions in the GPR technique and applied to obtain the corresponding source term in the reflectivity technique. Above z₁ and below z₂ the media are homogeneous. The wave vector $w(z)$ is discontinuous at $z = z_S$ where the source is located. Above z_S only up-going waves exist, whereas below z_2 only down-going waves exist.

The discontinuity of the wave vector at the source position can be written as (Kennett, 1983):

$$\underline{w}(z_S^+) - \underline{w}(z_S^-) = \underline{\underline{L}}^{-1}(z_S)\underline{S}(\omega, p_x, p_y) \ , \tag{B-2}$$

where $\underline{S}$ is the plane wave representation of the source in the frequency domain and I have indicate explicitly this dependency in this equation, but I will not indicate it in the next equation (notice that all the quantities in equations B-1 and B-2 are in fact represented in these domain and therefore all they depend on this variables).

Combining B-2 and B-1 we obtain,

$$\underline{w}(z_2^+) = \underline{\underline{Q}}(z_2^+, z_S^+)\left(\underline{w}(z_S^-) + \underline{\underline{L}}^{-1}(z_S)\underline{S}\right) . \tag{B-3}$$

Now, defining

$$\underline{\underline{L}}^{-1}(z_s)\underline{S} = \begin{pmatrix} \underline{\xi}_u \\ \underline{\xi}_d \end{pmatrix} , \tag{B-4}$$

and noticing that above the source there will only be up-going waves, and below the layered system there will only be down-going waves, i.e.,

$$\underline{w}(z_S^-) = \begin{pmatrix} \underline{u}_p \\ 0 \end{pmatrix}_{Z_S^-} \quad \text{and} \quad \underline{w}(z_2^+) = \begin{pmatrix} 0 \\ \underline{d}_w \end{pmatrix}_{Z_2^+} , \tag{B-5}$$

equation B-3, after substitution of $\underline{\underline{Q}}$ by its expression as function of transmission and reflection matrices, will be reduced,

$$\begin{pmatrix} 0 \\ \underline{d}_w \end{pmatrix} = \begin{bmatrix} \underline{\underline{T}}_U^{-1} & -\underline{\underline{T}}_U^{-1}\underline{\underline{R}}_D \\ \underline{\underline{R}}_U\underline{\underline{T}}_U^{-1} & \underline{\underline{T}}_D - \underline{\underline{R}}_U\underline{\underline{T}}_U^{-1}\underline{\underline{R}}_D \end{bmatrix}_{(z_2^+, z_S^+)} \begin{pmatrix} \underline{u}_p + \underline{\xi}_u \\ \underline{\xi}_d \end{pmatrix} , \tag{B-6}$$

finally, solving this system of equations I obtain,

$$\underline{u}_p(z_S^-) = -\underline{\xi}_u + \underline{\underline{R}}_D(z_2^+, z_S^+)\underline{\xi}_d \tag{B-7}$$

and

$$\underline{d}_w(z_2^+) = \underline{\underline{T}}_D(z_2^+, z_S^+)\underline{\xi}_d \ . \tag{B-8}$$

The equation B-7 is the equation that will give us the GPR reflection response of the layered system (as a function of the source $\underline{\underline{S}}$), whereas equation B-8 will give us the transmission response. To obtain the response at a receiver plane below the source plane (i.e., it is located at $z = z_r$, with $z_r > z_S$), we can use the equations B-3, but changing z_2^+ by z_r, in this way,

$$\underline{w}(z_r) = \underline{\underline{Q}}(z_r, z_S^+)\left(\underline{w}(z_S^-) + \underline{\underline{L}}^{-1}(z_S)\underline{S}\right) \ . \tag{B-9}$$

If the receiver plane is above the layered system (i.e., $z_S < z_r < z_1$), then the wave propagator in equation B-9 is only composed by transmission matrices, i.e.,

$$\underline{\underline{Q}}(z_r, z_S^+) = \begin{pmatrix} \underline{\underline{T}}_{U_{rs}}^{-1} & 0 \\ 0 & \underline{\underline{T}}_{D_{rs}} \end{pmatrix} . \tag{B-10}$$

then, using the expression of $w(z_s^-)$ (equation B-5), the expressions for $\underline{\underline{L}}^{-1}(z_s)\underline{S}$ (equation B-4), and substituting the result of equation B-7, we obtain,

$$\underline{w}(z_r) = \begin{pmatrix} \underline{\underline{T}}_{U_{rs}}^{-1} \underline{\underline{R}}_D (z_2^+, z_s^+) \underline{\xi}_d \\ \underline{\underline{T}}_{D_{rs}} \underline{\xi}_d \end{pmatrix} . \qquad \text{(B-11)}$$

If we call $\underline{\underline{R}}_{D_S} = \underline{\underline{R}}_D (z_2^+, z_s^+)$ and use the definition of the wave vector (i.e., $\underline{w} = \underline{\underline{L}}^{-1} \underline{b}$), then we obtain the equation 3.28 presented in Chapter 3.

Notice that the reflection and transmission matrices are independent of the source term, therefore, they have to be computed only once for a given system, and can be used with different source terms. This property makes the reflectivity technique also attractive for source inversion problems in stratified media.

Tau-p response of an infinite current line

To show an example of the use of the above equations to compute a synthetic radargram using the reflectivity technique, I obtain the algebraic expressions for the electric and magnetic fields generated by a hypothetical infinite and uniform current line (this hypothetical source is the same used in the 2D FDTD modeling technique).

Let's first suppose that the current line is parallel to the "y" axis and placed below the origin at $z = z_S$. For this configuration, the current density can be written as,

$$\underline{J}(x, y, z, t) = J_0(t) G(y) \delta(z - z_S) \delta(x) \hat{y} \qquad \text{(B-12)}$$

If the current is uniform, then $G(y)=1$, which corresponds to the fundamental source type in 2D FDTD modeling technique. However, if we want to compute the response of an infinitesimal electric dipole, then $G(y) = \delta(y)$, and for a general electric dipole $G(y)$ can have any form. As I have mentioned, I will solve the case for a uniform current. In this case, the source term in the reflectivity technique will be given by (see equation 3.2 on page 76, Chapter 3),

$$\underline{S} = \left[0,0,0,J_0(\omega)\delta(z-z_S)\delta(k_y)\right]^T \ , \tag{B-13}$$

where I have used the identity $\int_{-\infty}^{\infty} e^{-ik_y y} dy \equiv \delta(k_y)$. The $\delta(z-z_s)$, which generates the discontinuity of the wave vector at $z=z_s$, is already taken into account by the equation B-2 and does not have to be included when substituting (this result) in any equation obtained from equation B-2 (as, for example, equation B-11).

Now, using the definition of $\underline{\underline{L}}$ (see page 77, Chapter 3) and substituting in equation B-4, we obtain,

$$\underline{\xi}_d = -\frac{J_0(\omega)\delta(z-z_S)\delta(k_y)}{\sqrt{2}\gamma(z_S)\lambda_0^2(z_S)}\begin{pmatrix} -P_xP_y \\ \mu(z_S)\gamma(z_S)-P_y^2 \end{pmatrix} \ . \tag{B-14}$$

Substituting this expression in equation 3.28 (Chapter 3), dropping $\delta(z-z_0)$ (as mentioned above), and using the fact that $\underline{\underline{T}}_{D_{rs}} = \underline{\underline{T}}_{U_{rs}}^{-1}$, we get,

$$\begin{pmatrix} E_x \\ E_y \end{pmatrix} = -\frac{J_0(\omega)\delta(k_y)}{2\gamma(z_S)\lambda_0^2(z_S)} \underline{\underline{L}}_1(z_s)\underline{\underline{T}}_{D_{rs}}\left(\underline{\underline{I}} + \underline{\underline{R}}_{D_s}\right)\begin{pmatrix} -P_x P_y \\ \mu(z_S)\gamma(z_S) - P_y^2 \end{pmatrix},$$

and

$$\begin{pmatrix} -H_y \\ H_x \end{pmatrix} = -\frac{J_0(\omega)\delta(k_y)}{2\gamma(z_S)\lambda_0^2(z_S)} \underline{\underline{L}}_2(z_s)\underline{\underline{T}}_{D_{rs}}\left(\underline{\underline{R}}_{D_s} - \underline{\underline{I}}\right)\begin{pmatrix} -P_x P_y \\ \mu(z_S)\gamma(z_S) - P_y^2 \end{pmatrix}. \tag{B-15}$$

Now, we must substitute $\underline{\underline{L}}_1(z_s)$ and $\underline{\underline{L}}_2(z_s)$ (see page 77, Chapter 3), and transform these expressions from the "k_y" domain to the "y" domain. In doing so, we must recall that $P_i = k_i / \omega$, use the properties of $\delta(k_y)$ and notice that for $k_y = 0$ the reflection matrix $\underline{\underline{R}}_{D_s}$ becomes diagonal (see, for example, Appendix A),

$$\underline{\underline{R}}_{D_s} = \begin{pmatrix} r_{d_{xx}} & 0 \\ 0 & r_{d_{yy}} \end{pmatrix}, \tag{B-16}$$

where $r_{d_{xx}}$ and $r_{d_{yy}}$ are the reflection coefficients for the "x" and "y" components of the electric field associated with the down-going wave field.

In this way, the final expressions for the electric and magnetic fields (in the plane wave domain (ω, P_x)) for the infinite and uniform current line are,

$$\begin{aligned} E_x &= 0 \\ E_y &= -\frac{\mu(z_s)}{2\sqrt{\mu(z_s)\gamma(z_s) - P_x^2}} e^{i\omega\sqrt{\mu(z_s)\gamma(z_s) - P_x^2}\,(z_r - z_s)}(1 + r_{d_{yy}})J_0(\omega) \\ H_y &= 0 \\ H_x &= \frac{1}{2} e^{i\omega\sqrt{\mu(z_s)\gamma(z_s) - P_x^2}\,(z_r - z_s)}(1 - r_{d_{yy}})J_0(\omega) \end{aligned}$$

The factor $(1+r_{d_{yy}})$ in the expression of E_y indicates that this component is a superposition of the direct and reflected down-going waves (as expected). The opposite sign of "$r_{d_{yy}}$" in the expression of H_x is associated to the change of direction of propagation of the reflected wave. Notice that for a lossless media (e.g., the air in GPR applications), when $P_x = \sqrt{\mu(z_s)\gamma(z_s)}$ (maximum slowness of the medium), the vertical slowness $q = \sqrt{\mu(z_s)\gamma(z_s) - P_x^2}$ becomes zero and then E_y diverges. To understand the meaning of this result, let's suppose that the layered system does not exist (i.e., $r_{d_{yy}} = 0$) and make $(z_r - z_s) \to 0$, then we expect to observe only the direct wave, which in the tau-p domain will be a strong pulse at zero lag and exactly at the maximum slowness of the media, which is the result obtained for E_y according to the above equation (it becomes equivalent to a delta function at that position). In the numerical implementation of this equation, a small imaginary part can be added to the slowness of the medium where the source is located, in order to avoid this divergence. Finally, notice that for greater values of P_x, the vertical slowness becomes purely imaginary (in lossless media) or mostly imaginary (in slightly lossy media). Therefore, these waves will decay exponentially in the medium where the source is located (supposing that $(z_r - z_s) > 0$), and have a phase shift of -90°, changing the character of the resulting wavelet (see, for example, Figure 3.13, Chapter 3).

APPENDIX C

Vertical slowness for homogeneous plane waves

In general, the complex wave number of a plane wave can be expressed as

$$\vec{k} = \vec{k}_R + i\vec{k}_I \quad , \qquad \text{(C-1)}$$

where $\vec{k}_R$ and $\vec{k}_I$ are real vectors, and i is the unit imaginary number. The vectors $\vec{k}_R$ and $\vec{k}_I$ define the directions of propagation and attenuation (or amplification) of the plane wave, respectively. The planes of constant phase and constant amplitude are perpendicular to $\vec{k}_R$ and $\vec{k}_I$, respectively. In the particular case that these two vectors are parallel, the plane wave is called "homogeneous", otherwise it is called "heterogeneous" (e.g., Chen, 1983). Therefore, for homogeneous plane waves, the direction of propagation and attenuation (or amplification) is the same and the planes of constant phase and constant amplitude are parallel.

In isotropic media, the slowness "u" is, in general, a complex number. We express the square of the slowness as,

$$w = u^2 = w_R + iw_I \quad , \qquad \text{(C-2)}$$

where w_R and w_I are real numbers and represent the real and imaginary parts of the square of the slowness.

Substituting the equations C-1 and C-2 in the dispersion relation that corresponds to plane waves in isotropic and homogeneous media, we obtain

$$\omega^2 (w_R + iw_I) = (\vec{k}_R + i\vec{k}_I) \cdot (\vec{k}_R + i\vec{k}_I) \quad , \tag{C-3}$$

where the “$\cdot$” denotes inner product.

For homogeneous plane waves, we can express $\vec{k}_I = \beta \vec{k}_R$, where β is a real number. In this way, the equation A-3 becomes

$$\omega^2 (w_R + iw_I) = (1 + i\beta)^2 \vec{k}_R \cdot \vec{k}_R \quad . \tag{C-4}$$

Equating the real and imaginary parts yields to the following equation

$$\beta^2 + 2\frac{w_R}{w_I}\beta - 1 = 0 \quad . \tag{C-5}$$

Now, the real vector $\vec{k}_R$ can be written as

$$\vec{k}_R = k_x \hat{x} + k_y \hat{y} + k_z \hat{z} \quad , \tag{C-6}$$

substituting this expression in equation C-4 yields

$$\omega^2 (w_R + iw_I) = (1 + i\beta)^2 k_x^2 + (1 + i\beta)^2 k_y^2 + (1 + i\beta)^2 k_z^2 \ . \tag{C-7}$$

In wave field Fourier extrapolation techniques, the real values k_x and k_y are the variables of the Fourier transform in the horizontal directions. We see that these variables are related to the components of the complex wave number through the factor $1 + i\beta$. On the other hand, the extrapolation of the wave field in the vertical direction depends on the “z” component of the complex wave number, i.e.,

$$k_z^{'} = (1+i\beta)k_z \quad , \tag{C-8}$$

and so, the vertical slowness is given by

$$q_z = \frac{k_z^{'}}{\omega} = \left[(w_R + iw_I) - (1+i\beta)^2 \frac{(k_x^2 + k_y^2)}{\omega^2} \right]^{1/2} \quad . \tag{C-9}$$

To obtain the final expression, we have to substitute the solution of β derived from equation A-5. Since there are two solutions, the one with the same sign as w_I has to be chosen (as required by equation C-4). Nevertheless, the final algebraic result, for equation C-9, is independent of the sign w_I (if operating accordingly). I suppose a positive sign for w_I and obtain,

$$\beta = \frac{w_R}{w_I}\left[\sqrt{1+(w_I / w_R)^2} - 1 \right] . \tag{C-10}$$

Substituting this expression in equation C-9 and simplifying,

$$q_z = \frac{k_z^{'}}{\omega} = u\left[1 - (k_x^2 + k_y^2)/a^2 \right]^{1/2} \quad , \tag{C-11}$$

where $$a = \omega w_I \Big/ \left[2w_R(\sqrt{1+(w_I / w_R)^2} - 1) \right]^{1/2} \quad .$$

The expression for a can be simplified to,

$$a = \omega \left[\frac{\sqrt{w_R^2 + w_I^2} + w_R}{2} \right]^{1/2} = \omega \operatorname{Re}(u_0),$$

which shows that ω / a is the phase velocity in the medium.

In the 2D case, we just make $k_y = 0$ and obtain the result presented in Chapter 4.

APPENDIX D

Estimation of the electric permittivity and conductivity at the cave site

In order to estimate the models of electrical permittivity and conductivity used to migrate the GPR data acquired at the cave site, we used the velocities obtained from the stacking analysis of the CMP data, Archie's law and an empirical relationship between water content in soils and their electrical permittivities (Topp, et. al., 1980).

The results obtained from the stacking velocity analysis can be considered as related to the properties of the media at the main frequency of the radar signal. We suppose that the media are non magnetic and the electric permittivity and conductivity are real and do not change in the bandwidth of the radar signal. Then, I use an iteration procedure to estimate these parameters.

The velocity of the electromagnetic waves is related to the properties of the media through the real part of the slowness, i.e.,

$$V = 1/\mathrm{Re}(u) = \frac{\sqrt{2}}{\sqrt{\mu_0 \varepsilon}} \left[1 + \sqrt{1 + (\sigma / \omega\varepsilon)^2} \right]^{-1/2} \quad , \tag{D-1}$$

where $\mu_0 = 4\pi x 10^{-7}$ H/m, ε is the electric permittivity and σ is the electric conductivity.

On the other hand, the conductivity of the media is estimated using Archie's law,

$$\sigma = a_0 \sigma_w \phi^m (S_w)^n + \sigma_c \tag{D-2}$$

where a_0 is a constant (usually between 0.5 and 2), σ_w is the conductivity of the water present into the pore spaces, ϕ is the porosity of the media, m is the cementation exponent, S_w is the water saturation into the pore spaces, n is the saturation exponent and σ_c is the grain surface conductivity.

In carbonate rocks, the saturation exponent "n" can vary appreciably, especially when different porosities are present (macro and micro-porosities) and two or more immiscible fluids (of different conductivities) are contained inside the pore spaces. However, if only water is present in the pore spaces and it has a medium saturation, the saturation exponents take values very close to 2 (Anderson, 1986). Also, the cementation exponent "m" of carbonate rocks has been observed to be very close to 2 (Carothers, 1968), thus, we assume a value equal 2 for both the exponents. We also suppose that the main contribution to the conductivity is due to the pore fluid in the media, neglecting in this way the grain surface conductivity term. Then, the Archie's law reduces to the following expression,

$$\sigma = a_0 \sigma_w (\eta_w)^2 \quad , \tag{D-3}$$

where $\eta_w = \phi S_w$ is the water content.

In order to estimated the water content, we use the following empirical relationship between water content and electric permittivity of soils (Topp et. al., 1980),

$$\eta_w = 5.3\text{x}10^{-2} + 2.92\text{x}10^{-2}(\varepsilon_r) - 5.5\text{x}10^{-4}(\varepsilon_r)^2 + 4.3\text{x}10^{-6}(\varepsilon_r)^3 \quad , \tag{D-4}$$

where $\varepsilon_r = \varepsilon / \varepsilon_0$ is the electric permittivity of the soil relative to the vacuum.

The constant $a_0 \sigma_w$ in equation D-3 is obtained by requiring that the estimated mean value of the conductivity of the media (3.5 mS/m) be obtained when the mean value of the water content in the media is substituted. The mean value of the water content is computed by using equation D-4 and an estimated mean value of the electric permittivity of the media equal to $1.1x10^{-10}$ F/m ($\varepsilon_r = 12.51$).

Now, from equation B-1 we obtain the following recursive expression for the electrical permittivity,

$$\varepsilon = \frac{2}{\mu_0 V^2}\left[1+\sqrt{1+(\sigma/\omega\varepsilon)^2}\,\right]^{-1} \quad , \qquad \text{(D-5)}$$

Using the mean values of the electrical permittivity and conductivity as initial values for this recursive equation, we compute the values of permittivity corresponding to the velocities obtained from the staking analysis. These values of permittivity are substitute in equation D-4 and the obtained values of water content are substituted in equation D-3 to compute the corresponding conductivity values. Then, these new values of permittivity and conductivity are used to begin the next iteration. The iteration process is stopped when the difference between the old and new values of conductivity and permittivity are lower than some desired error level.

References

Abeles, F., 1950. Ann. de Physique, 5, 596.

Akbar, F.E., Sen, M.K. and Stoffa, P.L., 1996. Prestack plane-wave Kirchhoff migration in laterally varying media: Geophysics, 61, No. 4, 1068-1079.

Arcone, S.A., 1995. Numerical studies of the radiation patterns of resistively loaded dipoles: J. of App. Geophysics, 33, 39-52.

Anderson, W. G., 1986. Wettability literature survey – Part 3: The effect of wettability on the electrical properties of porous media: J. Petr. Tech., 38, 1372-1378.

Baumgartner, F., Munk, J. and Daniels, J., 2001. A geometric optics model for high-frequency electromagnetic scattering from dielectric cylinders: Geophysics, 66, No. 4, 1130-1140.

Berenger, J.P., 1994. A perfectly matched layer for the absorption of electromagnetic waves: J. Comput. Phys., 114, 185-200.

Bernabini M., Pettinelli E., Pierdicca N., Piro S., Versino L., 1995. Field experiments for characterization of GPR antenna and pulse propagation: J. Appl. Geoph., 33, 63-76.

Blacic, T.M. and Arulanandan, K., 1999. Identification of contaminated soils by dielectric constant and electric conductivity: Journal of Environmental Engineering, January, 103-105.

Carcione, J.M., 1996. Ground-penetrating radar: Wave theory and numerical simulation in lossy anisotropic media: Geophysics, 61, No. 6, 1664-1677.

Carcione, J.M., 1998. Radiation pattern for 2-D GPR forward modeling: Geophysics, 63, No. 2, 424-430.

Carcione, J.M. and Schoenberg, M.A., 2000. 3-D ground penetrating radar simulation and plane wave theory in anisotropic media, Geophysics, 65, No. 5, 1527-1541.

Carlsten, S., Johansson, S. and Wörman, A., 1995. Radar techniques for indicating internal erosion in embankment dams: J. App. Geophysics, 33, No. 1-3, 143-156.

Carothers, J.W., 1968. A statistical study of the formation factor relationship: The Log Analyst (Sept-Oct) 14-20.

Chapman, C.H., 1978. A new method for computing synthetic seismograms: Geophys. J. R. astr. Soc., 66, 445-453.

Chapman, C.H., 1981. Generalized Radon transforms and slant stacks: Geophys. J. R. astr. Soc., 54, 481-518.

Chen, H.C., 1983. Theory of electromagnetic waves: a coordinate-free approach: McGraw-Hill, New York.

Chew, W.C., 1995. Waves and fields in inhomogeneous media. IEEE press.

Claerbout, J.F., 1971. Toward a unified theory of reflector mapping: Geophysics, 36, No. 3, 467-481.

Cole, K.S. and Cole, R.H., 1945. Dispersion and absorption in dielectrics: J. Chem. Phys., 9, 341-351.

Crook, 1948. The reflection and transmission of light by any system of parallel isotropic film: J. Opt. Soc. Am., 38, 954-964.

Davis, J.L. and Annan, A.P., 1989. Ground-penetrating radar for high-resolution mapping of soil and rock stratigraphy: Geophysical Prospecting, **37**, 531-551.

Davis, J.L. and Annan, A.P. and Vaughan, C.J., 1984. Placer exploration using radar and seismic methods: 54th Annual meeting, Soc. Expl. Geophysicist, Expanded Abstracts, 306-308.

Debye, P., 1929. Polar molecules: Dover, New York.

Di, Q. and Wang, M., 2004. Migration of ground-penetrating radar data with a finite-element method that considers attenuation and dispersion: Geophysics, 69, No. 2, 472-477.

Dominic, D.F., Egan, K., Carney, C., Wolfe, P.J. and Boardman, M.R., 1995. Delineation of shallow stratigraphy using ground penetrating radar: J. of App. Geophysics, 33, 167-175.

Eisemberg, D. and Kauzmann, W., 1969. The structure and properties of water: Oxford University Press, New York.

Engheta, N., Papas, C.H. and Elachi, C., 1982. Radiation patterns of interfacial dipole antennas: Radio Sci., 17, 1557-1566.

Fieseler, R.G., Jasek, J. and Jasek, M., 1978. An introduction to the caves of Texas: Speleo Press, Austin, Texas.

Fruhwirth, R. and Mueller, R., 1994. Application of ground penetrating radar to geotechnical problems: In 56th meeting and technical exhibition, European Association of Exploration Geophysicists, technical programme and abstracts of papers, 56, 1012-1013.

Fuchs, K. and Müller, G., 1971. Computation of synthetic seismograms with the Reflectivity Method and comparison with observations: Geophys. J. R. astr. Soc., 23, 417-433.

Galloway, W.E., Ewing, T.E., Garrett, C.M., Tyler, N. and Bebout, D.G., 1983. Atlas of major Texas oil reservoirs: Bureau of Economic Geology, The University of Texas at Austin.

Gilbert, F. and Backus, G.E, 1966. Propagator matrices in elastic and vibration problems: Geophysics, 21, No. 2, 326-332.

Gloaguen, E., Chouteau, M., Marcotte, D. and Chapuis R., 2001. Estimation of hydraulic conductivity of an unconfined aquifer using cokriging of GPR and hydrostratigraphic data: J. of App. Geophysics, 47, 135-152.

Grandjean, G. and Gourry, J.C., 1996. GPR data processing for 3D fracture mapping in a marble quarry (Thassos, Greece): J. of App. Geophysics, 36, 19-30.

Grausmueck, M. and Horstmeyer, H., 1994. Seismic processing on single- and multi-offset ground penetrating radar: 56th meeting and technical exhibition, European Association of Exploration Geophysicists, technical programme and abstracts of papers, 56, 1009-1010.

Hansen, T.B. and Johansen, P.M., 2000. Inversion scheme for Ground Penetrating radar that takes into account the planar air-soil interface: IEEE transactions on Geosciences and Remote Sensing, 38, No. 1, 496-506.

Haskell, N.A., 1953. The dispersion of surface waves on multilayered media: Bull. Seis. Soc. Am., 43, No. 1, 17-43.

Hoekstra, P. and Delaney, A., 1974. Dielectric properties of soils at UHF and microwave frequencies: J. Geoph. Res., 79, No. 11, 1699-1708.

Issacson, E. and Keller, H.B., 1966. Analysis of numerical Methods: John Wiley & Sons, New York.

Jackson J.D., 1975. Classical electrodynamics: John Wiley & Sons, New York.

Jin, S., Mosher, C.C. and Wu, R., 2002. Offset-domain pseudoscreen prestack depth migration: Geophysics, 67, No. 6, 1895-1902.

Karlsson, A. and Kristensson, G., 1992. Constitutive relations, dissipation and reciprocity for the Maxwell equations in the time domain: J. Electromag. Waves and Applications, 6, 537-551.

Kennett, B.L.N., 1974. Reflections, rays and reverberations: Bull. Seism. Soc. Am., 64, 1685-1696.

Kennett, B.L.N. and Kerry, N. J., 1979. Seismic waves in stratified half space: Geophys. J. R. astr. Soc., 57, No. 3, 557-583.

Kennett, B.L.N., 1983. Seismic wave propagation in stratified media. Cambridge university press.

Lampe, B., Holliger, K. and Green, A. G., 2003. A finite-difference time-domain simulation tool for ground-penetrating radar antennas: Geophysics, 68, No. 3, 971-987.

Lehmann, F., Boerner, D.E., Holliger, K. and Green, A.G., 2000. Multicomponent georadar data: Some important applications for data acquisition and processing: Geophysics, 65, No. 5, 1542-1552.

Luebbers, R.J. and Hunsberger F., 1992. FDTD for Nth-order dispersive media: IEEE transactions on Antennas and Propagation, 40, No. 1, 1297-1301.

McMechan, G.A., Loucks, R.G., Mescher, P. and Zeng, X., 2002. Characterization of a coalesced, collapsed paleocave reservoir analog using GPR and well-core data: Geophysics, 67, 1148-1158.

Meincke, P., 2001. Linear GPR inversion for lossy soil and planar air-soil interface: IEEE transactions on Geosciences and Remote Sensing, 39, No. 12, 2713-2721.

Olhoeft, R.G. and Capron, E.D., 1994. Petrophysical causes of electromagnetic dispersion: Proc. of the 5th Internt. Conf. on ground-penetrating radar, 145-152.

Ottolini, R. and Claerbout, J.F., 1984. The migration of common mid-point slant-stacks: Geophysics, 49, No. 3, 237-249.

Pervago, E., Mousatov, A. and Shevnin V., 2003. Electric field modeling in arbitrary anisotropic layered media using the set of Fast Hankel Transformations of integer orders: 73rd Annual Internat. Mtg., Soc. Expl. Geophysicist, Expanded Abstracts, 564-567.

Pipan, M., Forte, E., Dal Moro, G., Sugan, M. and Finetti, I., 2003. Multifold ground-penetrating radar and resistivity to study the stratigraphy of shallow unconsolidated sediments: The Leading Edge, September, 876-881.

Purnell, G., Sukup, D. and Higginbotham, J., 2002. Wave-equation migration of common-receiver gathers for AVO analysis: The Leading Edge, December, 1242-1246.

Richtmyer, R.D. and Morton, K. W., 1967. Difference methods for initial-value problems: Interscience Publishers, New York.

Roberts, R.L. and Daniels, J.J., 1997. Modeling near-field GPR in three dimensions using the FDTD method: Geophysics, 62, 1114-1126.

Scott, J.H., Carroll, R.D. and Cunningham D.R., 1967. Dielectric constant and electrical measurements of moist rocks: A new laboratory methods: J. Geoph. Res., 72, No. 20, 5101-5115.

Sen, M.K. and Roy, I. G., 2002. Two problems in pre-stack inversion: Optimal Regularization and Computation of Differential Seismograms: 72nd Annual Internat. Mtg., Soc. Expl. Geophysicist, Expanded Abstracts, 894-897.

Sen, M.K. and Stoffa, P.L., 1991. Nonlinear one-dimensional seismic waveform inversion using simulated annealing: Geophysics, 56, No. 10, 1624-1638.

Sena, A.R., Stoffa, P.L. and Sen, M.K., 2003. Split Step Fourier Migration of Ground Penetrating Radar Data: 73rd Annual Internat. Mtg., Soc. Expl. Geophysicist, Expanded Abstracts, 1023-1026.

Sherman, M. M., 1988. A model for the frequency dependence of dielectric permittivity of reservoir rocks: The Log Analyst, 29, No. 5, 358-369.

Smith, G.S., 1984. Directive properties of antennas for transmission into a material half-space: IEEE Transactions on Antennas and Propagation, 32, No. 3, 232-246.

Stenberg, B.K. and McGill, J.W., 1995. Archeology studies in southern Arizona using ground penetrating radar: J. of App. Geophysics, 33, 209-225.

Stern, W., 1930. On a method and some results of electrodynamic measurement of glacier ice thickness: Z. Gletscherkd. Glazial-geol., 18, 24-42.

Stoffa, P.L., Buhl, P., Diebold, J.B. and Wenzel, F., 1981. Direct mapping of seismic data to the domain of intercept time and ray parameter – A plane wave decomposition: Geophysics, 46, No. 3, 255-267.

Stoffa, P.L., Fokkema, J.T., Freire, R.M. and Kessinger, W.P., 1990. Split-step Fourier migration: Geophysics, 55, 410-421.

Stoffa, P.L. and Sen, M.K., 1991. Nonlinear multiparameter optimization using genetic algorithm: Inversion of plane-wave seismograms: Geophysics, 56, No. 11, 1794-1810.

Taflove, A. and Brodwin, M.E, 1975. Numerical solution of steady-state electromagnetic scattering problems using the time-dependent Maxwell's equations: IEEE transactions on Microwave Theory and Techniques, 23, No. 8, 623-630.

Taflove, A. and Umashankar, K.R., 1989. Review of FD-TD numerical modeling of electromagnetic wave scattering and radar cross section: Proceedings of the IEEE, 77, No. 5, 682-699.

Tanis, M.C., 1998. Prestack split-step Fourier depth migration algorithms and parallel implementations on Cray T3E: Ph.D. Dissertation, University of Texas at Austin, Austin, Texas.

Teixeira, F.L., Chew, W.C., Straka M., Oristaglio, M.L. and Wang, T., 1998. Finite-difference Time-domain simulation of Ground Penetrating Radar on dispersive, inhomogeneous, and conductive soils: IEEE transactions on Geosciences and Remote Sensing, 36, No. 6, 1928-1937.

Telford, W.M., Geldart, L.P., Sheriff, R.E. and Keys, D.A., 1976. Applied Geophysics: Cambridge University Press, Cambridge.

Thomson, W.T., 1950. Transmission of elastic waves through a stratified medium: J. App. Physics, 21, 89-93.

Topp, G.C., Davis, J.L. and Annan, A.P., 1980. Electromagnetic determination of soil water content; measurement in coaxial transmission lines: Water Resources Research, 16, 574-582.

Tsoflias, G.P., Van Gestel J., Stoffa P.L., Blankenship D.D. and Sen M.K., 2004. Vertical fracture detection by exploiting the polarization properties of ground-penetrating radar signals: Geophysics, 69, 803-810.

Ursin, B., 1983. Review of elastic and electromagnetic wave propagation in horizontally layered media: Geophysics, 48, No. 8, 1063-1081.

Valera, C.L., Stoffa, P.L. and Sen, M.K., 1998. Background velocity estimation using non-linear optimization for reflection tomography and migration misfit: Geoph. Prospecting, 46, No. 1, 51-78.

Van der Kruk, J., Wapenaar, C.P. A., Fokkema, J.T. and Van den Berg, P.M., 2003. Three-dimensional imaging of multicomponent ground-penetrating radar data: Geophysics, 68, No. 4, 1241-1254.

Van Gestel, J. and Stoffa P.L., 2001. Application of Alford rotation to ground-penetrating radar data: Geophysics, 66, No. 6, 1781-1792.

Varga, R.S., 1962. Matrix iterative analysis: Prentice-Hall, Englewood Cliffs, New Jersey.

Wait, J.R., 1953. Propagation of radio waves over a stratified ground: Geophysics, 18, No. 2, 416-422.

Wang, T. and Oristaglio, M.L., 2000. GPR imaging using the generalized Radon Transform: Geophysics, 65, No. 5, 1553-1559.

Xiong, Z. and Tripp, A.C., 1997. 3-D electromagnetic modeling for near-surface targets using integral equations: Geophysics, 62, No. 4, 1097-1106.

Xu, T. and McMechan G. A., 1997. GPR attenuation and its numerical simulation in 2.5 dimensions: Geophysics, 62, No. 1, 403-414.

Yee, K. S., 1966. Numerical solution of initial boundary value problem involving Maxwell's equations in isotropic media: IEEE transactions on Antennas and Propagation, 14, No. 3, 302-307.

Yilmaz, Ö., 2001. Seismic data analysis. Vol. 1. Ed: Doherty, S. M., Soc. Expl. Geophys., Tulsa, USA.

Zeng, X., McMechan, G.A., Cai, J. and Chen, H., 1995. Comparison of ray and Fourier methods for modeling of monostatic ground-penetrating radar profiles: Geophysics, 60, No. 6, 1727-1734.

Zeng, X., McMechan G.A. and Xu, T., 2000. Synthesis of amplitude-versus-offset variations in ground-penetrating radar data: Geophysics, 65, No. 1, 113-125.

Zhou, B. and Fullagar, P.K., 2001. Delineation of sulphide ore-zones by borehole radar tomography at Hellyer Mine, Australia: J. App. Geophysics, 47, No. 3-4, 261-269.

Vita

Armando Sena was born in Naples, Italy, on July 31, 1970, to Maria Sena D'anna and Salvatore Sena. Then, his family moved to Venezuela where he completed his high school in Carrizal, Estado Miranda, in 1986. In 1987, he entered the Department of Physics and Mathematics at the Faculty of Sciences of the Central University of Venezuela. He completed all his required classes in 1992, but economic reasons impeded him to pursue his thesis that year. In the summer of 1994, he started his thesis work at the Venezuelan Institute for Scientific Research and successfully defended it in the fall of 1995. He received the degree of Licentiate in Physics in the spring of 1996. In 1997, he obtained a position as instructor and research scientist at the Earth Sciences Institute of the Central University of Venezuela, and in August 2000, he enrolled in the PhD program in the Department of Geological Sciences of The University of Texas at Austin. He participated in a marine seismic survey at the Hess Deep Rift area in summer of 2003. Upon graduation, he will continue with his position as research scientist and professor at the Earth Sciences Institute of the Central University of Venezuela.

Permanent address: 7117 Wood Hollow Dr., Apt. 818, Austin, Texas 78731.

This dissertation was typed by the author.